Universität Hamburg
DER FORSCHUNG | DER LEHRE | DER BILDUNG

A Matter-Wave Microscope for Lithium Atoms in a Tunable Optical Lattice

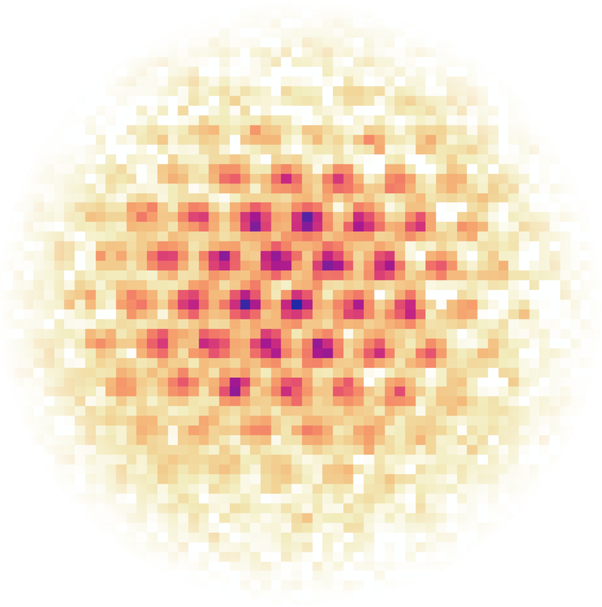

Dissertation zur Erlangung des Doktorgrades

an der Fakultät für Mathematik, Informatik und Naturwissenschaften
Fachbereich Physik der Universität Hamburg

vorgelegt von
Mathis Samuel Fischer
aus Hamburg

Hamburg
2023

Gutachter

Gutachter der Dissertation:	Dr. Christof Weitenberg Prof. Dr. Henning Moritz
Zusammensetzung der Prüfungskomission:	Dr. Christof Weitenberg Prof. Dr. Henning Moritz Prof. Dr. Klaus Sengstock Prof. Dr. Ludwig Mathey Prof. Dr. Markus Drescher
Vorsitzender der Prüfungskommission:	Prof. Dr. Ludwig Mathey
Datum der Disputation:	28.09.2023
Vorsitzender Fach-Promotionsausschuss PHYSIK:	Prof. Dr. Günter H. W. Sigl
Leiter des Fachbereichs PHYSIK:	Prof. Dr. Wolfgang J. Parak
Dekan der Fakultät MIN:	Prof. Dr.-Ing. Norbert Ritter

Eidesstattliche Versicherung

Hiermit versichere ich an Eides statt, die vorliegende Dissertationsschrift selbst verfasst und keine anderen als die angegebenen Hilfsmittel und Quellen benutzt zu haben.

Hamburg, den 03.08.2023
Ort, Datum

Mathis Fischer
Mathis Fischer

Abstract

Ultracold gases in optical lattices are a pristine experimental platform for quantum simulation of complex many-body systems as they come with a high degree of control and a wide range of accessible observables. The advent of quantum gas microscopes has revolutionized the access to quantum many-body systems by detecting and addressing single particles on single lattice sites. However, they are limited to 2-dimensional (2D) systems and suffer from parity projection due to light assisted collisions. A complementary approach is the so-called matter-wave microscopy or quantum gas magnification, where the atomic density distribution is magnified via matter-wave optics before taking absorption images with sub-lattice site resolution.

In this thesis, we report on the construction of a matter-wave microscope for ultracold ^{7}Li-atoms in optical lattices. Within the course of this thesis, we adapted the experimental apparatus that was formerly used for experiments with the fermionic isotope ^{6}Li, to creating Bose-Einstein condensates of ca. 1×10^5 ^{7}Li-atoms within a cycle time of ca. $14\,$s. To this end, we implemented a multi-frequency 2D-MOT scheme and set up an optically plugged magnetic quadrupole trap as well as a novel dipole trap setup, that can simultaneously be used to create optical lattices with dynamically tunable, yet passively stable geometry of the lattice structure. The interference of three laser beams is suppressed by detuning their frequencies and then pairwisely reestablished by imprinting sidebands onto each beam. This setup allows us to use the same beams as a dipole trap that we also employ as a matter-wave lens for the magnification of the density distribution in the matter-wave microscopy. Via a quarter period evolution in the harmonic trap, the initial positions of the atoms are mapped onto their momenta. A subsequent time of free expansion results in a Fourier transform back to the initial density distribution but with a magnification M that is typically on the order of $M \approx 24$ for our parameter settings. We use this technique to study the matter-wave Talbot effect in coherent systems, which in the future will give us access to the g_1 correlation function.

Zusammenfassung

Ultrakalte Quantengase in optischen Gittern bieten vielseitig einsetzbare Möglichkeiten zur Quantensimulation komplexer Vielteilchensysteme. Sie bestechen dabei durch einen hohen Grad an Kontrolle über das Modellsystem und den Zugang zu einer großen Anzahl von Observablen. Durch die Einführung von Quantengasmikroskopen mit der Möglichkeit, einzelne Teilchen an einzelnen Gitterplätzen zu detektieren und gezielt zu manipulieren, wurde der Zugang zu quantenmechanischen Vielteilchensystemen revolutioniert. Allerdings beschränkt sich dieser Zugang auf zweidimensionale Systeme und Licht-assoziierte Stöße führen dazu, dass nur die Parität der Besetzung auf einem Gitterplatz gemessen werden kann. Ein hierzu komplementärer Ansatz besteht in der sogenannten Materiewellen-Mikroskopie oder auch Quantengasvergrößerung. Hierbei wird die atomare Dichteverteilung mit Hilfe von Materiewellen-Optik vergrößert, bevor sie in einer Absorptionsabbildung mit Sub-Gitterplatzauflösung abgebildet wird.

In dieser Dissertation wurde ein Experiment zur Materiewellen-Mikroskopie ultrakalter ^{7}Li-Atome in optischen Gittern aufgebaut. Die experimentelle Apparatur, die vormals zum Kühlen des fermionischen Isotops ^{6}Li benutzt wurde, wurde im Rahmen dieser Arbeit angepasst, sodass sie nun wiederholt Bose-Einstein-Kondensate bestehend aus 1×10^5 ^{7}Li-Atomen innerhalb von $14\,$s erzeugen kann. Hierfür wurde eine multifrequenz-basierte 2D-MOT entwickelt und eine magnetische Quadrupolfalle in Betrieb genommen. Das Einstrahlen eines repulsiven Laserstrahls verhindert hierbei Majorana-Verluste im Fallenzentrum. Darüberhinaus wurde eine neuartige Dipolfalle errichtet, die auch als optisches Gitter verwendet werden kann. Hierfür werden zunächst drei Laserstrahlen in ihrer Frequenz zueinander verstimmt, sodass sie nicht miteinander interferieren. Anschließend sorgt das Aufmodulieren von Frequenz-Seitenbändern dafür, dass die Interferenz paarweise wiederhergestellt wird. Hierdurch kann die Geometrie der entstehenden Gitterstruktur dynamisch verändert werden, wobei die Geometrie dennoch passiv stabil bleibt. Dieses Lasersystem nutzen wir unter anderem als optische Dipolfalle für die Materiewellen-Mikroskopie. Wir halten die Atome für eine viertel Periode in der durch die Dipolfalle realisierten harmonischen Falle, was dazu führt, dass der anfängliche Ort der Atome durch eine Fourier-Transformation in einen Impuls umgewandelt wird. Eine anschließende freie Expansion ermöglicht eine Rücktransformation zur ursprünglichen Dichteverteilung, wobei diese um einen Faktor M vergrößert wurde. Für typische experimentelle Parameter in unserem System ist diese Vergrößerung $M \approx 24$. Mit dieser Technik studieren wir den sogenannten Materiewellen-Talbot-Effekt. Dieser tritt in kohärenten Systemen auf und wird es uns in Zukunft ermöglichen, Rückschlüsse auf die g_1-Korrelationsfunktion zu ziehen.

Contents

1 Introduction **1**

1.1 Thesis Outline 2

2 Properties of ^{7}Li **3**

2.1 Fundamental Physical Properties 3

2.2 Optical Properties 5

2.3 Energy Levels 6

2.4 Energy Levels and Transitions at Non-zero Magnetic Fields 8

2.5 Collisional Properties 11

2.5.1 Small and Attractive Triplet Scattering Length 11

2.5.2 Large Three-Body Loss Coefficient 13

2.5.3 Feshbach Resonances 13

2.6 Magic Wavelengths 14

3 The ^{7}Li BEC Machine **15**

3.1 The Path to Degeneracy 15

3.2 The Experimental Apparatus 17

3.2.1 The Vacuum Chamber 17

3.2.2 Magnetic Field Coils 20

3.2.3 Radio Frequency Antennas 24

3.2.4 Experimental Control and Sequence Infrastructure 26

3.3 Laser Cooling and Trapping 27

3.3.1 Near-Resonant Laser Systems for Cooling and Imaging 28

3.3.2 2D/3D-MOT 32

3.3.3 Compressed MOT 38

3.3.4 Gray Molasses 39

3.4 Evaporation in the Magnetic Trap 39

3.4.1 Optical Dark State Pumping 41

3.4.2 Loading and Adiabatic Compression of the Magnetic Trap 43
3.4.3 Majorana Losses and Optical Plug 44
3.4.4 Radio Frequency Evaporation 48
3.5 Evaporation in the Crossed Optical Dipole Trap 50
3.5.1 Laser System for the Optical Dipole Trap 50
3.5.2 Loading the Optical Dipole Trap and Adiabatic State Transfer 53
3.5.3 Evaporation near the Feshbach Resonance 54

4 A Multi-Frequency Optical Lattice for Dynamic Control of the Lattice Geometry 57

4.1 Tuning of the Lattice Geometry 57
4.2 Implementation 59
4.3 Calibration of the Geometry Phase 61
4.4 Outlook 65

5 Matter-Wave Microscopy of ^{7}Li 67

5.1 Theoretical Description of the Matter-Wave Lens 68
5.2 Deviations from the Focusing Condition 70
5.3 Implementation 72
5.4 The Matter-Wave Talbot Effect 74
5.5 Conclusion and Outlook 78

6 Conclusion and Outlook 79

A Thermodynamic Considerations in the Magnetic Quadrupole Trap 81

A.1 General Considerations on the Trapping Potential 81
A.2 Diabatic Loading of the Magnetic Trap 81
A.3 Adiabatic Compression/Decompression 83
A.4 Measurement of the Phase-Space Density 84

B Relative Intensity Noise of the Optical Dipole Trap/Lattice Laser 86

Bibliography 89

Glossary 101

List of Figures 103

List of Tables 107

Acknowledgements 109

CHAPTER 1

Introduction

With increasing complexity, the computing of a quantum mechanical system with conventional digital computers becomes exponentially hard, since the dimensionality of the system grows exponentially with the number of constituents. As a solution to this problem for many-body systems, Richard Feynman introduced the concepts of quantum simulation and quantum computation [1]. The basic idea of quantum simulation is to simulate a complex quantum system with restricted access to critical observables with a more accessible model system. This system shall have more control than the original system and the observables of interest shall be easier to access. This simulation can then be used in two ways. One can replicate a known complex system with as little and simple elements as necessary to get insight as to which element is of fundamental importance to the original system. On the other hand, these model systems can be used to engineer new and exotic systems with appealing properties, that could later be transferred to the realization and application in real tools or materials.

Shortly after the first realizations of a Bose-Einstein condensate (BEC) [2–4] it became clear that ultracold atoms are a versatile experimental platform for quantum simulation [5]. By combining quantum gases with optical lattices [6, 7] one can not only simulate condensed matter physics but also study exotic systems without a solid-state counterpart [8]. By interfering two or more laser beams, one can create a periodic potential landscape for neutral atoms that mimics the spatially periodic landscapes of solid crystals. Here the neutral atoms in the optical lattice can play the role of electrons in real materials. Thus, optical lattices are an ideal platform to realize Bose- [9] and Fermi-Hubbard [10] models, where the tunneling rate and the particle interaction strength can be tuned by the experimentalist via tuning the laser intensity or employing Feshbach resonances [11]. Well known examples for this are the direct observation of the quantum phase transitions from a superfluid to a Mott insulator for bosons [12] as well as the metal to band insulator to Mott insulator transition for fermions [13, 14].

The development of quantum gas microscopes [15, 16] added the measurement of single lattice site populations with single atom sensitivity as well as single-site addressing to the toolbox of ultracold atoms experiments, which lead to the observation of a vast number of phenomena [17]. In this work, we have set up a new ^{7}Li BEC experiment and implemented a complementary approach on single lattice-site resolved imaging based on matter-wave optics [18]. Using the evolution in a harmonic trap followed by a free expansion, we perform two Fourier transformations that reproduce the initial atomic density distribution with a magnification. We can then use standard absorption imaging techniques to get single-shot images of the real space density distribution of atoms in a 2D lattice of 1-dimensional (1D) tubes with up to ~ 1000 atoms per lattice site. With this matter-wave microscope we directly observe the matter-wave Talbot effect in coherent systems, which in the future will give us access to the g_1 correlation function. We also implemented a novel type of optical lattice [19], that uses multiple frequency components to enable a tunable yet passively stable lattice geometry.

1.1 Thesis Outline

This thesis is organized as follows. In chapter 2, we summarize the experimentally relevant properties of ^{7}Li that we need to consider on the pathway to quantum degeneracy. In particular, we discuss the collisional properties of ^{7}Li, that require a precisely engineered experimental sequence to balance the low elastic collision rate and the high three-body loss rate.

In chapter 3 we give a detailed description of the experimental apparatus and the experimental cycle to reach Bose-Einstein condensation. We report on the implementation of a multi-frequency 2D-MOT with which we enhance the particle number after sub-Doppler cooling by a factor of $\sim 5 - 10$. We set up an optically plugged magnetic quadrupole trap to balance the disadvantageous collisional properties during radio frequency (RF) evaporation. Before reaching quantum degeneracy, we load the atoms into an optical dipole trap and, after an internal state transfer, evaporatively cool them to Bose-Einstein condensation in the vicinity of a Feshbach resonance.

Chapter 4 presents our approach on the multi-frequency optical lattice [19], for which we use the same laser system that produces the optical dipole trap in our BEC sequence.

In chapter 5, we introduce the matter-wave microscope based on [18], where we use an optical dipole trap as a matter-wave lens for spin-independent magnification. The first part of this chapter considers the theoretical description of the focusing condition and slight deviations from it. We then present the experimental implementation of the technique and end with real-space measurements of the matter-wave Talbot effect.

Finally, chapter 6 summarizes this thesis and gives an outlook towards possible future research directions.

CHAPTER 2

Properties of ^{7}Li

When we initially started working on cooling ^{7}Li, we soon encountered problems, because our knowledge and experiences from working with ^{6}Li and ^{87}Rb could not all be applied to ^{7}Li. These issues arose from fundamental differences in some of the physical properties that are relevant for the successful preparation of ultracold gases. The most important of these are the collisional properties of ^{7}Li. While there are great resources on the relevant physical properties for Rubidium, Cesium, Sodium, Potassium and the fermionic isotope ^{6}Li by and Daniel Steck, Tobias Tiecke and Michael Gehm [20–25], there is - to the best of our knowledge - no comparable manuscript discussing properties of ^{7}Li. A review article by Randall G. Hulet, Jason H. V. Nguyen, and Ruwan Senaratne [26] discusses methods for the preparation of cold gases of both Lithium isotopes. Here we want to summarize these results together with other resources to provide the relevant data solely for ^{7}Li in a similar format as from Michael Gehm for ^{6}Li. We focus on the important properties that need to be considered for successful Bose-Einstein condensation of ^{7}Li.

2.1 | Fundamental Physical Properties

Lithium is the lightest alkali-metal denoted by the chemical symbol Li with an atomic number of Z=3. In this thesis we focus on the bosonic isotope ^{7}Li. The fundamental physical properties of atomic ^{7}Li are shown in table 2.1. It is solid at room temperature and standard pressure. Due to the single valence electron, it is very chemically reactive. It especially reacts quickly with water and when exposed to air, it forms a crust of oxides and hydroxides on the surface, that have a much higher melting point than the pure Lithium metal. It is therefore commonly stored in paraffin oil or cyclohexane. Lithium also chemically reacts with Copper and Nitrogen, which one has to be aware of when constructing or flooding vacuum chambers. Compared to the other alkali-metals it has a relatively low vapor pressure. One thus has to go to higher temperatures to produce atomic beam sources or vapor cells that are sufficient for cold atom experiments. For a given temperature T in K one can determine the vapor pressure P_V in mbar of solid and liquid Lithium with the formula [27]:

$$\text{(solid)}\;\; \log(P_\mathrm{V}) = 8.673 - \frac{8310}{T} \qquad 298\,\mathrm{K} < T < T_\mathrm{M} \tag{2.1}$$

$$\text{(liquid)}\;\; \log(P_\mathrm{V}) = 8.061 - \frac{8023}{T} \qquad T_\mathrm{M} < T < 600\,\mathrm{K}, \tag{2.2}$$

where T_M is the melting point of Lithium. It is listed in table 2.2 together with other physical and thermochemical properties. A comparison of the vapor pressure of Lithium with other alkali-metals is shown in figure 2.1.

Table 2.1: Atomic properties of ^{7}Li.

Property	Symbol	Value	Ref.
Atomic number	Z	3	[28]
Nucleons	$Z+N$	7	[28]
Natural abundance	η	$92.41\,\%$	[28]
Nuclear lifetime	τ_n	stable	[28]
Atomic mass	m	$7.016\,004\,55$ u $11.650\,349\,5 \times 10^{-27}$ kg	[28]
Total electronic spin	S	$1/2$	[28]
Total nuclear spin	I	$3/2$	[28]
Magnetic moment	μ	$3.256\,427\,\mu_\mathrm{N}$ $16.447\,508 \times 10^{-27}$ J/T	[28]

Table 2.2: Physical and thermochemical properties of bulk ^{7}Li.

Property	Symbol	Value	Ref.
Density at 298 K	ρ	535 kg/m^3	[29]
Melting point	T_M	453.69 K	[29]
Enthalpy of fusion	Q_F	3.0 kJ/mol	[29]
Boiling point	T_B	1615 K	[30]
Enthalpy of vaporization	Q_V	134.7 kJ/mol	[30]

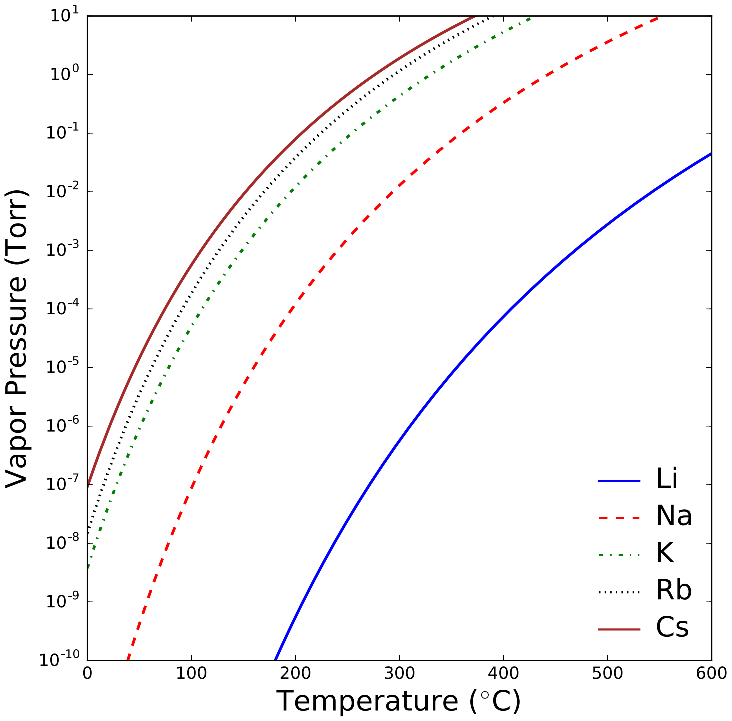

Figure 2.1: Vapor pressure of different alkali elements. Figure taken from [26].

2.2 | Optical Properties

As for all alkali elements there are two prominent spectral lines of the ground state of ^{7}Li called the D1 ($2^2S_{1/2} \longrightarrow 2^2P_{1/2}$) and D2 ($2^2S_{1/2} \longrightarrow 2^2P_{3/2}$) line (for historical reasons). Some properties of these spectral lines are listed in table 2.3 and table 2.4, respectively. The wavelength λ and the wavenumber k are related to the frequency of the transition via

$$\nu = \frac{c}{\lambda}, \qquad k = \frac{2\pi}{\lambda}, \tag{2.3}$$

with the speed of light c. The natural linewidth of the excited state Γ can be derived from the respective lifetime τ via:

$$\Gamma = \frac{1}{\tau}. \tag{2.4}$$

This linewidth can be associated with the so-called Doppler temperature T_D that is the fundamental limit to Doppler cooling:

$$k_\mathrm{B} T_\mathrm{D} = \frac{\hbar\Gamma}{2}, \tag{2.5}$$

with the Boltzmann constant k_B and the reduced Planck constant $\hbar$. Sub-Doppler cooling techniques are fundamentally limited to the so-called recoil temperature T_R that is associated with the residual momentum transfer of a single scattered photon. This momentum is simply given by

$$m v_\mathrm{R} = \hbar k \tag{2.6}$$

and thus the recoil temperature can be expressed as

$$k_\mathrm{B} T_\mathrm{R} = \frac{1}{2} m v_\mathrm{R}^2 = \frac{(\hbar k)^2}{2m}, \tag{2.7}$$

where m is the atomic mass of ^{7}Li. We finally define the saturation intensity I_sat as the intensity where the optical Rabi frequency equals the spontaneous decay rate and the transition is thus saturated. The exact value depends on the properties of the transition. For a cycling transition it is given as

$$I_\mathrm{sat} = \frac{\pi h c}{3\lambda^3 \tau}. \tag{2.8}$$

Table 2.3: Optical properties of the ^{7}Li D1-line.

Property	Symbol	Value	Ref.
Frequency	ν	$446\,800\,132.006(25)$ MHz	[31, 32]
Wavelength (vacuum)	λ	$670.976\,654\,939$ nm	
Wavenumber (vacuum)	$k/2\pi$	$14\,903.648\,\mathrm{cm}^{-1}$	
Lifetime	τ	$27.102(7)$ ns	[33]
Natural linewidth	$\Gamma/2\pi$	5.8724 MHz	
Doppler temperature	T_D	140.915 μK	
Atomic recoil velocity	v_R	$8.476\,366$ cm/s	
Recoil temperature	T_R	$3.031\,413$ μK	

Table 2.4: Optical properties of the ^{7}Li D2-line.

Property	Symbol	Value	Ref.
Frequency	ν	$446\,810\,184.005(33)$ MHz	[31, 32]
Wavelength (vacuum)	λ	$670.961\,559\,812$ nm	
Wavenumber (vacuum)	$k/2\pi$	$14\,903.983\,\mathrm{cm}^{-1}$	
Lifetime	τ	$27.102(7)$ ns	[33]
Natural linewidth	$\Gamma/2\pi$	5.8724 MHz	
Recoil temperature	T_R	$3.031\,549$ µK	
Atomic recoil velocity	v_R	$8.476\,557$ cm/s	
Doppler temperature	T_D	140.915 µK	
Saturation intensity	I_sat	$2.54\,\mathrm{mW/cm}^2$	

2.3 | Energy Levels

In the semi-classical approximation, the energy levels of an atom are only determined by the principal quantum number n and the angular momentum L. When taking into account the spin-orbit interaction that couples the orbital angular momentum $\boldsymbol{L}$ of the valence electron and its spin $\boldsymbol{S}$, the system has to be described by the total electronic angular momentum

$$\boldsymbol{J} = \boldsymbol{L} + \boldsymbol{S}. \tag{2.9}$$

The corresponding quantum number J can take values in the range of $|L - S| \leq J \leq L + S$. As a consequence the degeneracy of the two $2P$-states is resolved. The fine structure energy splitting for ^{7}Li is $\Delta E_\mathrm{FS} = 10\,052.37(11)$ GHz [34]. When also taking into account the coupling of the nuclear Spin $\boldsymbol{I}$ to $\boldsymbol{J}$, we get the hyperfine structure. The total atomic angular momentum $\boldsymbol{F}$ is then given by

$$\boldsymbol{F} = \boldsymbol{J} + \boldsymbol{I} \tag{2.10}$$

and consequently the quantum number F is in the range of $|J - I| \leq F \leq J + I$. This again lifts the degeneracy of the F-subspaces and results in a hyperfine energy shift given as [25]

$$\Delta E_\mathrm{HFS} = \frac{1}{2}AC + \frac{3}{8}B\frac{C(C+1)}{I(2I-1)J(2J-1)}, \tag{2.11}$$

where $C = F(F+1) - J(J+1) - I(I+1)$ and A and B are the magnetic dipole hyperfine constant and the electric quadrupole hyperfine constant respectively. Measured values for these constant for the states of interest are listed in table 2.5. For the ground-state the energy-splitting between $F = 1$ and $F = 2$ is $\Delta E_\mathrm{HFS} = 803.504\,086\,6$ GHz [31]. The resulting level scheme including the hyperfine structure is displayed in figure 2.2. We note that the hyperfine splitting of the $2^2P_{3/2}$-state is on the order of the natural linewidth. Thus, sub-Doppler cooling techniques that are standard for other alkalis are not suitable for Lithium. In the past years, Gray Molasses cooling on the D1 transtion [35] has become an established technique to reach sub-Doppler temperatures.

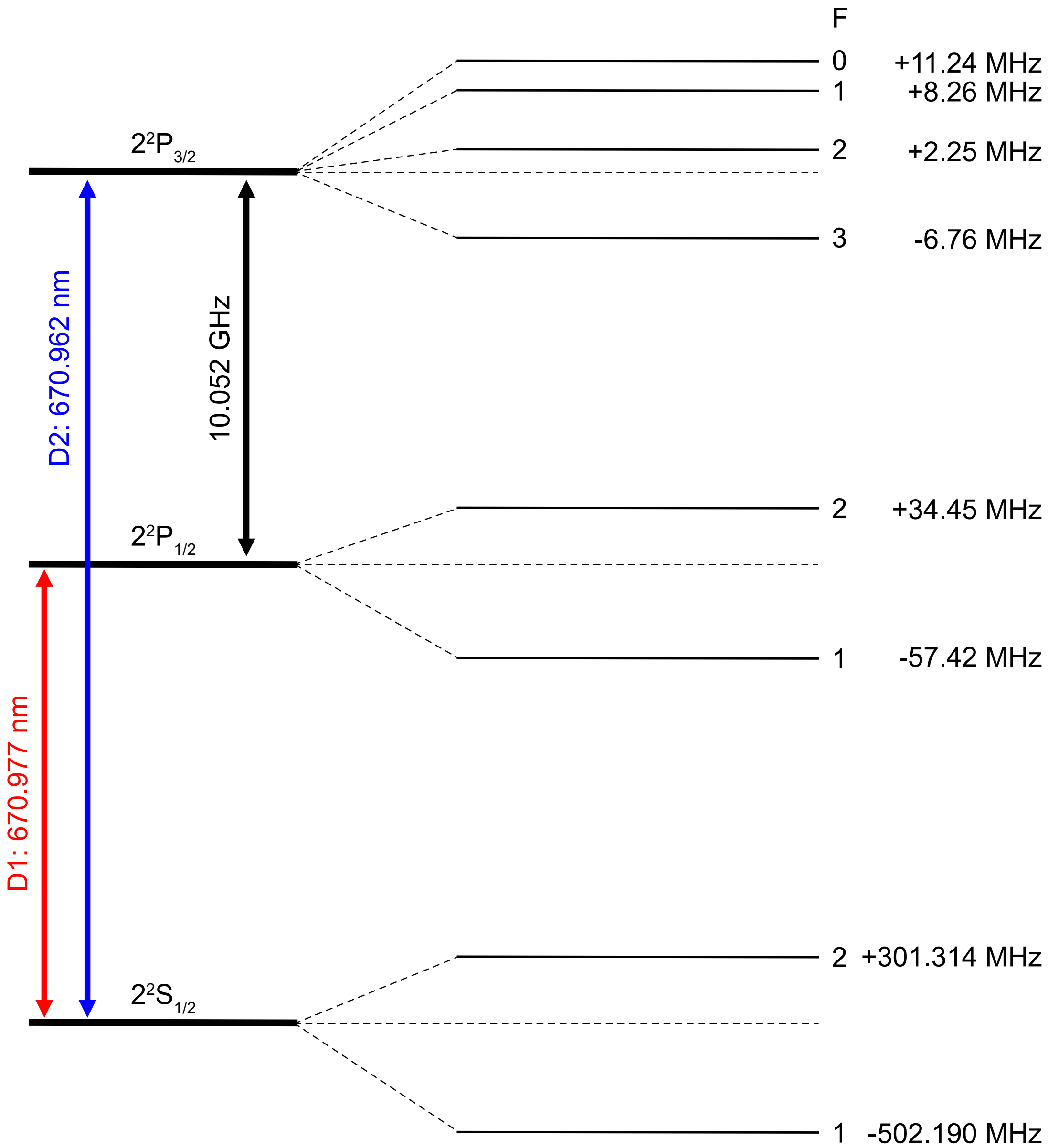
F
0 +11.24 MHz
1 +8.26 MHz
2 +2.25 MHz
3 -6.76 MHz
$2^2P_{3/2}$
D2: 670.962 nm
10.052 GHz
$2^2P_{1/2}$
2 +34.45 MHz
1 -57.42 MHz
D1: 670.977 nm
$2^2S_{1/2}$
2 +301.314 MHz
1 -502.190 MHz

Figure 2.2: Energy level scheme of ^{7}Li - Spectroscopic data for the plot were taken from [31, 32, 36, 34].

Table 2.5: Hyperfine constants for the $2S$ and $2P$ levels of ^{7}Li.

Property	Symbol	Value	Ref.
$2^2S_{1/2}$ Magnetic dipole constant	$A_{2^2S_{1/2}}$	$401.752\,043\,3(5)$ MHz	[37]
$2^2P_{1/2}$ Magnetic dipole constant	$A_{2^2P_{1/2}}$	$46.17(35)$ MHz	[37]
$2^2P_{3/2}$ Magnetic dipole constant	$A_{2^2P_{3/2}}$	$-3.055(14)$ MHz	[37]
$2^2P_{3/2}$ Electric quadrupole constant	$B_{2^2P_{3/2}}$	$-0.221(29)$ MHz	[37]

2.4 Energy Levels and Transitions at Non-zero Magnetic Fields

In the presence of small magnetic fields B, the energy of the states is shifted by the Zeeman energy shift:

$$\Delta E_{\mathrm{Zeeman}}(B) = m_F g_F \mu_{\mathrm{B}} B, \tag{2.12}$$

with the magnetic quantum number m_F, the hyperfine Landé-factor g_F and the Bohr magneton μ_{B}. For daily back-of-the-envelope calculations in the lab, it can be helpful to memorize that $\mu_{\mathrm{B}} \approx 1.4\,\mathrm{MHz/G}$. The hyperfine Landé-factor g_F is given by [22]

$$g_F = g_J \frac{F(F+1) - I(I+1) + J(J+1)}{2F(F+1)} + g_I \frac{F(F+1) + I(I+1) - J(J+1)}{2F(F+1)}. \tag{2.13}$$

For higher magnetic fields, the coupling of $\boldsymbol{I}$ and $\boldsymbol{J}$ to $\boldsymbol{F}$ is broken and F is no longer a good quantum number. In this so-called Paschen-Back regime, the energy shift ΔE_{PB} is given by

$$\Delta E_{\mathrm{PB}}(B) = (m_I g_I + m_J g_J)\mu_{\mathrm{B}} B. \tag{2.14}$$

The relevant electronic and nuclear gyromagnetic factors are given in table 2.6. For completeness we also include the polarizabilities in the presence of DC electric fields that are needed to calculate the DC Stark shift. We don't cover this topic any further here.

Table 2.6: ^{7}Li magnetic and electric field interaction parameters.

Property	Symbol	Value	Ref.
Electronic spin g-factor	g_S	$-2.002\,319\,304\,362\,56(35)$	[38]
Total nuclear g-factor	g_I	$-0.001\,182\,213\,0(3)$	[36]
Total electronic g-factor	$g_J(2^2S_{1/2})$	$2.002\,301\,0(7)$	[37]
	$g_J(2^2P_{1/2})$	$0.666\,8(20)$	[37]
	$g_J(2^2P_{3/2})$	$1.335(10)$	[37]
Total atomic g-factor	$g_F(2^2S_{1/2}),\ F=1$	-0.5021	
	$g_F(2^2S_{1/2}),\ F=2$	0.4997	
	$g_F(2^2P_{1/2}),\ F=1$	-0.1685	
	$g_F(2^2P_{1/2}),\ F=2$	0.1661	
	$g_F(2^2P_{3/2}),\ F=0$	0.6669	
	$g_F(2^2P_{3/2}),\ F=1$	0.6669	
	$g_F(2^2P_{3/2}),\ F=2$	0.6669	
	$g_F(2^2P_{3/2}),\ F=3$	0.6669	
Ground-state scalar polarizability	$\alpha_0\ (2^2S_{1/2})$	$0.0408(8)\,\mathrm{Hz/(V/cm)^2}$	[39]
D1 scalar polarizability	$\alpha_0\ (2^2P_{1/2})$	$0.031\,57(8)\,\mathrm{Hz/(V/cm)^2}$	[39]
D2 scalar polarizability	$\alpha_0\ (2^2P_{3/2})$	$0.031\,52(9)\,\mathrm{Hz/(V/cm)^2}$	[39]
D2 tensor polarizability	$\alpha_2\ (2^2P_{3/2})$	$0.409(11)\,\mathrm{Hz/(V/cm)^2}$	[39]

Figures 2.3, 2.4 and 2.5 show the energy shift of the $2^2S_{1/2}$-, $2^2P_{1/2}$- and $2^2P_{3/2}$-state at a magnetic field of up to $1000\,\mathrm{G}$. The data for these figures were obtained with a *Wolfram Mathematica* script based on appendix C.2 of Michael Gehm's PhD thesis [40]. We numerate the corresponding states in ascending order of their respective energy.

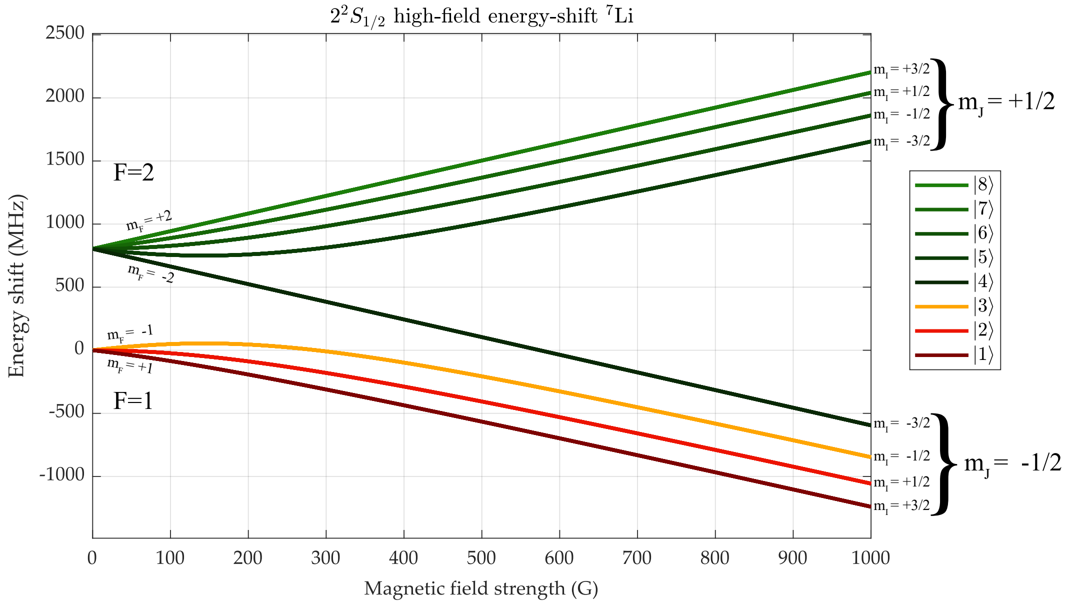

Figure 2.3: Ground-state energy shift at varying magnetic field - The energy zero is set to the lowest energy of the respective state at zero magnetic field. The data for this figure were obtained with a *Wolfram Mathematica* script based on appendix C.2 of Michael Gehm's PhD thesis [40].

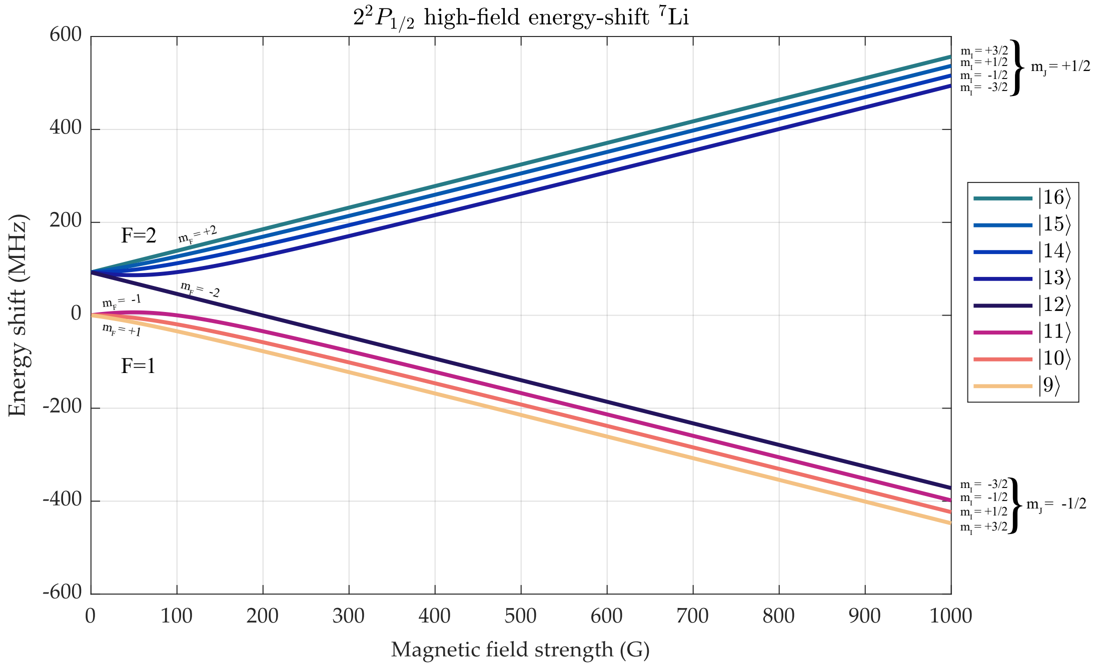

Figure 2.4: Energy shift of the $2^2P_{1/2}$-state at varying magnetic field - The energy zero is set to the lowest energy of the respective state at zero magnetic field. The data for this figure were obtained with a *Wolfram Mathematica* script based on appendix C.2 of Michael Gehm's PhD thesis [40].

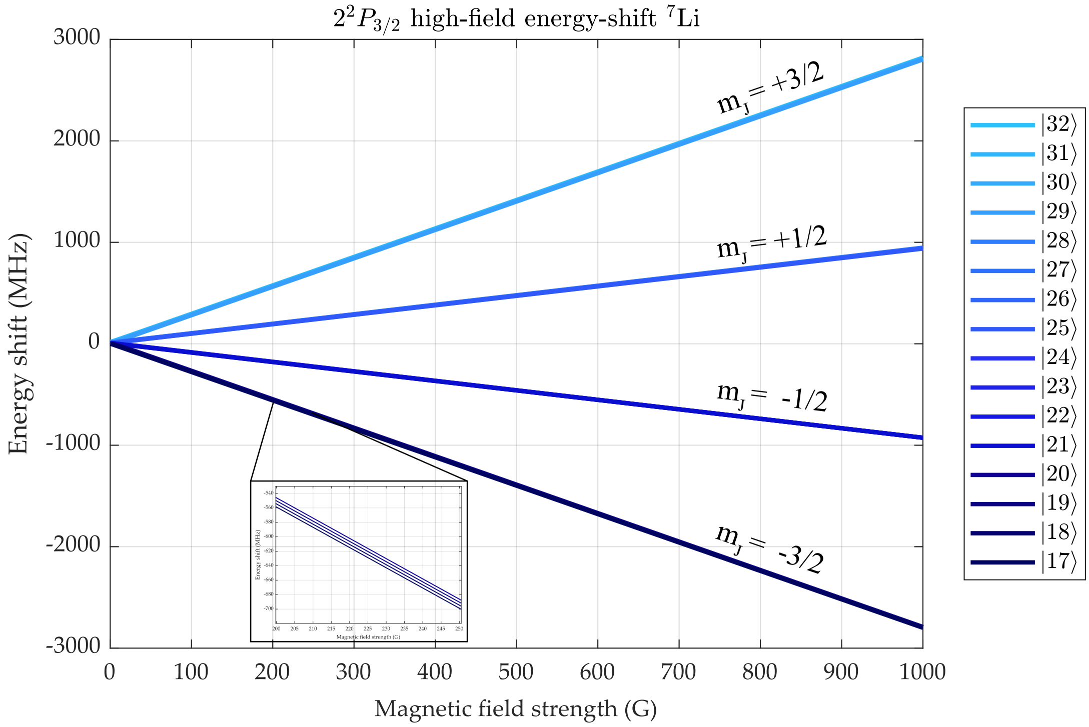

Figure 2.5: Energy shift of the $2^2P_{3/2}$-state at varying magnetic field - The energy zero is set to the lowest energy of the respective state at zero magnetic field. The hyperfine splitting at zero magnetic field is not resolved. The inlet shows that in every of the four large branches there are four almost equidistant states. The data for this figure were obtained with a *Wolfram Mathematica* script based on appendix C.2 of Michael Gehm's PhD thesis [40].

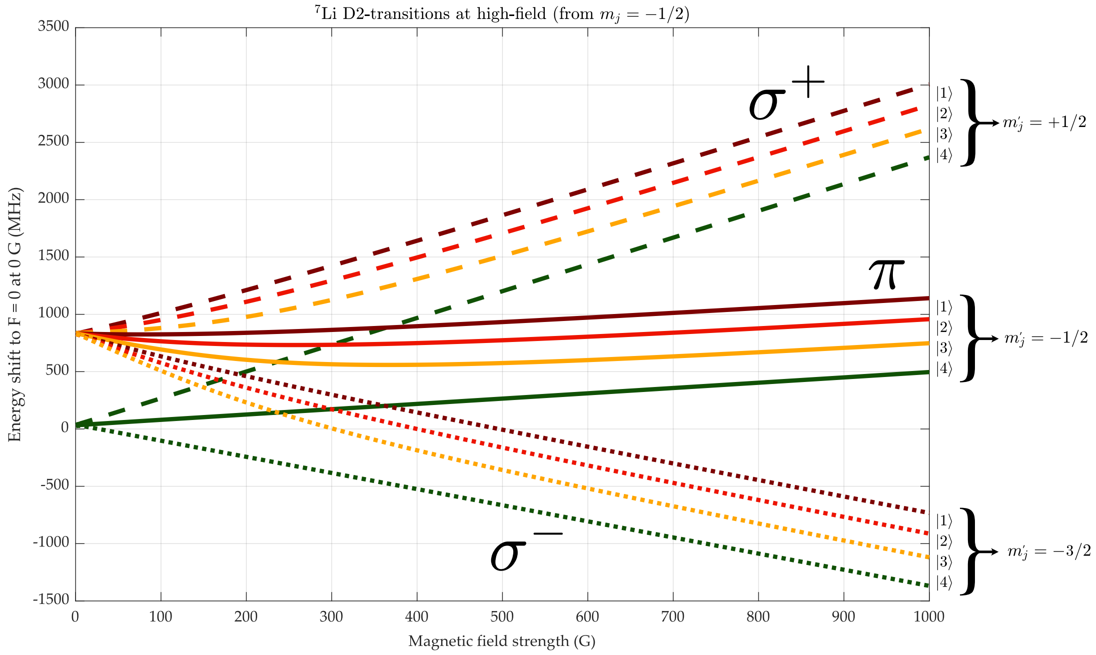

Figure 2.6: D2 transitions at high fields from $m_J = -1/2$ - The data for this figure were obtained with a *Wolfram Mathematica* script based on appendix C.2 of Michael Gehm's PhD thesis [40].

With this data, we can now calculate the energy shift of the optical transitions from the ground-state to the $2^2P_{3/2}$-state on the D2-line. We only take into account transitions that are allowed by selection rules via $\Delta m_J = 0, \pm 1$. For more clarity, we present the data in two separate plots. Figure 2.6 displays the transition frequencies for $\sigma^\pm$- and π-transitions from the lower four energy states $|1\rangle$ - $|4\rangle$. Figure 2.7 shows the transitions for the upper four states $|4\rangle$ - $|8\rangle$.

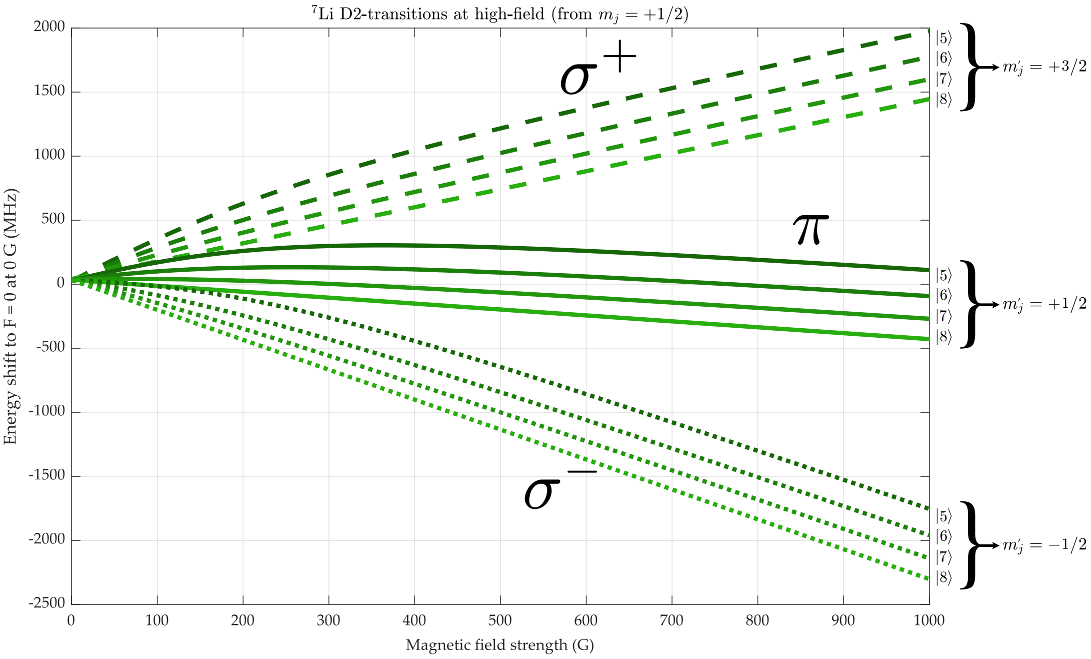

Figure 2.7: D2 transitions at high fields from $m_J = +1/2$ - The data for this figure were obtained with a *Wolfram Mathematica* script based on appendix C.2 of Michael Gehm's PhD thesis [40].

2.5 | Collisional Properties

Though Lithium was among the first elements to be cooled to Bose-Einstein condensation, the early Lithium experiments suffered from long cycle times on the order of ca. $200\,\mathrm{s}$ and only small atom numbers of ca. 1×10^4 in the condensate [41] due to the small and attractive interactions of the used state. Modern experiments however achieve much faster cycle times (as fast as $11\,\mathrm{s}$ [42]) and much larger atom numbers (up to 2.7×10^6 [42]), by precisely engineering the experimental cycle to overcome the unique challenges that are posed by the collisional properties of ^{7}Li. Here, we want to discuss the key aspects that need to be considered when cooling Lithium.

2.5.1 Small and Attractive Triplet Scattering Length

At typical densities and temperatures in cold atom experiments, it is reasonable to focus on binary collisions involving only two atoms [25]. The two colliding atoms can either approach each other with their unpaired spins parallel ($\boldsymbol{S} = \boldsymbol{S}_1 + \boldsymbol{S}_2 = 1$) or anti-parallel ($\boldsymbol{S} = \boldsymbol{S}_1 + \boldsymbol{S}_2 = 0$). For parallel spins, there are three possible linear combinations for a symmetric spin wavefunction while there is only one possible anti-symmetric spin wavefunction for the anti-parallel case. Thus the two cases are called triplet ($\boldsymbol{S} = 1$) and singlet ($\boldsymbol{S} = 0$). Since the overall electronic wavefunction needs to be anti-symmetric, both cases require different symmetries of the respective spatial wavefunctions. For the singlet, the spatial wavefunction has to be symmetric, and for the triplet, the spatial wavefunction has to be anti-symmetric. As a result, the corresponding molecular potentials look vastly different. For ^{7}Li-^{7}Li collisions, the interaction potential is some linear combination of these singlet and triplet potentials. The exact linear combination depends on the involved states (and the magnetic field).

As the phase-space density approaches one, the scattering problem can be tackled with the so-called partial wave treatment [43]. For an incoming particle represented by a plane wave in the z-direction with wavenumber k that is scattered off a spherical atomic potential $V(r)$ the asymptotic form of the wavefunction can be expressed in the relative coordinate r and the reduced mass μ as

$$\psi(\boldsymbol{r}) \approx e^{ikz} + f(\theta)\frac{e^{ikz}}{r}, \tag{2.15}$$

where we can write an expansion in terms of spherical waves with angular momentum l

$$f(\theta) = \sum_{l=0}^{\infty}(2l+1)\left(\frac{e^{2i\delta_l}}{2ik}P_l(\cos\theta)\right), \tag{2.16}$$

where $P_l(\cos\theta)$ are the Legendre polynomials and δ_l is the spatial phase shift for each partial wave. At low temperatures, only the partial wave with $l = 0$ contributes to the scattering process. We thus speak of s-wave scattering in this regime. We can then define the s-wave scattering length a that can be used to calculate the scattering cross-section σ

$$a = -\lim_{k\to 0}\frac{\delta_0}{k} \tag{2.17}$$

$$\sigma = 8\pi a^2. \tag{2.18}$$

With this we can determine the two-body collision rate for elastic collisions

$$\Gamma_{\text{el}} = n\sigma v, \tag{2.19}$$

with the atomic density n and the mean velocity v. As described above, the scattering length for a given state is a linear combination of the singlet and triplet scattering lengths a_{S} and a_{T}. The scattering lengths of the singlet and triplet for ^{7}Li are given in table 2.7.

Table 2.7: Singlet and triplet s-wave scattering lengths for ^{7}Li.

Property	Symbol	Value	Ref.
Singlet s-wave scattering length	a_{S}	$33(2)\,a_0$	[44]
Triplet s-wave scattering length	a_{T}	$-27.6(5)\,a_0$	[44]

Both values are small compared to the case of other alkali elements like Rubidium. The rethermalization of the atoms is mediated via elastic collisions. Hence, low scattering lengths result in slow rethermalization rates, and thus limit the speed of the evaporation process. One can boost the rethermalization rate by increasing the density of the cloud. The easiest way to do this is to use a magnetic quadrupole trap. Since the $|1,-1\rangle$-state exhibits a sign change of the energy shift around ca. $150\,$G (see figure 2.3), it is advisable to use the $|2,2\rangle$-state from the $F = 2$-manifold. This doubly spin-polarized state interacts via a pure triplet potential and hence $a_{|2,2\rangle} = a_{\mathrm{T}}$. Thus the scattering length is not only small but also negative. These attractive interactions cause the forming condensates to be unstable and thus the overall atom number in the condensate is limited [41]. Additionally, the triplet scattering length exhibits a temperature-dependent zero-crossing at around ca. $10\,$mK [45] due to the Ramsauer-Townsend effect. Since the temperatures in the magneto-optical trap (MOT) are typically only one order of magnitude below this limit, further sub-Doppler cooling is required before effective evaporative cooling can be carried out.

2.5.2 Large Three-Body Loss Coefficient

While compressing the trap to increase the density is a feasible way to speed up the evaporation process, it can also cause issues due to three-body losses. While the gain in elastic collision rate scales with the density n as $\Gamma_{\mathrm{el}} \propto n$, the three body-losses scale as $\sigma_3 \propto n^2$. This puts a limit to an experimentally suitable density. For ^{7}Li, the three-body loss coefficient is $1 \times 10^{-27}\,\mathrm{cm}^3/\mathrm{s}$ [46] which is two to three orders of magnitude higher than for ^{87}Rb $4.3 \times 10^{-29}\,\mathrm{cm}^3/\mathrm{s}$ [47] and ^{23}Na $1.1 \times 10^{-30}\,\mathrm{cm}^3/\mathrm{s}$ [48]. Thus, the density should be kept below $1 \times 10^{13}\,\mathrm{cm}^{-3}$ in order to keep the three-body losses negligible during typical evaporation timescales. In order to manage both the three-body losses and the elastic collisions it is helpful to adiabatically compress and decompress the trap during the evaporation process.

2.5.3 Feshbach Resonances

Next to the disadvantageous collissional properties discussed above, the $F = 1$-manifold of ^{7}Li also features broad Feshbach resonances that can be used to tune the interaction strength between either identical atoms or also spin mixtures. Figure 2.8 shows the resonances for intra-spin collisions and figure 2.9 shows the Feshbach resonances for spin mixtures. The data for these figures were kindly provided by Randall Hulet and Ruwan Senaratne and published in [26]. To our knowledge, there are no Feshbach resonances in the $F = 2$-manifold.

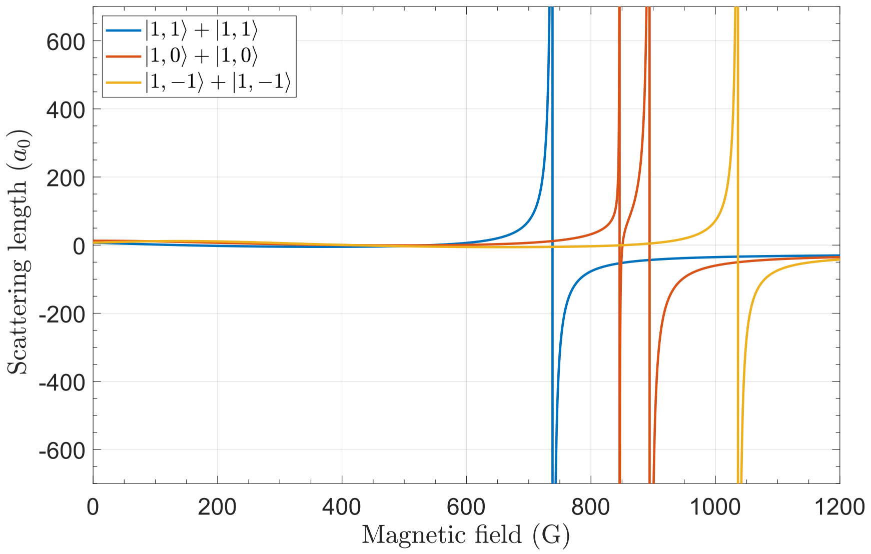

Figure 2.8: Feshbach resonances for intra-spin collisions in the lowest hypferfine state - The scattering length data were provided by Randall Hulet and Ruwan Senaratne and published in [26].

In the vicinity of a Feshbach resonance, the s-wave scattering length can be parametrized by

$$a(B) = a_{\mathrm{bg}} \left(1 - \frac{\Delta B}{B - B_0}\right), \tag{2.20}$$

where a_{bg} is the background scattering length at zero field, ΔB is the magnetic field width and B_0 is the position of the resonance. We summarize the width and position of the resonances together with the position of the zero-crossings in table 2.8.

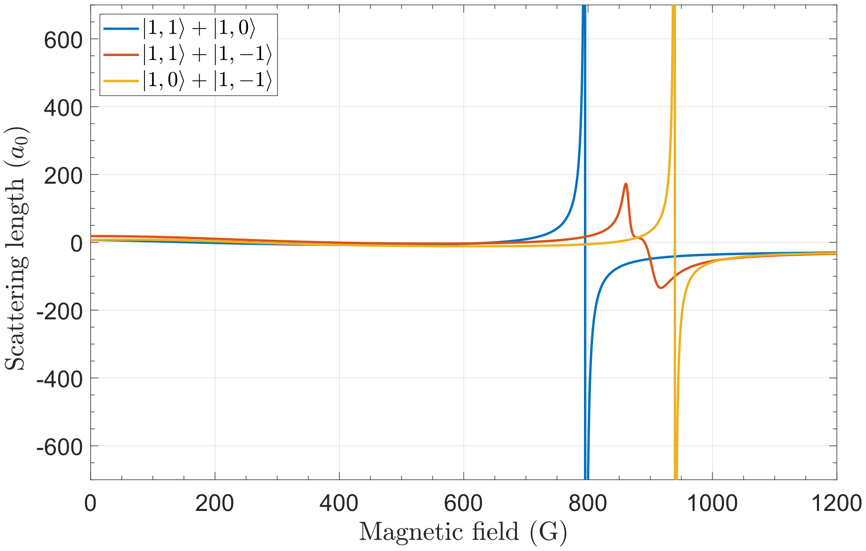

Figure 2.9: Feshbach resonances for spin mixtures in the lowest hypferfine state - The scattering length data were provided by Randall Hulet and Ruwan Senaratne and published in [26].

Table 2.8: Position B_0 and width ΔB of the Feshbach resonances and zero-crossing magnetic field B^* of all possible spin-mixtures in the lowest hyperfine-state of ^{7}Li. The scattering length data were provided by Randall Hulet and Ruwan Senaratne and published in [26].

Spin mixture	B_0 (G)	ΔB(G)	B^* (G)
$\|1,1\rangle + \|1,1\rangle$	738.3	194.7	543.6
$\|1,0\rangle + \|1,0\rangle$	846.0	4.8	576.2
	894.2	43.4	850.8
$\|1,-1\rangle + \|1,-1\rangle$	1036.3	182.6	853.7
$\|1,1\rangle + \|1,0\rangle$	795.2	143.5	651.7
$\|1,1\rangle + \|1,-1\rangle$	890.8	196.6	694.2
$\|1,0\rangle + \|1,-1\rangle$	939.6	100.7	838.9

2.6 | Magic Wavelengths

In modern ^{7}Li experiments, the atoms are typically pre-cooled close to degeneracy in a magnetic trap before they are transferred into an optical dipole trap [49]. They are then evaporatively cooled to degeneracy in the vicinity of a Feshbach resonance [50, 51, 42]. There are also approaches to all-optical cooling of Lithium, where the dipole trap is directly loaded from a MOT [52, 53]. Optical dipole traps could in the future be combined with laser-cooling on the $2S - 2P$ UV transition. There is a so-called magic wavelength at ca. $1070\,$nm where the differential AC stark shift between both states vanishes [54]. A similar approach has already been successfully implemented for the fermionic isotope ^{6}Li [55].

CHAPTER 3

The ^{7}Li BEC Machine

The machine was originally designed as a quantum gas microscope for both fermionic ^{6}Li- and bosonic ^{7}Li-atoms. At the beginning of the author's work in the lab in 2017, sub-Doppler laser cooling for both isotopes had already been implemented. We then focused on the all-optical creation of degenerate ^{6}Li-gases. We were able to produce both molecular BECs and degenerate Fermi gases in all three lowest hyperfine states within cycle times of ca. $15\,$s. The corresponding sequences and the latest progress towards single lattice-site resolved fluorescence imaging of ^{6}Li is described in [56–59]. In June 2020, we switched gears working towards constructing a matter-wave microscope focusing on the bosonic isotope ^{7}Li. The following chapter introduces the experimental apparatus and the main experimental techniques towards reaching quantum degeneracy with ^{7}Li. The results and techniques described in this chapter were carried out by the author in close collaboration with Justus Brüggenjürgen under the supervision of Christof Weitenberg.

3.1 | The Path to Degeneracy

With the switch of isotopes, we had to overcome several new experimental obstacles, that were less pronounced in ^{6}Li. Firstly, the crossed optical dipole trap (ODT) in which we produced the molecular BEC of ^{6}Li, was implemented using a diode pumped linearly polarized continuous-wave multimode Ytterbium fiber laser[1] with a spectral width of $5\,$nm centered around $1070\,$nm[2]. After loading the bosonic atoms into this trap, we observed severe particle loss, that impeded any efforts in further evaporative cooling. We attribute this heating to unwanted Raman processes caused by unfortunate choices of the intersection angles and the multimode nature of the laser source. We know from other groups, that they also encountered issues with trapping ^{7}Li in a multimode crossed dipole trap[3]. As a consequence, we decided to set up a new optical dipole trap using a single mode laser. In addition to this, we also had to manage the disadvantageous collisional properties of ^{7}Li. During evaporative cooling, the particles with the most kinetic energy are removed and the kinetic energy is then redistributed via elastic scattering processes. The elastic scattering cross-section is given by $\sigma = 8\pi a^2$, where a is the so-called scattering length. The singlet and triplet scattering lengths of ^{7}Li are $a_{\mathrm{S}} = (33 \pm 2)\, a_0$ and $a_{\mathrm{T}} = (-27.6 \pm 0.5)\, a_0$ [44], where a_0 is the Bohr radius. These rather small values (ca. three times smaller than for Rubidium) cause the rethermalization process during evaporative cooling to be quite slow. One can mitigate this by increasing the density n of the cloud and thus increasing the elastic collision rate $\Gamma_{\mathrm{el}} = n\sigma v$, with v being the mean

---

[1] IPG Photonics: YLR-100-LP-A

[2] For more details regarding this ODT setup, see [56–58]

[3] Private communication with Jesse Amato-Grill, Ketterle Group, 2021

velocity. However, while the elastic collisions scale as $\sigma_2 \propto n$, the three-body losses scale as $\sigma_3 \propto n^2$. This puts a limit to an experimentally suitable density. For ^{7}Li, the three-body loss coefficient is $1 \times 10^{-27}\,\mathrm{cm^3/s}$ [46] which is two to three orders of magnitude higher than for ^{87}Rb $4.3 \times 10^{-29}\,\mathrm{cm^3/s}$ [47] and ^{23}Na $1.1 \times 10^{-30}\,\mathrm{cm^3/s}$ [48]. Thus, we want to keep the density below $1 \times 10^{13}\,\mathrm{cm^{-3}}$ in order to keep the three-body losses negligible during typical evaporation timescales.
To the best knowledge of the author, there are to this day nine experimental groups that achieved Bose-Einstein condensation of ^{7}Li. A list of the groups with some key parameters is displayed in table 3.1.

Table 3.1: List of experimental groups that realized BECs of ^{7}Li.

Experimental Group	Evaporation to Degeneracy	Final Particle Number $\times 10^3$	References
Hulet	cloverleaf trap + single beam ODT	500	[60–62]
Kasevich	Ioffe-Pritchard trap	60	[63]
Khaykovich	all-optical	0.7	[52]
Salomon	Ioffe-Pritchard trap + single beam ODT	60	[64]
Horikoshi	all-optical, sympathetic cooling with ^{6}Li	30	[53]
Ketterle	plugged quadrupole trap + cODT	500	[50, 45, 65]
Weld	plugged quadrupole trap + cODT	300	[51, 66–68]
Choi	plugged quadrupole trap + cODT	2700	[42]
Weitenberg/Sengstock	plugged quadrupole trap + cODT	100	/

In recent years, the groups of Wolfgang Ketterle, David Weld and Jae-yoon Choi all took a quite similar approach that we also follow in our experiment: We start with initial trapping of the atoms in a MOT, followed by sub-Doppler cooling in a Gray Molasses (GM). We then optically pump the atoms to the $|F = 2, m_F = 2\rangle$-state and load them into an optically plugged magnetic quadrupole trap or short magnetic trap (MT). We perform evaporative cooling via an RF transition to the untrapped $|F = 1, m_F = 1\rangle$-state, while adiabatically decompressing the trap. Before reaching degeneracy, we load the atoms into our crossed optical dipole trap, where we perform an adiabatic state transfer to the $|F = 1, m_F = 1\rangle$-state. We ramp up a bias field close to the Feshbach-resonance of said state and perform the final evaporation by decreasing the trap depth in the ODT. The following chapter elaborates the main steps towards reaching quantum degeneracy. For these stages the respective particle number, temperature and Phase-Space Density (PSD) are displayed in table 3.2.

Table 3.2: Experimental stages and corresponding particle number, temperature and PSD.

Experimental Stage	Particle Number	Peak density n_0 (cm^{-3})	Temperature T (µK)	PSD $\rho_0 0$
MOT	6×10^8	8×10^9	3300	1×10^{-8}
cMOT	6×10^8	3×10^{10}	800	4×10^{-7}
GM	5×10^8	3×10^{10}	35	3×10^{-5}
MT Load	4×10^8	5×10^{12}	320	2×10^{-4}
MT Evaporation	2×10^6	2×10^{13}	16	1×10^{-1}
ODT Load	1×10^6	4×10^{12}	24	1×10^{-2}
ODT Evaporation	1×10^5	2×10^{12}	0.22	4

3.2 | The Experimental Apparatus

We introduce our experimental platform by giving an overview of the vacuum chamber as well as the main coils which have been assembled before the author started his thesis. A CAD drawing of the compact vacuum chamber is displayed in figure 3.1. During this thesis, we improved the switching circuits of the coils and developed new RF antennas to address internal states of ^{7}Li which are also discussed in the section. We close with an overview of the experiment control infrastructure.

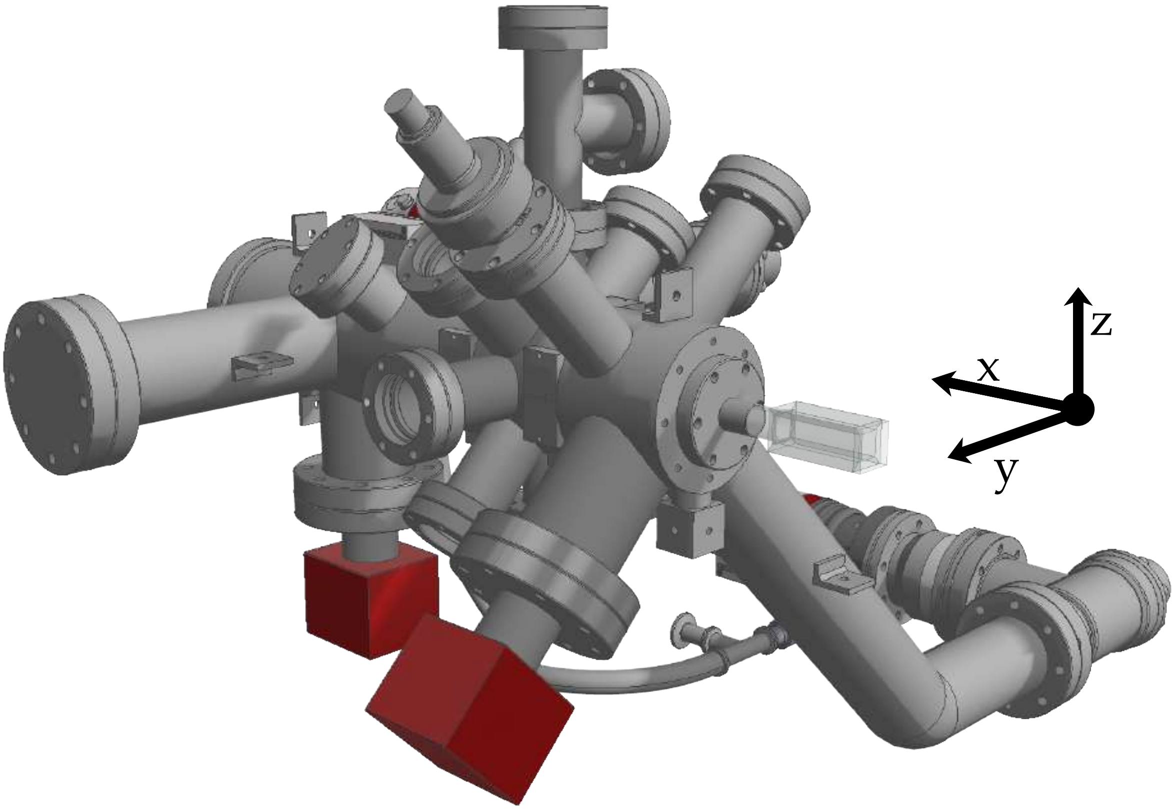

Figure 3.1: CAD drawing of the vacuum chamber - The compact 2D/3D-MOT setup allows for a compact design, where the atoms are captured and imaged in a glass cell without further atom transport after the 3D-MOT phase. Turbo pumps, ion getter pumps and gauges are used to create and monitor the extreme-high vacuum (XHV) conditions. Figure adapted from [57].

3.2.1 The Vacuum Chamber

For quantum simulation with cold atoms we operate on a cycle-based experimental scheme. A degenerate atomic sample is created every few seconds, which can then be used to study a sandbox Hamiltonian of choice. These Hamiltonians can for example be engineered by shaping the atoms' potential landscapes using laser beams or by exposing them to DC or AC magnetic fields in order to address internal states. For these purposes good optical access to the atoms is essential. At the same time the machine must be capable to gather a lot of statistics in a reasonable amount of time. For this it is crucial to achieve high repetition rates and thus short cycle times. In recent years the cycle times have been pushed to ever lower limits and now reach even the sub-second regime [69, 70].

When our machine was in the early planning stages in 2014, short cycle times and robustness as well as good optical access were the main motivation for the design of the vacuum chamber. Here, we provide a short overview of the chamber. More detailed discussions on certain design choices can be found in [71, 57, 58]. For maximum optical access the atoms are trapped and imaged in a glass cell (science cell)[4]. To prevent the faces of the glass cell from getting coated with a film of Lithium atoms and thus reducing transmission of relevant optical wavelengths, the cell has to be placed out of the direct line of sight from the atomic source. For Lithium experiments, this is typically done by first loading the atoms in a 3D-MOT using a Zeeman slower, followed by a transport in a moving magnetic or optical trap. However this approach not only requires additional vacuum components, lasers and magnetic field coils, but it can also induce heating and particle loss. One can avoid these drawbacks by using a 2D-MOT instead of a Zeeman slower. 2D-MOTs have been a common first stage for multiple laser-cooling experiments with other chemical elements such as Potassium or Rubidium [73–75] for ca. two decades. In 2009, it was shown that this technique also works for Lithium atoms and achieves comparable 3-dimensional (3D)-MOT loading rates to using a Zeeman slower [76]. Our vacuum chamber is a compact 2D/3D-MOT setup, a side view of which is depicted in figure 3.2.

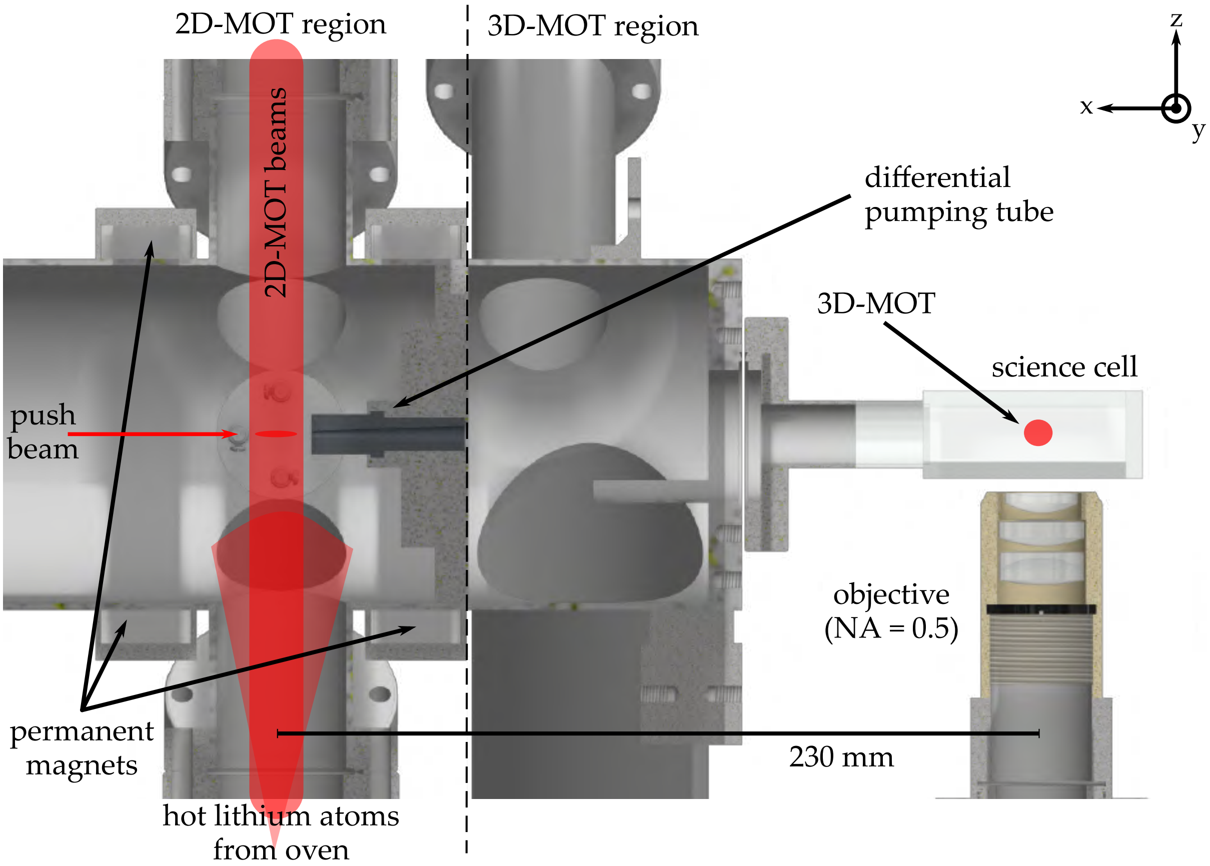

Figure 3.2: Sideview of the vacuum chamber - The vacuum system is divided into two parts. In the 2D-MOT region (left side) the atoms are released from the oven and then transversely cooled in a 2D-MOT. They are then transferred to the 3D-MOT region (right side) via resonantly scattering them through a differential pumping tube. Here the atoms get trapped in a 3D-MOT inside of a glass cell. The high-resolution microscope objective was used to image cold gases of ^{6}Li. Picture taken from [58].

---

[4] Cold quanta: custom coating. See [72].

This setup allows us to place the oven as the atomic source perpendicular to the line of sight between the 2D-MOT and the 3D-MOT. Thus we are able to omit any further atom transport after capturing the atoms in the 3D-MOT inside the glass cell. To not be limited by collisions with the background gas, the chamber is split into two regions, that are separated via a differential pumping tube. It is a conical graphite tube that can sustain a pressure difference of at least two orders of magnitude between both regions [57]. The heart of the 2D-MOT region is a stainless steel DNCF 40 8-way cross, at the bottom of which the oven is placed. It is filled with ca. $20\,\text{g}$ (footnote [5]) of a 50:50 mixture of ^{6}Li/^{7}Li and heated to ca. $690\,\text{K}$. At this temperature the vapor pressure of Lithium rises above 1×10^{-2} mbar (see figure 2.1) such that the atoms are released from the oven. This flux causes the pressure in the 2D-MOT chamber to increase to ca. 1×10^{-10} mbar. The 2D-MOT beams are shone into the chamber through viewports under $\pm 45^\circ$ with respect to the vertical z-axis. The magnetic field gradient for the 2D-MOT is created by eight stacks of permanent magnets[6] that are externally screwed onto the vacuum chamber. In order to maximize the loading rate of the 3D-MOT, the distance between the 2D-MOT and the glass cell is as small as possible ($23\,\text{cm}$). A resonant pushing beam is shone onto the atoms and enhances the number of atoms that are transferred to the 3D-MOT. The pressure here is ca. 1.2×10^{-11} mbar. By switching off the 2D-MOT beams and the pushing beam, the atom flux between both regions can be shut off. The 3D-MOT is created inside the glass cell which is depicted in figure 3.3.

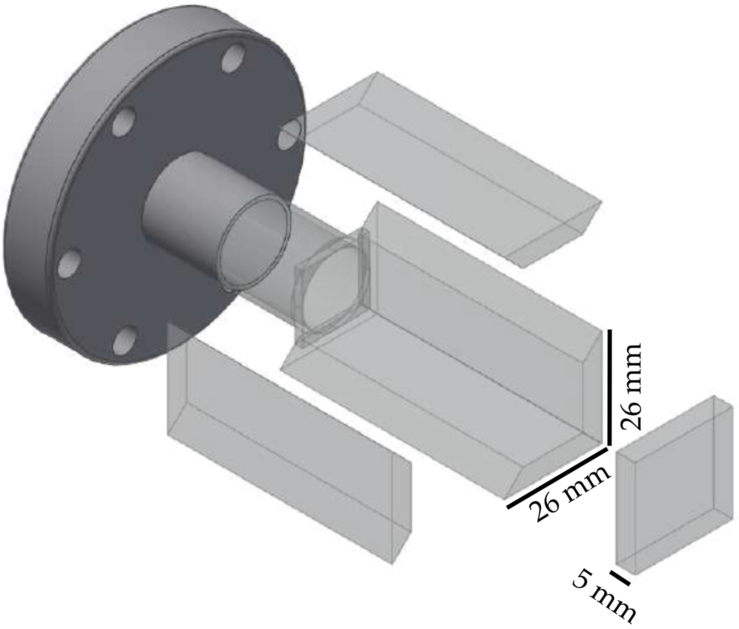

Figure 3.3: 3D explosion plot of the science cell - The glass cell consists of four trapezoidal walls and a square front. All of the walls are $5\,\text{mm}$ thick and are anti-reflection (AR) coated for all relevant wavelengths from both sides. The front wall covers a $26 \times 26\,\text{mm}^2$ area, the central $16 \times 16\,\text{mm}^2$ of which are AR coated. Figure taken from [57]

It is manufactured from a borosilicate glass[7] that is AR coated for all relevant wavelengths[8] [72] from both sides. The coils that generate the quadrupole field for the 3D-MOT and bias fields for addressing Feshbach resonances are discussed in the following section 3.2.2.

---

[5] The oven was first filled with ca. $3\,\text{g}$ of Lithium in 2016 which lasted for three years

[6] Eclipse Magnetics Ltd: N750-RB

[7] Schott: Borofloat 33

[8] The relevant wavelengths for everything discussed in this thesis are: $671\,\text{nm}$, $660\,\text{nm}$ and $1064\,\text{nm}$

Details on the chamber assembly and evacuation can be found in the PhD thesis of Andreas Kerkmann [57]. We note that apart from the Lithium oven, there is also a Rubidium dispenser in the vacuum chamber. All the optics and magnetic coils are designed such that we could also study ^{85}Rb/^{87}Rb or mixtures of Lithium and Rubidium.

3.2.2 Magnetic Field Coils

Magnetic fields play an essential role in multiple steps of every cold atoms experiment. Electromagnets are for example used in Zeeman slowers or magneto-optical traps. Bias fields are applied to define a quantization axis or to access the Zeeman or Paschen-Back regime and given the existence of a magnetic Feshbach resonance can even be used to tune the interaction strength of the atoms. In our experiment we can divide the electromagnets into two categories. The main coils are used to create quadrupole fields for the MOT and the magnetic trap, to generate a magnetic field gradient in the $x - y$ plane and to apply fields of up to ca. $1500\,$G to address Feshbach resonances. They are operated with currents of up to $200\,$A and thus require a dedicated water cooling. On the other hand we have multiple offset coils that don't require a dedicated water cooling and operate at maximum at $5\,$A. They are used to apply small bias fields, shield the atoms from the earth's magnetic field and finely tune the position of the 2D-MOT.

The Main Coils

The main coils consist of two pairs of coils that are roughly oriented in Helmholtz configuration along the z-axis as well as a single coil along the x-axis. A 3D rendering of the coils around our glass cell is depicted in figure 3.4. The single coil (Tilt coil) was used in our previous work with ^{6}Li atoms to provide a magnetic field gradient in the $x - y$ plane after preparation of a single atomic layer in an accordion lattice (see [58] for further details). It is not used in this work.

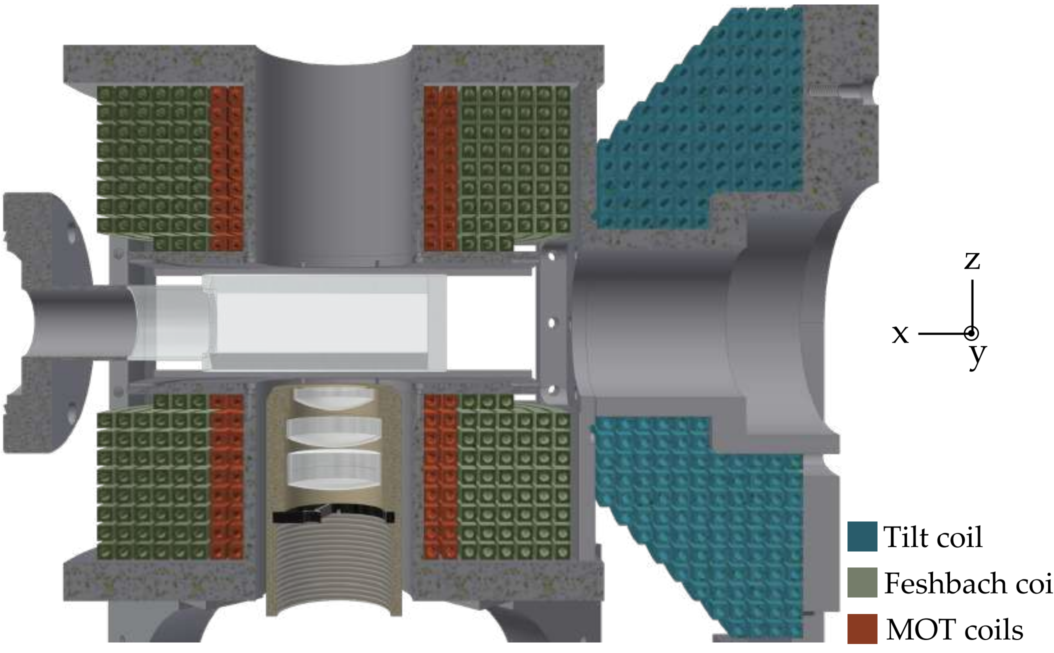

Figure 3.4: Side-cut through the magnetic field coils surrounding the glass cell - They are all wound of the same $4 \times 4\,\text{mm}^2$ cross-section hollow-core copper wire. Figure taken from [57].

The two coil pairs can either be operated in Helmholtz (HH) or anti-Helmholtz (AH) configuration. The outer coil pair (Feshbach coils) is used to generate part of the quadrupole field for the MT and the bias field to address the Feshbach resonances of ^{7}Li. The inner coil pair (MOT coils) produces the quadrupole fields for the MOT and the magnetic trap. It can also be used to cancel the residual curvature of the Feshbach coils when operated in Helmholtz mode. The main coils were designed and simulated by Michael Hagemann and manufactured by the company *Oswald*. See [77, 58] for a detailed discussion of the design, the properties of the coils, the possible field combinations and the water cooling infrastructure. The key properties of the main coils are summarized in table 3.3. The coil design enables us to apply bias fields of up to $1500\,\text{G}$ and field gradients of up to $520\,\text{G/cm}$ while maintaining good optical access to the atoms. In principle, the relatively low inductance of the coils allows for fast switching times. In the past, we were able to switch fields of $\sim 1180\,\text{G}$ within $< 100\,\mu\text{s}$ [57]. However, the insulation of the coils got damaged such that the induction voltages cause an electric arc from the coils to their mount if we try fast switching of the currents now. Thus, we currently only switch off the current slowly within $\sim 10\,\text{ms}$.

Table 3.3: Magnetic field strengths, gradients, residual curvatures and inductance of the main coils for Helmholtz (HH) and anit-Helmholtz (AH) mode. The residual curvature is calculated for ^{7}Li. The data is taken from [58].

	Feshbach coils	MOT coils
Bias field in HH mode	$5.86\,\text{G/A}$	$1.81\,\text{G/A}$
Axial field gradient in AH mode	$1.71\,\text{G/(cm A)}$	$0.90\,\text{G/(cm A)}$
Axial curvature ω_z in HH mode	$2\pi \times 1.16\,\text{Hz}/\sqrt{\text{G}}$	$2\pi \times 2.21\,\text{Hz}/\sqrt{\text{G}}$
Radial curvature ω_r in HH mode	$2\pi \times 0.82\,\text{Hz}/\sqrt{\text{G}}$	$2\pi \times 1.56\,\text{Hz}/\sqrt{\text{G}}$
Inductance at $1\,\text{kHz}$	$160\,\mu\text{H}$	$12\,\mu\text{H}$

In his simulations, Michael Hagemann treated the coils as perfect rings. The resulting field centers perfectly coincide in the origin of the simulation. In reality, the centers of the Helmholtz and anti-Helmholtz field configurations don't overlap. We observed this by measuring the position of the magnetic trap centers created by the combination of the MOT and Feshbach coils or by the respective coils alone. Additionally, the centers of the residual curvatures in HH mode are also at different positions in space as can be measured by releasing cold clouds from the dipole trap at high fields. These observations can be explained by taking into account the helicity of the real coils. In his Bachelor's thesis, Richard von Wurmb simulated our coils including the helicity and studied the influence of small imperfections in the manufacturing process [78]. His results can explain the observed position deviations of up to $500\,\mu\text{m}$. A possible way to mitigate these effects is to cancel the residual field curvature at high fields by applying a bias field with the MOT coils that counteracts the bias field generated by the Feshbach coils. Since the field curvature generated by the inner lying MOT coils is higher than the curvature caused by the Feshbach coils the overall curvature can be flattened while still maintaining fields of up to ca. $800\,\text{G}$ [58]. This technique is already in use in other Lithium experiments [66] but we have not implemented it yet.

Switching High Currents

The basic concept of switching the high currents that generate the magnetic fields in our experiment is described in Michael Hagemann's PhD thesis [58]. We have however improved the setup since his thesis and quickly summarize the results here. Both coils are powered by identical power supplies[9] that can deliver up to $200\,\mathrm{A}$. For switching the current through the MOT and Feshbach coils, we use identical electric circuits which are depicted in figure 3.5. We use a dual channel insulated-gate bipolar transistor (IGBT)[10] to implement H-bridges. With these we can not only switch the current on and off but also change the direction of the current through one of the coils. This allows us to switch between AH and HH mode independently on both coil pairs. The current through the coils is monitored with current transducers[11] and the power supplies are protected against high induction voltages with diodes[12]. In order to quickly dissipate the induction voltages that arise when switching high magnetic fields, we put varistors[13] in parallel to each coil.

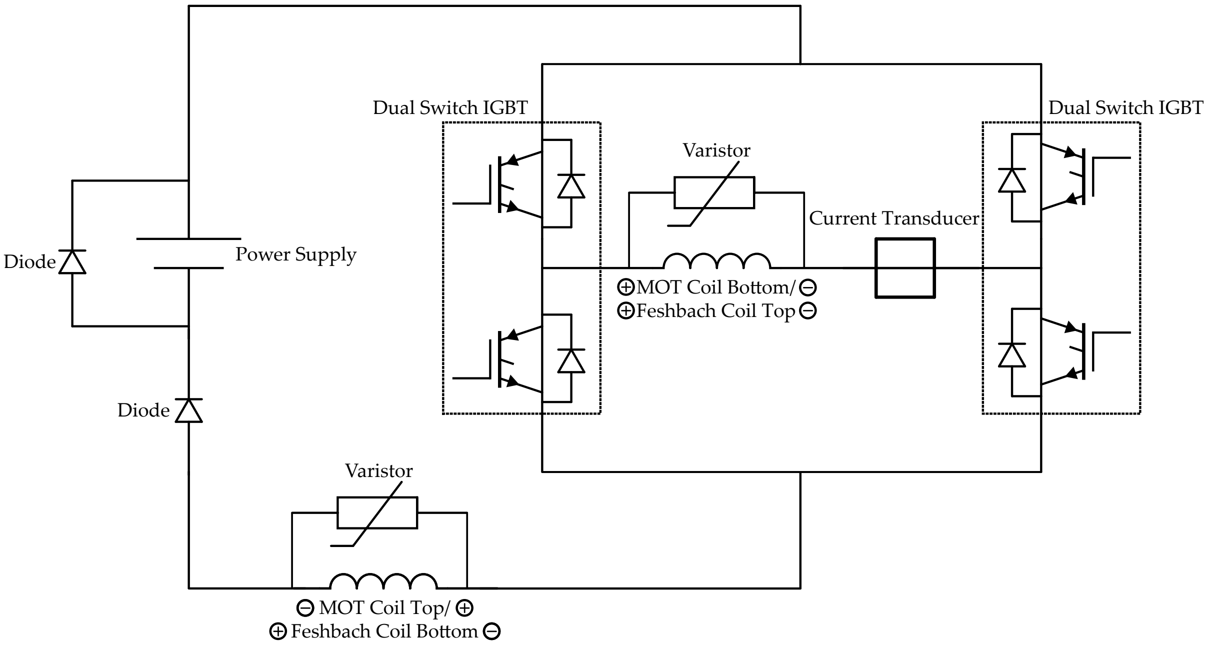

Figure 3.5: Circuit for switching the current through the MOT and the Feshbach coils - An H-bridge enables us to not only switch the current on and off but also switch between AH and HH configuration. The "+" and "-" labels at the coils depict the randomly chosen polarity of the coils in the lab.

When we prepared atoms in a magnetic trap of the combined AH fields from both coil pairs, we noticed that we lost more atoms from the trap than expected. We found the issue to be RF noise in the lab that coupled to the atoms and induced unwanted spin-flips into untrapped states. The main contribution to this noise was caused by the IGBT gate drive units[14] that were directly soldered onto the IGBTs. They feature built-in DC-DC converters that introduced the RF noise at low frequencies and coupled it directly onto the main coils that served as RF antennas. This caused an effective anti-evaporation, removing the atoms with the least kinetic energy from the trap. To avoid this, we removed the DC-DC converters and replaced them with $24\,\mathrm{V}$ linear power supplies and $8\,\mathrm{V}$ voltage regulators[15]. Figure 3.6 shows the noise emitted from the main coils that we measured with a self-made pick-up antenna in the frequency range between $15\,\mathrm{kHz}$ and $10\,\mathrm{MHz}$ before and after substituting the DC-DC converters with our custom solution. After the exchange the lifetime of the atoms in the magnetic trap drastically improved.

---

[9] Delta Elektronika: SM30-200
[10] Mitsubishi Electric: CM450DX-24T
[11] LEM: HTA600-S
[12] Semikron: SKKE 600
[13] TDK Electronics: B40K75
[14] Isahaya Electronics Corporation: VLA536-01R
[15] STM: L7808

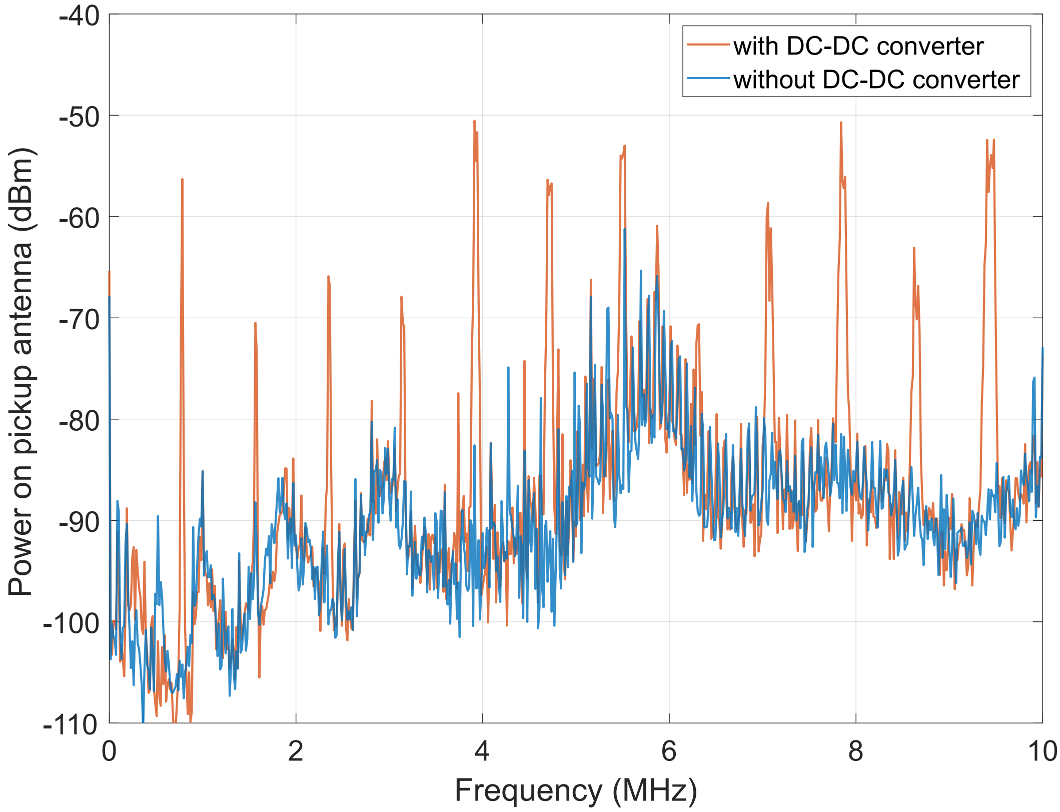

Figure 3.6: Noise spectra of the IGBT drivers - The noise was coupled directly onto the main coils. We measure the spectra before and after exchanging the built-in DC-DC converters with a custom solution. The signal was recorded with a self-made pick-up antenna and analyzed with a spectrum analyzer[16].

Offset Coils

We use offset coils to apply additional magnetic fields at two stages in the experiment. For the 2D-MOT, the main gradient field is realized by eight stacks of permanent magnets which are difficult to precisely align. We use the 2D offset coils to apply bias fields to shift the position of the 2D-MOT in front of the differential pumping tube. The 2D offset coils are made out of a ribbon cable with 20 cores[17] that is wound eight times around a 3D-printed mount such that there are 160 windings per coil in total. Four of these coils are pairwisely attached to the 2D-MOT vacuum chamber as close to each other as possible. Both of the coil pairs are supplied by the same four channel power supply[18] and are powered with maximum $5\,\mathrm{A}$. A photograph of one of the coils and its 3D-printed mount is shown in figure 3.7b. The 3D offset coils consist of three pairs of coils centered around the glass cell along each spatial direction. They are made of copper wire and are mainly supplied by an identical power supply as the 2D offset coils. At the maximum current of $5\,\mathrm{A}$ they can generate bias fields of up to ca. $4\,\mathrm{G}$ ($7\,\mathrm{G}$, $16\,\mathrm{G}$) and field gradients of ca. $1.1\,\mathrm{G/cm}$ ($1.5\,\mathrm{G/cm}$, $4.4\,\mathrm{G/cm}$) in the x- (y-, z-) direction. We mainly use them to shield the atoms from Earth's magnetic field but we could in principle also counteract residual gradient fields. One of the coil pairs along the z-direction is used to apply a bias field for the optical pumping into the $|F = 2, m_F = 2\rangle$-state before trapping the atoms in the magnetic trap and to maintain a quantization axis when loading the atoms from said magnetic trap into the optical dipole trap. This coil pair is powered by a bipolar power supply[19] because we need to change the direction of the field between both scenarios. A photograph of the offset coils around the glass cell is shown in figure 3.7a. Further details on the 3D offset coils can be found in Andreas Kerkmann's PhD thesis [57].

---

[16] Rohde & Schwarz: FSV-7

[17] Multicomp Pro: FBLA20-20-50

[18] Rohde & Schwarz: HMP4040

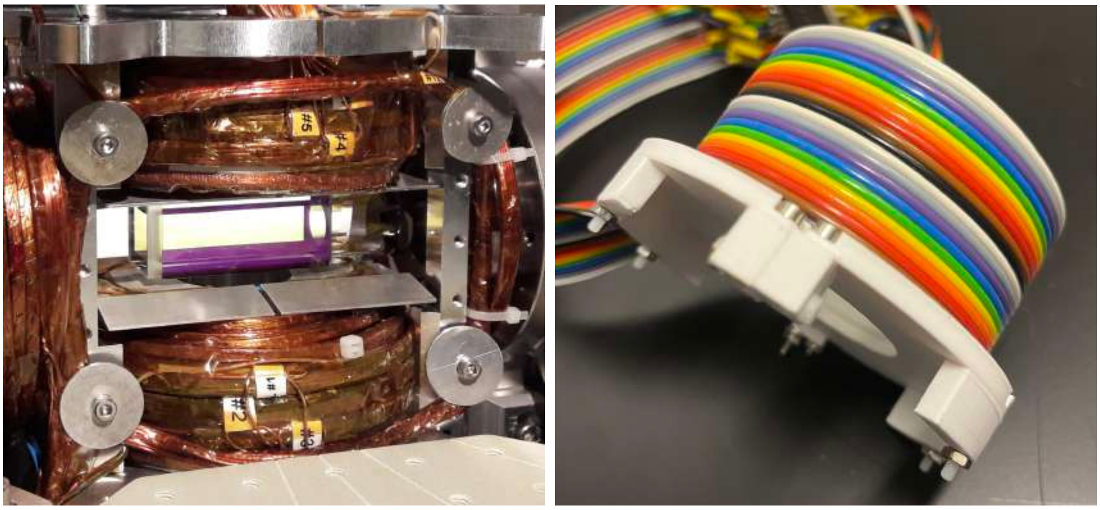

(a) (b)

Figure 3.7: Photographs of the 3D **(a)** and 2D **(b)** offset coils used in the experiment.

3.2.3 Radio Frequency Antennas

At various stages in our experiment cycle it is necessary to address the internal states of the atoms. During evaporation in the magnetic trap, we need to transfer the hottest atoms from the trapped $|F = 2, m_F = 2\rangle$-state to the untrapped $|F = 1, m_F = 1\rangle$-state. To keep this transition resonant with the hottest atoms as the whole sample cools down, we need to scan this transition frequency roughly from 950 MHz to 800 MHz. We thus require an RF antenna that has a reasonably good emission characteristic in this frequency range. For this purpose we use a conductor loop that was placed inside the cover plate of the main coil holder. It can be seen underneath the glass cell in figure 3.7a. The input return loss in the frequency range of interest is measured with a network analyzer[20] and is displayed in figure 3.8. Though this antenna is sufficient for the evaporation in the magnetic trap, the achieved Rabi frequencies are not adequate to perform fast and reliable state transfers at later stages of the experiment. To this end, we built two additional antennas with a narrow resonance centered around 813 MHz and 173 MHz respectively. The 813 MHz antenna is used to transfer the atoms from the $|F = 2, m_F = 2\rangle$-state to the $|F = 1, m_F = 1\rangle$-state at a small bias field (see section 3.5). The 173 MHz antenna can be used to quickly change the state and thus the interaction strength at high magnetic fields from $|F = 1, m_F = 1\rangle$ to $|F = 1, m_F = 0\rangle$ (see section 5.3).

---

[19] HighFinesse: BCS 4/12
[20] Rohde & Schwarz: ZVL13

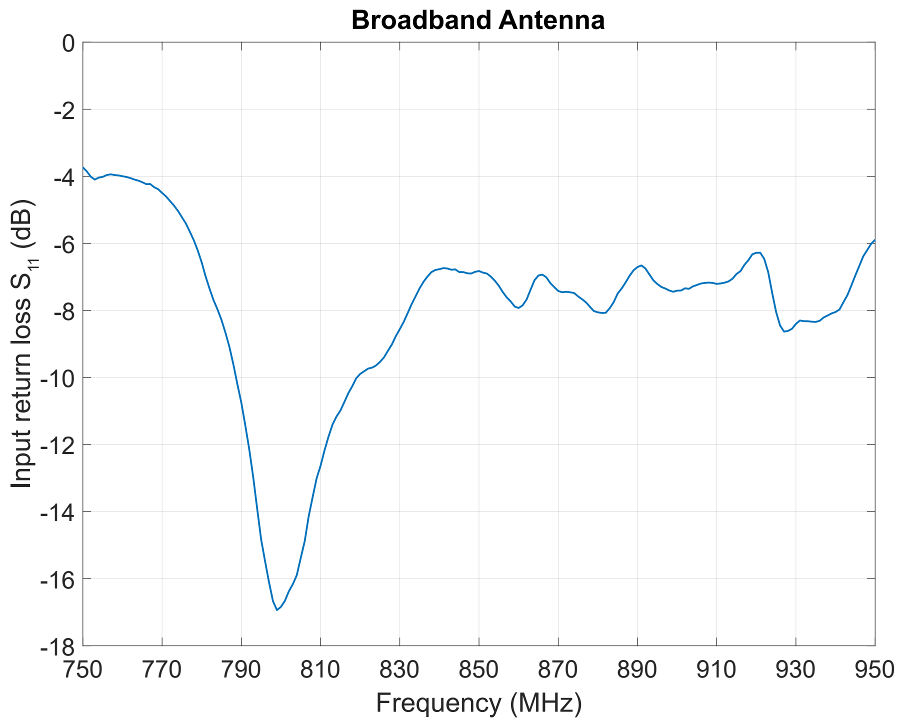

Figure 3.8: Input return loss of the broadband antenna that we use for evaporation in the magnetic trap.

Both antennas follow the same design which is a simple magnetic loop made out of $2\,\mathrm{mm}$ diameter copper wire. Its circumference is shorter than $\lambda/10$ (footnote [21]). We use two tunable plate capacitors to precisely optimize the antenna's resonances. They are installed in a 3D-printed mount that allows us to place the antennas as close to the atoms as possible. A photograph of the $173\,\mathrm{MHz}$ antenna as well as a sketch of the equivalent circuit are shown in figure 3.9.

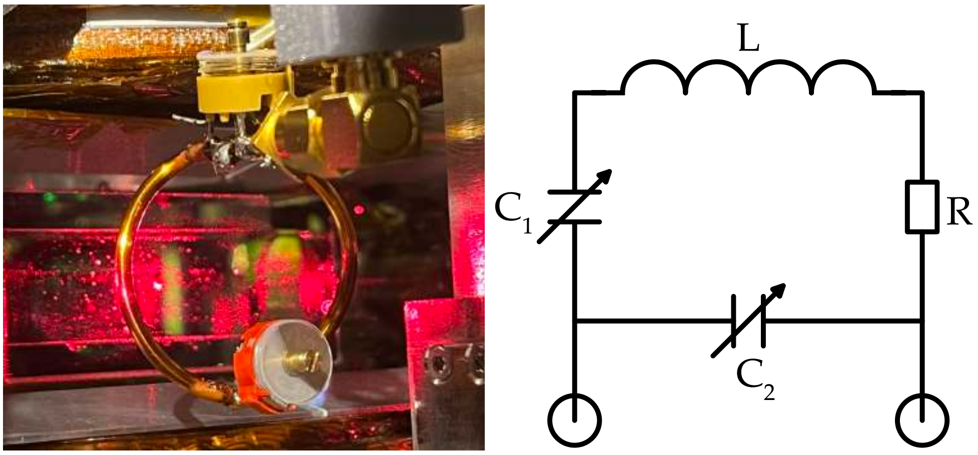

(a) (b)

Figure 3.9: Narrow-resonance RF antenna used for fast state transfers - **(a)** Photograph of the $173\,\mathrm{MHz}$ antenna built into the experiment and **(b)** sketch of the equivalent circuit of the antennas. We assume a simple RLC circuit with two tunable capacitors C_1 and C_2, the inductance L and resistance R of the loop.

Instructions on how to build and tune these types of antennas can be found in Tobias Petersen's Master's thesis [59]. We measure the input return loss for both antennas after installing them in the experiment and plot the results in figure 3.10. We achieve Rabi frequencies of up to ca. $2\pi \times 10\,\text{kHz}$ ($2\pi \times 7\,\text{kHz}$) at RF powers of $40\,\text{dBm}/10\,\text{W}$ ($35\,\text{dBm}/3\,\text{W}$) for the $813\,\text{MHz}$ ($173\,\text{MHz}$) antenna. In the future we might also add an antenna with a resonance around $210\,\text{MHz}$ to address transitions from $|F = 1, m_F = 0\rangle$ to $|F = 1, m_F = -1\rangle$.

---

[21] $12.5\,\mathrm{mm}$ for the $813\,\mathrm{MHz}$ antenna and $25\,\mathrm{mm}$ for the $173\,\mathrm{MHz}$ antenna

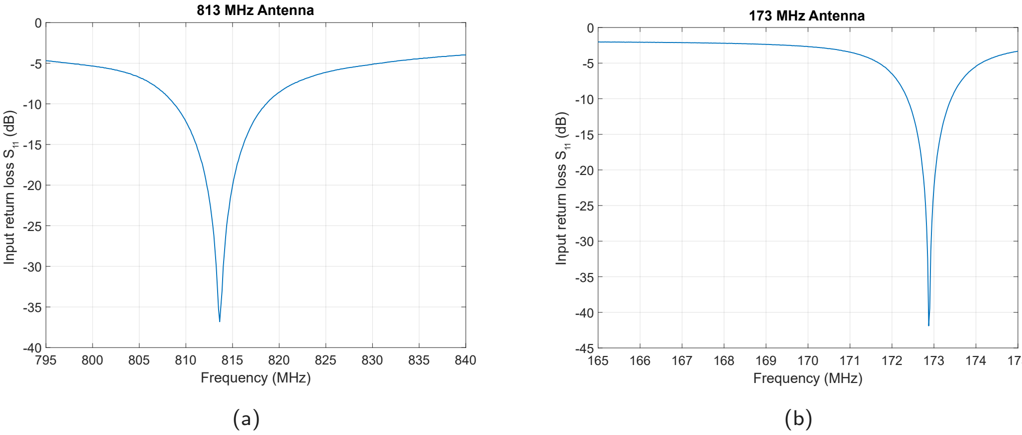

Figure 3.10: Measured input return loss of **(a)** the $813\,\text{MHz}$ antenna and **(b)** the $173\,\text{MHz}$ antenna after installing them at the experiment.

3.2.4 Experimental Control and Sequence Infrastructure

To program the experimental sequences we use an adapted version of the *Cicero Word Generator* [79]. It features a client program called *Cicero* with which we can design an experimental sequence in a graphical user interface (GUI) and a server program called *Atticus* which manages the execution of said sequence. When an experimental run is to be executed, the sequence information is sent via Transmission Control Protocol/Internet Protocol (TCP/IP) from *Cicero* to the server computer that runs *Atticus*. *Atticus* then generates output buffers that are sent either directly via Recommended Standard 232 (RS-232) connections or as virtual instrument software architecture (VISA) commands via TCP/IP to the hardware devices in the lab. The most important of these is the *ADwin Pro II* system[22]. It provides multiple analog[23] and digital[24] real-time outputs with a minimum time resolution of $1\,\mu\text{s}$. All timing-sensitive hardware is synchronized with a Rubidium clock[25] at 10MHz. Meanwhile, *Cicero* writes a protocol file including all sequence information of the current run and sends commands to a camera PC that runs our camera software *QCam*[26]. *QCam* prepares the cameras for taking images and stores them. The images and protocol files are then processed by a Matlab-based *Image Viewer* software developed by Justus Brüggenjürgen. The *Image Viewer* calculates the optical density (OD) and enables us to perform quick analyses of the current and past experimental runs. The interplay of all the components mentioned above is illustrated in figure 3.11. Additionally, we monitor multiple experimental quantities in real-time on a *Monitor PC* to ensure a safe remote operation. These include for example analog signals from photodiodes, the vacuum pressure gauges or the temperature sensors at the Lithium oven. These signals are either monitored with a data logger[27] or digital oscilloscopes[28]. An auxiliary infrared-sensitive camera streams a video of the glass cell to a monitor in the lab, such that we have a live view of the experiment even if the laser safety is in place. An additional analog *Interlock System* prevents damaging of the experimental apparatus caused by hard- or software failures (see [59]).

---

[22] Jäger Messtechnik: Adwin Pro II with Pro-CPU-T12
[23] Jäger Messtechnik: Pro II-AOUT-8/16, 16-bit resolution, 3×8 channels
[24] Jäger Messtechnik: Pro II-DIO-32, 3×32 channels
[25] SRS FS725 Rubidium Frequency Standard
[26] It is based on the Bachelor's thesis of Niels-Ole Rohweder [80]
[27] Pico Technology: TC-08
[28] Pico Technology: PicoScope 2000

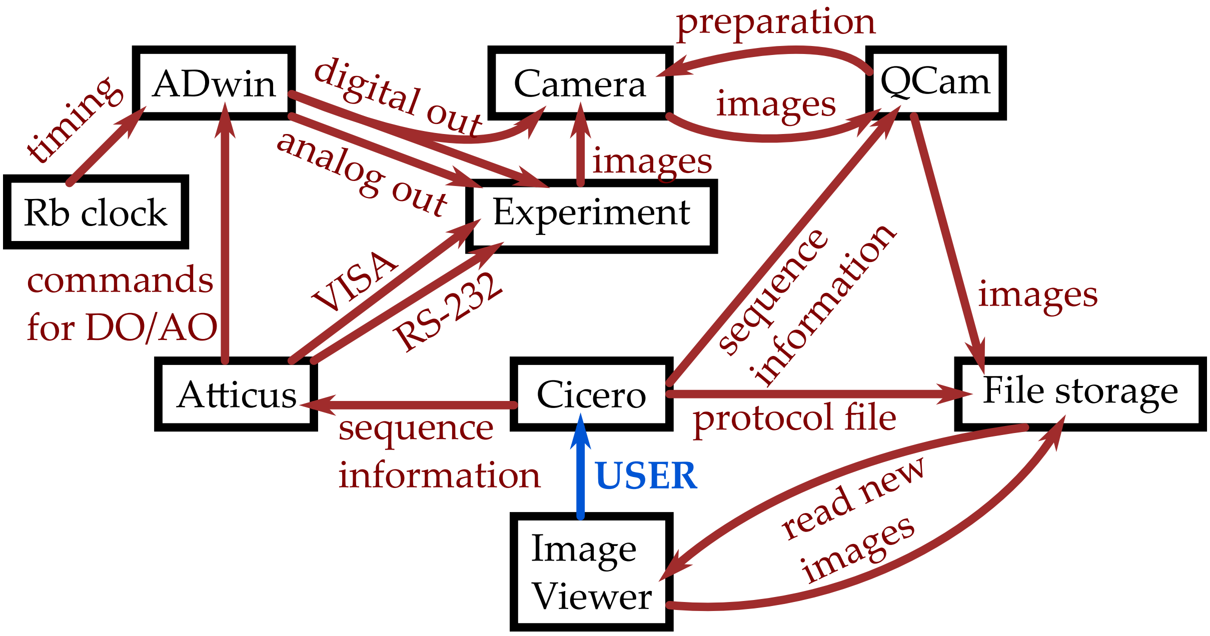

Figure 3.11: Illustration of the interplay between the soft- and hardware that controls the experiment - The user designs an experimental sequence in *Cicero*. The *Atticus* server manages the communication with all hardware devices to execute said sequence, the most important of which is the *Adwin Pro II* that provides multiple analog and digital real-time outputs. A camera software named *QCam* prepares the cameras for taking images and manages the data storing. We can use the *Image Viewer* software to display the optical density for each shot and perform real-time analyses. Figure taken from [57].

3.3 | Laser Cooling and Trapping

In modern quantum gas experiments, laser cooling is crucial as the first cooling step, since it enables cooling of neutral atoms by several orders of magnitude from oven temperatures down to the μK-regime within just a few milliseconds. In the past decades, multiple well established laser cooling techniques have been developed, which we won't cover in theoretical detail here. The following section discusses our approach to cooling ^{7}Li. We first describe our compact 2D/3D-MOT setup for the initial capture and cooling of the atoms. While the trapping of ^{7}Li had already been implemented in our setup prior to this thesis, we significantly improved the particle number and the loading rate of the MOT during this work. As of writing this thesis, we are able to capture ca. 6×10^8 atoms at ca. $3300\,\mu\mathrm{K}$ within $5\,\mathrm{s}$ of MOT loading. The MOT-stage is followed by a so-called compressed MOT (cMOT)), in which we further cool the atoms to ca. $800\,\mu\mathrm{K}$ while simultaneously increasing the atomic density - causing the overall PSD to increase. Since the hyperfine structure of the $2^2P_{3/2}$-state of both Lithium isotopes is only poorly resolved within the natural linewidth of the D2 transition, standard optical molasses cooling is not feasible to reach sub-Doppler temperatures[29]. In 2013, it was shown, that Gray Molasses cooling can be applied to Lithium atoms to achieve sub-Doppler temperatures [35], which has since become a standard technique for Lithium experiments.

---

[29] The Doppler temperature for ^{7}Li is $T_\mathrm{D} = 141\,\mu\mathrm{K}$

Hence, we follow the cMOT phase with a Gray Molasses phase to further cool the atoms down to ca. $35\,\mu$K. The experimental key parameters for the mentioned laser cooling steps are listed in table 3.4. Figure 3.12 depicts the energy levels of ^{7}Li and the relative detunings of the applied laser beams.

Table 3.4: Experimental key parameters for laser cooling - The intensities are given in units of the saturation intensity $I_{\mathrm{sat}} = 2.54\,\mathrm{mW/cm^2}$ and the detunings are given in units of the natural linewidth $\Gamma = 2\pi \times 5.87\,\mathrm{MHz}$. In AH configuration, the axial field gradient is twice as large as the radial field gradient. Here we only give the axial gradient.

	2D-MOT	3D-MOT	cMOT	GM
Beam waist (cm)	0.3	0.5	0.5	0.5
Intensity cooler I_{c} (I_{sat})	211.8	21.8	0.41	28.4
Intensity repumper I_{r} (I_{sat})	82.1	10.1	0.19	6.8
Ratio cooler : repumper $I_{\mathrm{c}}/I_{\mathrm{r}}$	2.58	2.16	2.16	4.17
Detuning cooler Δ_{c} (Γ)	-12.43	-6.64	-5.62	6.81
Detuning repumper Δ_{r} (Γ)	-5.86	-8.16	-7.14	6.81
Field gradient (G/cm)	56	25	100	-
Duration (s)	5	5	40×10^{-3}	5×10^{-3}
Temperature (μK)	-	~ 3300	~ 800	~ 35
PSD	-	$\sim 1 \times 10^{-8}$	$\sim 4 \times 10^{-7}$	$\sim 3 \times 10^{-5}$

3.3.1 Near-Resonant Laser Systems for Cooling and Imaging

The near-resonant laser system is used to drive the transitions of the 2D-MOT, the 3D-MOT, the cMOT, the push beam and resonant imaging from the $F = 2$-manifold on the D2-line, as well as the transitions for the Gray Molasses and optical dark-state pumping on the D1-line. Additionally, an offset-locked laser can be used to address transitions for imaging or repumping at detunings of up to ± 2.2 GHz from the D2-line. To provide laser light at both these D-lines, we pre-amplify two separate external cavity diode laser (ECDL) master lasers[30] and couple both into optical polarization-maintaining (PM) single mode fibers[31]. Starting the laser system with fiber couplings is advantageous, because it clears the transversal beam mode and also enables easy replacing of the master lasers without the need to adjust the whole laser system in case of maintenance work. Both master lasers are locked to the cross-over of the respective D-line via saturated absorption spectroscopy. The beam path for the spectroscopy is sketched in figure 3.13. The setup design is identical for both light sources. Two acousto-optic modulator (AOM)s shift the frequency and the beams are then split via a polarising beam splitter (PBS) into a high-intensity 'pump' beam and a low-intensity 'probe' beam, one of which passes through an electro-optic modulator (EOM) that modulates frequency sidebands onto the beam. Both spectroscopy setups feature two photodiodes such that we can choose between frequency modulation spectroscopy (FMS) or modulation transfer spectroscopy (MTS). We currently operate the D2-lock with MTS and the D1-lock with FMS. Further details regarding the lock can be found in [72].

---

[30] Toptica: TA pro for the D2-line and DL pro + BoosTA for the D1-line

[31] Thorlabs: P3-630PM-FC-1

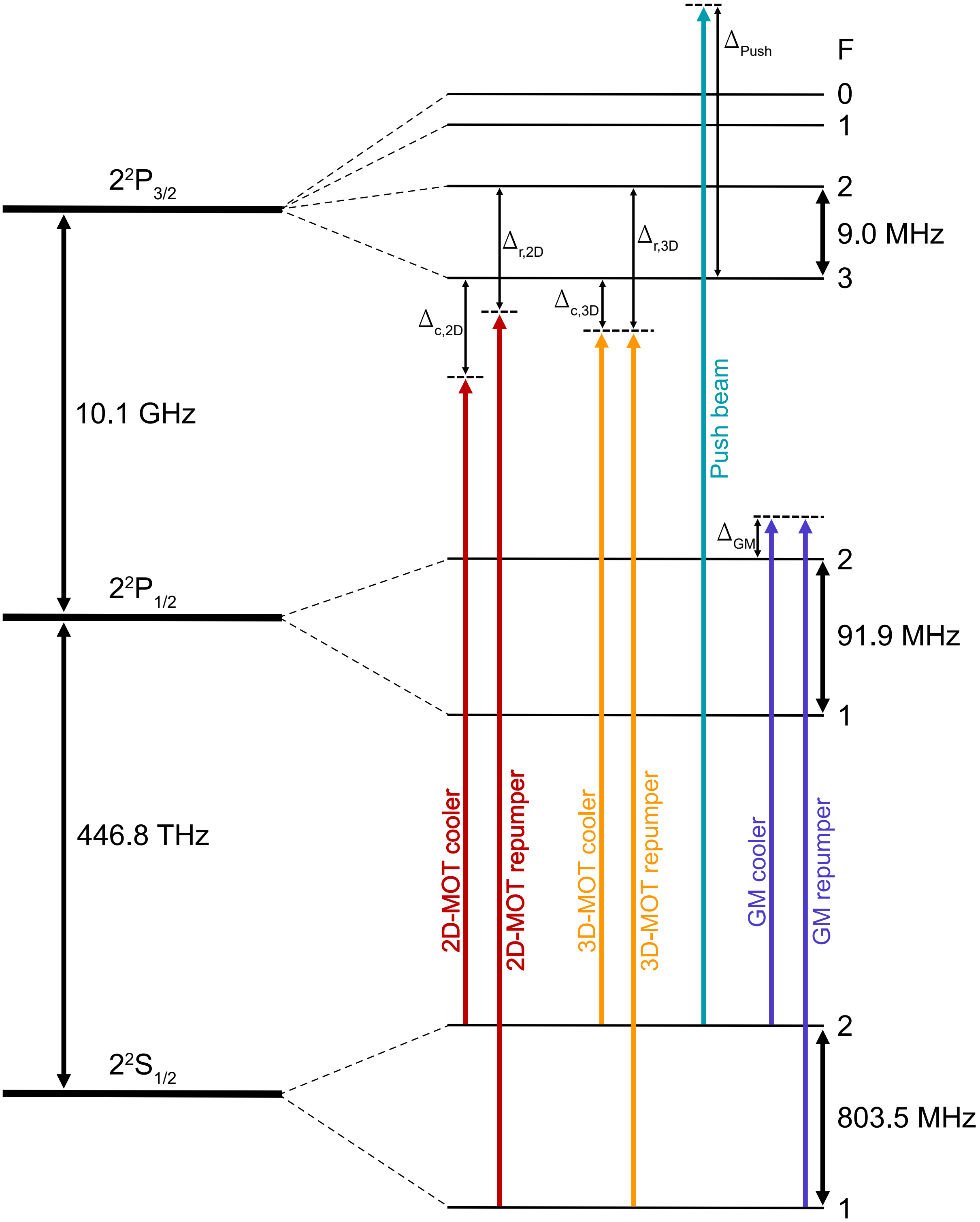

Δ_{Push}
F
0
1
2
3
9.0 MHz
$2^2P_{3/2}$
$\Delta_{r,2D}$
$\Delta_{r,3D}$
$\Delta_{c,2D}$
$\Delta_{c,3D}$
10.1 GHz
Push beam
Δ_{GM}
$2^2P_{1/2}$
2
91.9 MHz
1
446.8 THz
2D-MOT cooler
2D-MOT repumper
3D-MOT cooler
3D-MOT repumper
GM cooler
GM repumper
$2^2S_{1/2}$
2
803.5 MHz
1

Figure 3.12: Energy levels of ^{7}Li and the relative detunings of the applied laser beams - To establish cycle transitions, we need to address both hyperfine states of the ground state for each cooling process. Due to the poorly resolved hyperfine state on the D2-line and the comparably high branching ratio of the energy levels involved, both frequencies contribute almost equally to the cooling processes. Nonetheless, we stick to the established notation of labelling the transition from the $F = 2$-manifold 'cooler' and the transition from the $F = 1$-manifold 'repumper'. The values of the detunings can be found in table 3.4, except for the push beam which is $\Delta_{\mathrm{push}} = 5.28\,\Gamma$. The spectroscopic data are taken from [26].

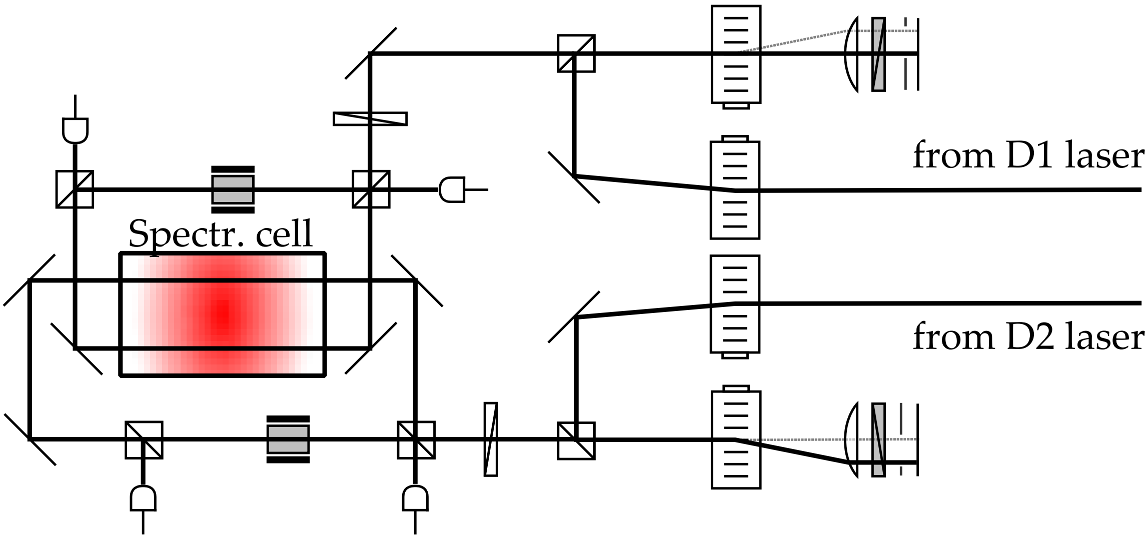

Figure 3.13: Sketch of the spectroscopy setup - We lock both master lasers via saturated absorption spectroscopy on a spectroscopy cell that is heated to ca. $660\,\mathrm{K}$. We can perform either FMS or MTS. The displayed beam path shows the setup for locking onto the D-lines of ^{7}Li. One can switch the lock to the other isotope by inverting the logic of the two double-pass AOMs. A legend explaining the symbols for the optical components can be found in figure 3.14. Figure adapted from [57].

The main part of the laser system was conceptualized and constructed prior to this thesis. The motivation and design concepts are described in detail in the Master's and PhD theses of Andreas Kerkmann [72, 57]. However, while working with ^{7}Li we found it necessary to increase the optical power on the atoms to improve the MOT performance and thus revised ca. $50\,\%$ of the laser system. The current setup is depicted in figure 3.14. The laser system can be divided into three parts. One for the supply of the 2D-MOT, a second part for the supply of the 3D-MOT as well as Gray Molasses and a third part for the imaging. The purpose of this laser system is to couple the correct light frequency and intensity for each experimental time-step into one of nine PM fibers[32] that guide the light to the experiment. There are two optical fibers for the two arms of the 2D-MOT, one fiber for the push beam and four fibers for the 3D-MOT. The 2D-MOT beams as well as the 3D-MOT beams in the $x-y$ plane are retro-reflected, while we use two separate fibers to address the two z-directions (see figure 3.17). The imaging light can be coupled into the MOT x- and MOT y-fiber on the respective orthogonal polarization axes. Two additional fibers are used for imaging along the axis of the optical plug (see section 3.4.3) and along the z-axis. The latter of which is also used to apply light for the optical dark state pumping (see section 3.4.1). We use several different optical elements in the laser system:

- Polarizing beam splitters, $\lambda/2$-waveplates and mirrors are used to split or overlap the beams and to adjust the beam path as well as the polarization.

- Lenses are used to adjust the beam shape (not depicted in figure 3.14).

- AOMs are used to precisely tune the frequency of the light (when used in double-pass configuration) and to quickly switch the light and set the intensity on the atoms (when used in single-pass configuration).

---

[32] Thorlabs: P3-630PM-FC-10

- For both the 2D-MOT as well as the 3D-MOT and Gray Molasses beam path, we use phase-modulating EOMs to generate the light for the repumper by imprinting frequency sidebands on to the laser beams. Both EOMs are operated in the vicinity of the hyperfine splitting frequency of $803.5\,$MHz. The blue sidebands are used as repumpers while the red sidebands are off-resonant and don't interact with the atoms. The creation of those sidebands is monitored on a Fabry-Perot interferometer (FPI). In the 2D-MOT beam path, we additionally installed a second EOM that operates at $12.5\,$MHz. It is used to effectively broaden the linewidth of the 2D-MOT beams and address a larger variety of velocity classes in the 2D-MOT (see section 3.3.2).

- We use tapered amplifier (TA)s to generate the required optical power.

- Shutters are used to mechanically block beam paths when they are not used to avoid stray light on the atoms.

- A non-polarizing 50:50 splitter in combination with double-pass AOMs allows us to switch the seed of the 3DTA between D2- and D1-light when switching between the MOT and the Gray Molasses.

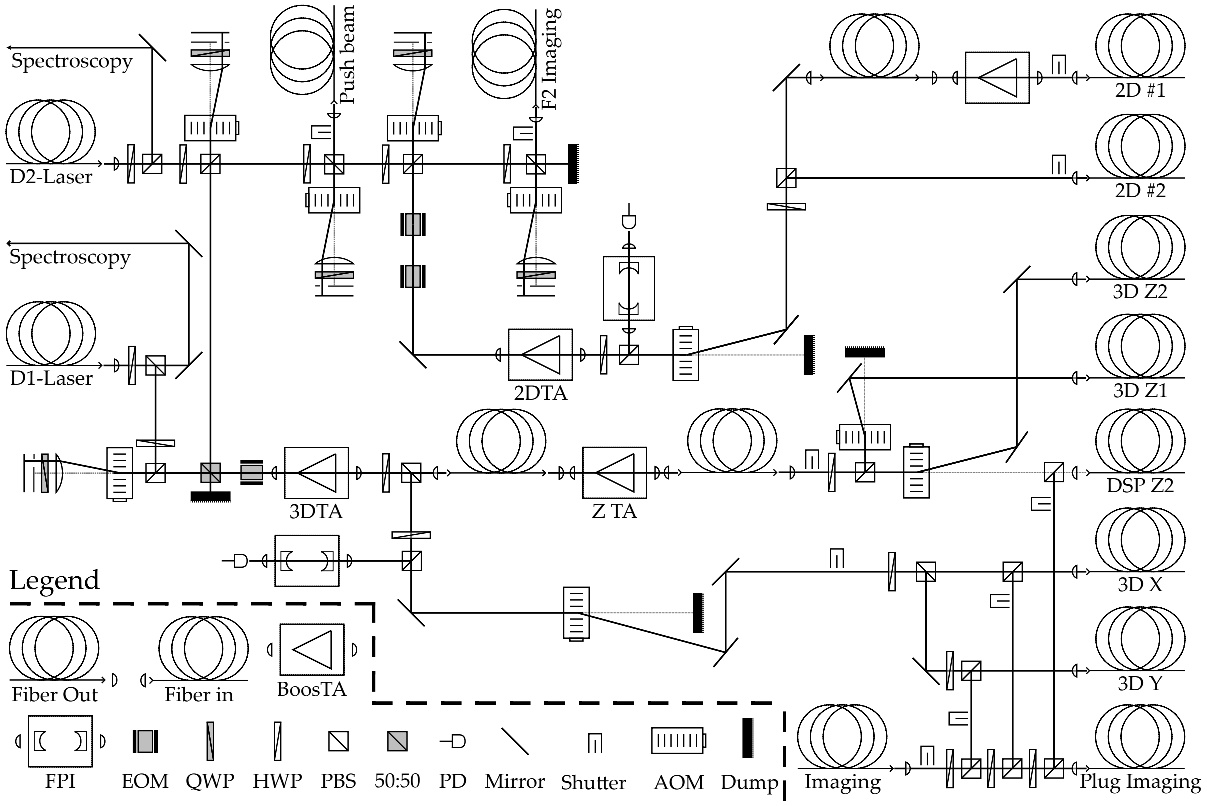
Spectroscopy
D2-Laser
Push beam
F2 Imaging
2D #1
2D #2
Spectroscopy
D1-Laser
2DTA
3D Z2
3D Z1
3DTA
Z TA
DSP Z2
3D X
3D Y
Legend
Fiber Out
Fiber in
BoosTA
FPI
EOM
QWP
HWP
PBS
50:50
PD
Mirror
Shutter
AOM
Dump
Imaging
Plug Imaging

Figure 3.14: Near-resonant laser system - The light of the two master lasers is amplified via multiple tapered amplifiers and coupled into nine polarization-maintaining optical fibers that guide the light to the experiment. Via polarizing beam splitters in front of the optical fibers, we can couple imaging light on the orthogonal polarization axes. Not shown: AOMs and mechanical shutters allow us to either use the F2 imaging light or the light from an offset-locked laser for imaging. As a library for optical components the author used [57, 81].

For imaging or repumping transitions at non-zero magnetic fields, we use an additional ECDL laser at $671\,$nm[33]. It is offset-locked to the D2 master laser. For the offset lock, a part of the light from the DL pro is overlapped with light from the D2 master laser on a non-polarizing 50:50 splitter. A photodiode[34] detects the beat of the two light signals, which is then processed on a custom made printed circuit board (PCB). Here, the signal gets amplified and divided before it is compared to a reference signal on a digital phase-locked loop (dPLL). The reference signal is generated by a signal generator[35] that can be programmed via the experimental control. The output of the dPLL is a TTL signal that is either high or low depending on which one of the two compared frequencies is higher. We feed this output as an error signal into the locking electronics from Toptica. The *DigiLock* software allows us to lock at either the positive or the negative slope such that we can use either a blue- or a red-detuned frequency offset. With this setup we can tune the offset lock in a range between ± 50 MHz and ± 2.2 GHz from the D2-line. More details can be found in [57]. A sketch of the offset lock scheme is depicted in figure 3.15. The part of the light that is not used for the lock is coupled into a fiber towards distribution on the imaging axes.

---

[33] Toptica: DL pro

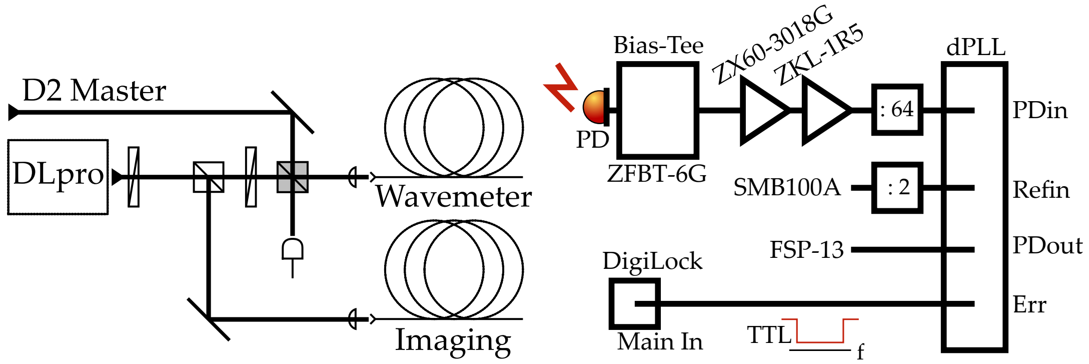

(a) (b)

Figure 3.15: The offset lock - **(a)** Sketch of the optical beam path for the offset lock. Part of the light from the DL pro is overlapped with the D2 Master laser on a non-polarizing 50:50 splitter. A photodiode measures the beat of both light signals. The other part of the light from the DL pro is coupled into a fiber to further distribute the light onto the imaging axes. An additional fiber port allows us to check the wavelength of both the master and offset-locked laser on a wavelength meter. A legend explaining the symbols for the optical components can be found in figure 3.14. As a library for optical components the author used [57, 81]. **(b)** Sketch of the electronic components used in the offset lock. The photodiode signal (PDin) is processed on a custom PCB and compared to a reference signal (Refin) via a dPLL board that generates the error signal for the lock. Figure taken from [57].

3.3.2 2D/3D-MOT

For the initial trapping and cooling of the atoms, we use a 2D/3D-MOT setup similar to [76]. The atomic source is the oven, which is placed perpendicular to the line of sight between the 2D-MOT and the 3D-MOT chamber. It is heated to 690 K such that a flux of Lithium atoms is released into the chamber. We transversally cool the hot Lithium atoms in a 2D-MOT. Eight stacks of permanent magnets are mounted to the vacuum chamber and generate a magnetic field gradient of 56 G/cm [57]. The 2D offset coils allow for a precise positioning of the magnetic field center. The light for the 2D-MOT is shone onto the atoms from two perpendicular axes which we label 2D $\#1$ and 2D $\#2$. Both beams have a $1/e^2$-beam waist radius of 3 mm and are circular polarized. After the first pass of each beam, they are retro-reflected and used again for the counter-propagating 2D-MOT beam. A CAD drawing of the 2D-MOT setup and a photograph of the 2D-MOT fluorescence are shown in figure 3.16.

---

[34] Hamamatsu Photonics: G4176-03

[35] Rohde & Schwarz: SMB100A

We transfer the atoms from the 2D-MOT to the 3D-MOT via a push beam that scatters the atoms through the differential pumping tube. The push beam is collimated to a beam waist radius of $725\,\mu\text{m}$. It is blue detuned with $\Delta_{\text{push}} = 5.28\,\Gamma$ at an intensity of $I_{\text{push}} = 1.93\,I_{\text{sat}}$. Here, $I_{\text{sat}} = 2.54\,\text{mW/cm}^2$ is the saturation intensity and $\Gamma = 2\pi \times 5.87\,\text{MHz}$ is the natural linewidth of the D2 transition.

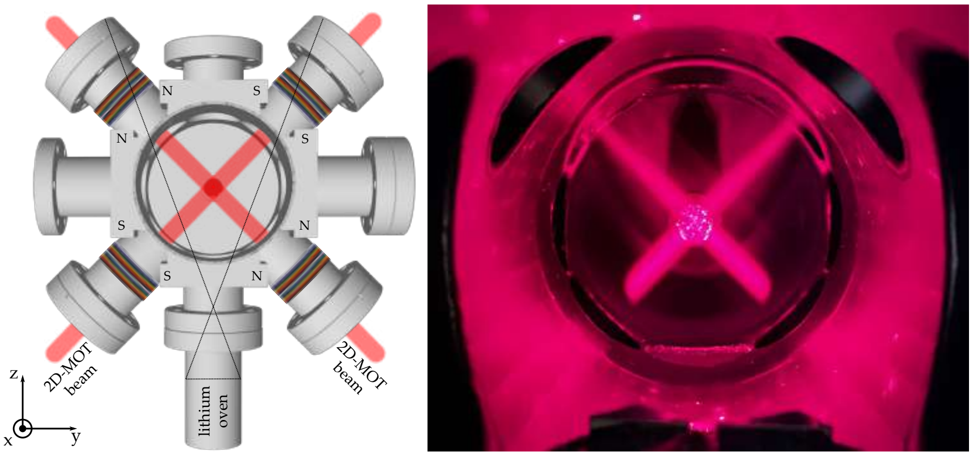

(a) (b)

Figure 3.16: View on the 2D-MOT through the rear window - **(a)** CAD drawing of 2D-MOT steel chamber. The path of the 2D-MOT beams is indicated as red laser beams. The ribbon cable 2D offset coils allow us to shift the center of the magnetic field gradient that is generated by the permanent magnets. Adapted from [58]. **(b)** Photograph of the 2D-MOT fluorescence through the rear window of the vacuum apparatus. The fluorescence appears to be brighter on the lower half of the vacuum chamber because this area is closer to the oven and it thus exposed to a higher flux of Lithium atoms.

In the glass cell, the atoms are captured in a 3D-MOT. A magnetic field gradient of $25\,\text{G/cm}$ is generated by the MOT coils (see section 3.2.2). We use a retro-reflected beam setup in the $x-y$ plane similar to the 2D-MOT beam setup. The layout of the laser system allows us to apply imaging light through the MOT fibers, but on the orthogonal polarization axes. We set up absorption imaging systems along both in-plane MOT axes with a magnification $M_{x,y}$ of $M_x = 0.82$ and $M_y = 0.42$. We use two independent fibers along the z-direction of the MOT, which we label $z1$ and $z2$. All the 3D-MOT beams have a beam waist radius of $5\,\text{mm}$ and are circular polarized. Additionally, we apply a second beam from the top with a beam waist radius of $2.5\,\text{mm}$. It is orthogonally polarized to the $z2$-MOT beam from the top and can be used for optical dark state pumping and imaging with a magnification of $M_z = 2.14$. An illustration of the MOT setup is depicted in figure 3.17.

We shine in two frequencies on the D2-line to address the transitions from both hyperfine ground states. In contrast to other alkali elements such as Rubidium, both transitions contribute almost equally to the MOT. However, we stick to the established notation of labelling the transition from the $F = 2$-manifold 'cooler' and the transition from the $F = 1$-manifold 'repumper'. The repumper is generated as a blue frequency sideband via an EOM[36]. We find the optimum intensities per beam to be $I_{\text{c,3D}} = 21.8\,I_{\text{sat}}$ and $I_{\text{r,3D}} = 10.1\,I_{\text{sat}}$. Consequently, the optimum ratio between cooler and repumper in our MOT is $I_{\text{c}}/I_{\text{r}} = 2.16$. Both the cooler and the repumper are red detuned to their relative transition with $\Delta_{\text{c,3D}} = -6.64\,\Gamma$ and $\Delta_{\text{r,3D}} = -8.16\,\Gamma$.

---

[36] The red sideband is off-resonant and doesn't influence the MOT.

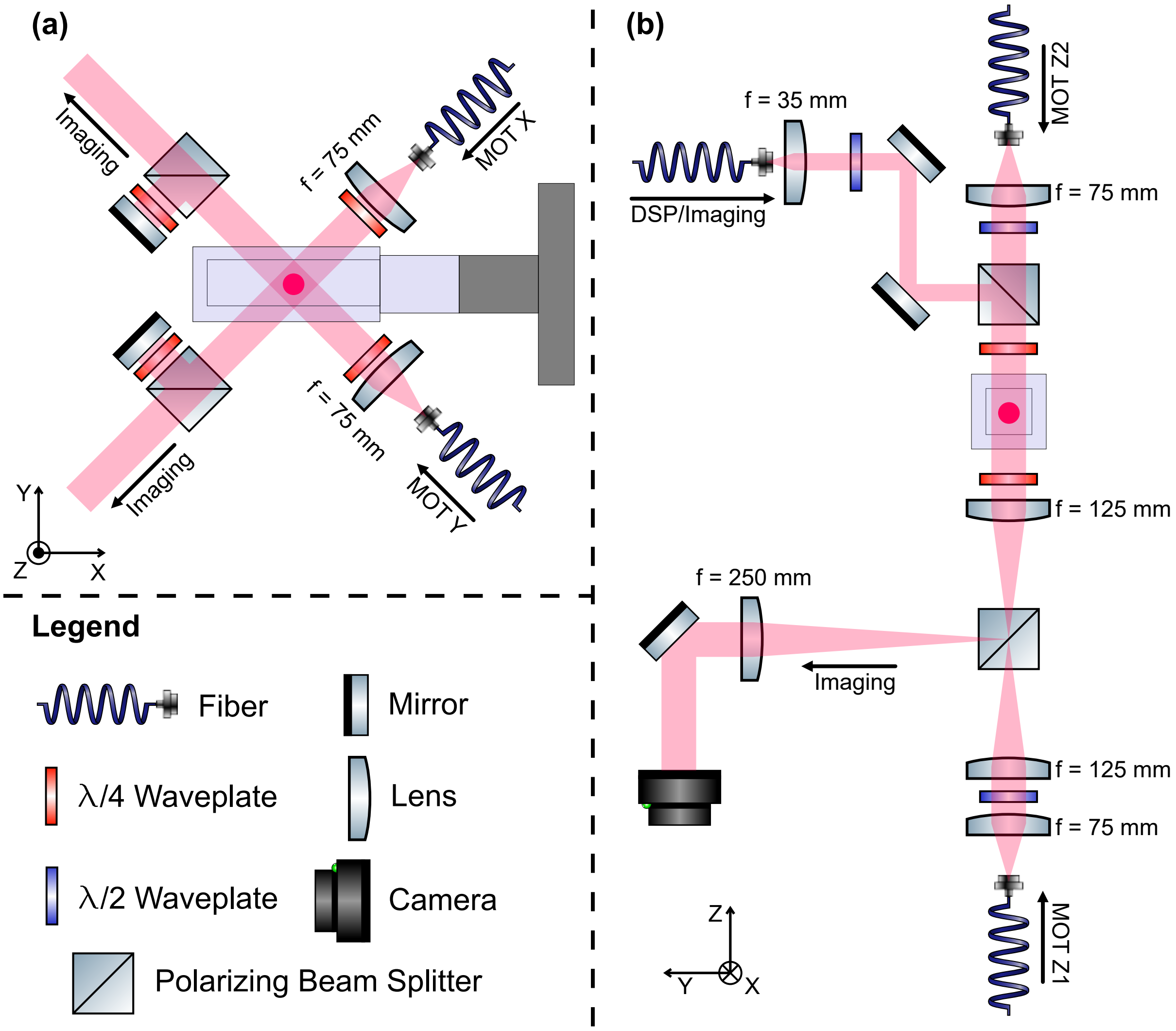
(a)
Imaging
f = 75 mm
MOT X
f = 75 mm
Imaging
MOT Y
Y
Z
X
Legend
Fiber
Mirror
λ/4 Waveplate
Lens
λ/2 Waveplate
Camera
Polarizing Beam Splitter
(b)
f = 35 mm
DSP/Imaging
MOT Z2
f = 75 mm
f = 125 mm
f = 250 mm
Imaging
f = 125 mm
f = 75 mm
MOT Z1
Z
Y
X

Figure 3.17: Illustration of the 3D-MOT setup - **(a)** Top view on the glass cell. The two MOT beams in the $x-y$-plane are coupled through polarization maintaining fibers and collimated to a size of $w_0 = 5$ mm. The circular polarization is adjusted via a $\lambda/4$-waveplate. The beams pass the glass cell and are then retro-reflected by a combination of a polarizing beam splitter, a $\lambda/4$-waveplate and a mirror. Both fibers feature an axial translation stage (not depicted) to precisely balance the beam intensity of the first and second pass. We can use the orthogonal axes of the PM fibers to shine in light for imaging. **(b)** Side view on the glass cell and the MOT beams in z-direction. We shine in an additional beam ($w_0 = 2.5$ mm) for imaging/dark state pumping (DSP) and overlap it with the MOT beams via polarizing beam splitters.

When we first started working on ^{7}Li, we were able to load ca. 1×10^8 atoms within 8 s of MOT loading, which was not sufficient as a starting point for a successful evaporative cooling in the magnetic trap[37]. During this thesis we found three ways to improve the MOT loading.

1. We increased the optical power for the 2D- and 3D-MOT by improving the laser system.
2. We implemented the 2D offset coils to precisely align the position of the 2D-MOT in front of the differential pumping tube.
3. We implemented a multi-frequency 2D-MOT scheme that allows us to address multiple velocity classes simultaneously.

---

[37] After optimizing the experimental apparatus, we can only reach quantum degeneracy when we start with at least 2×10^8 atoms in the magnetic trap.

The increase of optical power was realized by exchanging degraded TA chips and by making some changes to the laser system, the results of which are discussed in the previous section 3.3.1.

The 2D-MOT positioning in front of the pumping tube can in principle be performed by adjusting the permanent magnets that are mounted via long slots and allow for a few millimeters of movement. However, those magnets are difficult to reach and an iterative adjustment is necessary for optimization of the 2D-MOT position. Additionally, when the machine is running, the vacuum chamber is heated up by the oven to ca. $70\,^\circ\mathrm{C}$ so one has to avoid burns during the adjustment procedure. To circumvent these obstacles, we designed the 2D offset coils as described in section 3.2.2. The differential pumping tube has a diameter of $2\,\mathrm{mm}$. We numerically simulate the coils and find that we can expect an offset field of ca. $1.7\,\mathrm{G/A}$ at the origin of a single coil pair. Considering the magnetic field gradient of $56\,\mathrm{G/cm}$ this corresponds to a translation of the magnetic field center of ca. $300\,\mu\mathrm{m/A}$.

We find the optimum settings for the offset fields by scanning the current through both coil pairs independently while measuring the atom number in the MOT after $10\,\mathrm{s}$ loading without the push beam. The results of this measurement are shown in figure 3.18. We find the optimum currents to be ca. $1.033\,\mathrm{A}$ (2D $\#1$) and $0.05\,\mathrm{A}$ (2D $\#2$). This corresponds to a translation of the magnetic field center by ca. $310\,\mu\mathrm{m}$ and results in an atom number increase of ca. $20\,\%$.

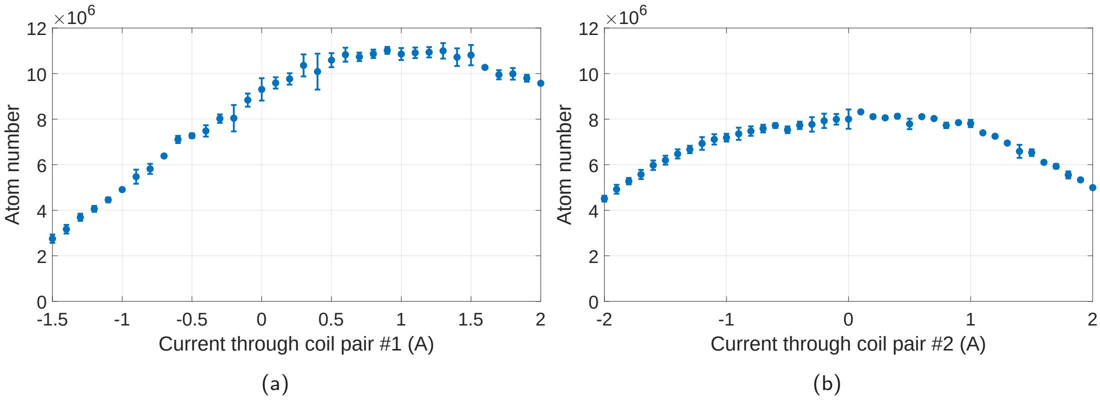

(a) (b)

Figure 3.18: Alignment of the 2D-MOT in front of the differential pumping - We plot the atom number in the MOT after loading it for $10\,\mathrm{s}$ without the push beam for different current values in the coil pair along the 2D $\#1$ **(a)** and 2D $\#2$ **(b)** axis. The sign of the current denotes the polarity of the coil pair.

The widths of both measured curves roughly match the diameter of the pumping tube. We then manually adjust the push beam onto the 2D-MOT via a beam walk and repeat the measurement with the push beam turned on at $2\,\mathrm{s}$ of MOT loading. This time we find slightly different optimal parameters of $1.1\,\mathrm{A}$ (2D $\#1$) and $0.2\,\mathrm{A}$ (2D $\#2$) corresponding to a shift of ca. $330\,\mu\mathrm{m}$. The respective measurements are displayed in figure 3.19. We can see that the width of the curve has decreased to roughly the size of the push beam. This means that we now use the offset coils to align the 2D-MOT position with the push beam. Here the offset coils allow for a much more precise adjustment than the manual beam walk.

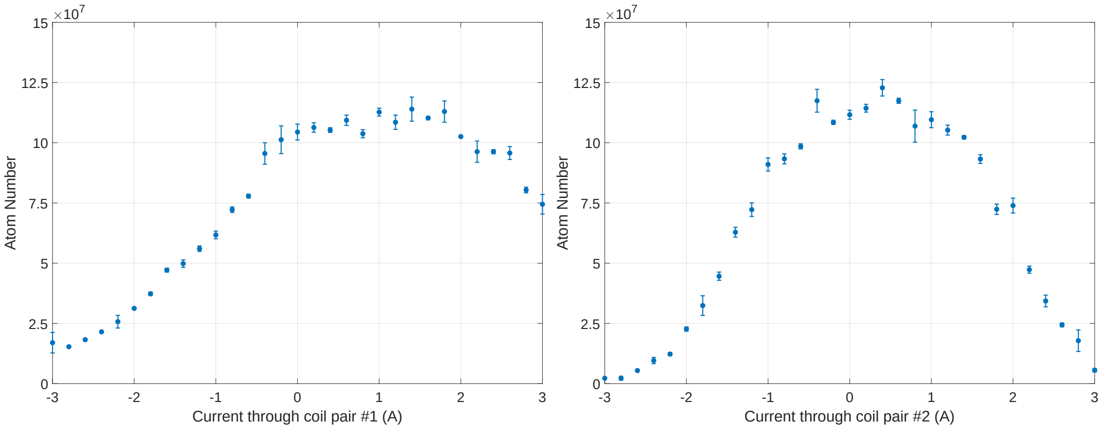

(a)

(b)

Figure 3.19: Alignment of the 2D-MOT with respect to the push beam - We plot the atom number in the MOT after loading it for $2\,\mathrm{s}$ with the push beam for different current values in the coil pair along the 2D $\#1$ **(a)** and 2D $\#2$ **(b)** axis. The sign of the current denotes the polarity of the coil pair. In contrast to figure 3.18 the width of the curves is much smaller, corresponding to the size of the push beam.

To further enhance the initial loading rate, we implemented a multi-frequency 2D-MOT approach that was originally inspired by artificially broadened narrow-line MOTs in earth-alkali like elements. Similar 2D-MOT schemes have been realized for ^{6}Li and ^{40}K atoms [82, 83]. At an oven temperature of $690\,\mathrm{K}$, the most probable atomic velocity is ca. $1280\,\mathrm{m/s}$. For typical 2D-MOT parameters the capture velocity is on the order of ca. $50\,\mathrm{m/s}$-$100\,\mathrm{m/s}$. So we only capture atoms from the low-velocity region of the Maxwell-Boltzmann distribution. Any increase of the capture velocity will hence result in a substantial gain in the loading rate. An atom can be captured when it can be decelerated to zero velocity within the volume of the 2D-MOT. Therefore, the capture velocity not only depends on the volume but also on the magnetic field gradient and the detuning of the beams such that the atoms can resonantly scatter photons within the 2D-MOT region. It is thus desirable to address as many velocity classes as possible in the 2D-MOT.

To realize this experimentally we don't only use two frequencies for the cooler and the repumper as in the typical 2D-MOT, but we modulate sidebands onto both frequencies. This results in an effective broadening of the laser frequencies such that we can address a wider range of velocity classes. We place an EOM[38] in the laser system before the repumper is modulated onto the light (see section3.3.1). We choose the frequency distance of the sidebands to be $2\pi \times 12.5\,\mathrm{MHz}$, ca. twice the natural linewidth of $\Gamma = 2\pi \times 5.87\,\mathrm{MHz}$. With this choice we ensure that we cover a wide frequency range when using the higher order sidebands, while maintaining an overlap between the single frequency components within the range of the natural linewidth. The radio frequency for the EOM is generated by an arbitrary waveform generator (AWG)[39] and is amplified with an RF amplifier[40]. With this setup we can realize modulation indices η of up to $\eta = 5$. Since the atoms are constantly removed from the 2D-MOT by the push beam, we can optimize the parameters to maximize the capture efficiency and are not limited by density effects. We find the optimum 2D-MOT performance at a modulation index of $\eta = 4.2$ and detunings of the central frequencies of $\Delta_{\mathrm{c,2D}} = -12.43\,\Gamma$ and $\Delta_{\mathrm{r,2D}} = -5.86\,\Gamma$. Integrated over the whole frequency range, the intensities per beam for the cooler and repumper are $I_{\mathrm{c,2D}} = 211.8\, I_{\mathrm{sat}}$ and $I_{\mathrm{r,2D}} = 82.1\, I_{\mathrm{sat}}$. The resulting spectrum of the cooler is illustrated in figure 3.20.

---

[38] QUBIG: EO-12.5M3-NIR

[39] RSPro: RSDG2122X

[40] Mini-Circuits: ZHL-32A+

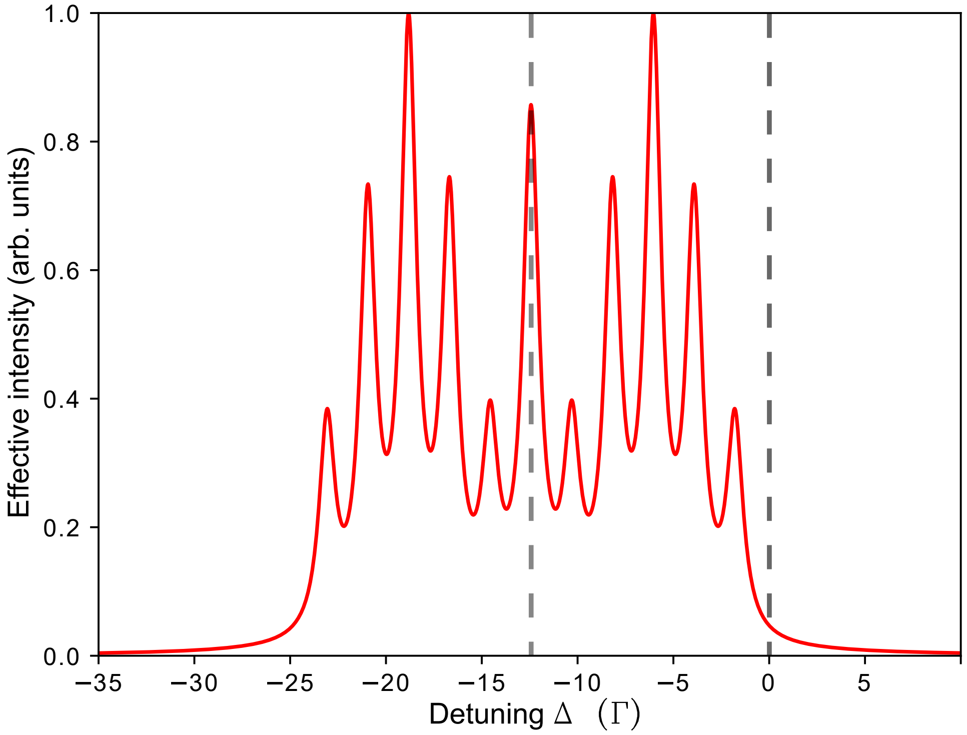

Figure 3.20: Illustration of the multi-frequency 2D-MOT approach - We plot equidistant Lorentzian distributions with the natural linewidth $\Gamma = 2\pi \times 5.87\,\mathrm{MHz}$ that are separated by multiples of $2\pi \times 12.5\,\mathrm{MHz}$. The amplitude of the Lorentzians corresponds to the absolute value of the Bessel functions of the respective order at a modulation index of $\eta = 4.2$. The two dashed lines indicate the positions of the carrier frequency and the atomic resonance.

We compare the MOT loading of the multi-frequency 2D-MOT with the simple 2D-MOT using only two frequencies. For the latter case, the optimum detunings are $\Delta_{\mathrm{c,2D,single}} = -8.52\,\Gamma$ and $\Delta_{\mathrm{r,2D,single}} = -1.94\,\Gamma$. We keep the intensities of the cooler and repumper at the same values as before. Figure 3.21 shows the the atom number after Gray Molasses cooling for both 2D-MOT schemes at different durations of 3D-MOT loading.

With the multi-frequency 2D-MOT, we achieve an initial loading rate of ca. 1×10^8 atoms/s which is a ca. ~ 3 times enhancement to the case with only one cooler and one repumper. The multi-frequency 2D-MOT saturates after ca. $20\,\mathrm{s}$ at ca. 8.5×10^8 atoms, while the single frequency 2D-MOT only reaches ca. 7×10^8 atoms within ca. $40\,\mathrm{s}$. We note that the MOT parameters presented here are optimized for fast production of BECs. We also observed up to 1.3×10^9 atoms in the MOT for long loading times at different beam parameters. We typically stop the MOT loading after $5\,\mathrm{s}$ with ca. 6×10^8 atoms at a temperature of $2660(100)\,\mu\mathrm{K}$. The phase-space density after the MOT is ca. $\sim 1.3 \times 10^{-8}$. We have also implemented this multi-frequency approach in the 3D-MOT similar to [84] where this technique improved the loading of a 3D-MOT directly from an atomic beam. However, we observed no substantial gain in atom number or loading rate. We attribute this to the fact that the atoms that are transferred from the 2D-MOT to the 3D-MOT already have a much narrower velocity distribution (compare [76]) than the atoms that are released from the oven. It is thus not necessary to cool additional velocity classes. We therefore don't use this technique in the 3D-MOT at the moment.

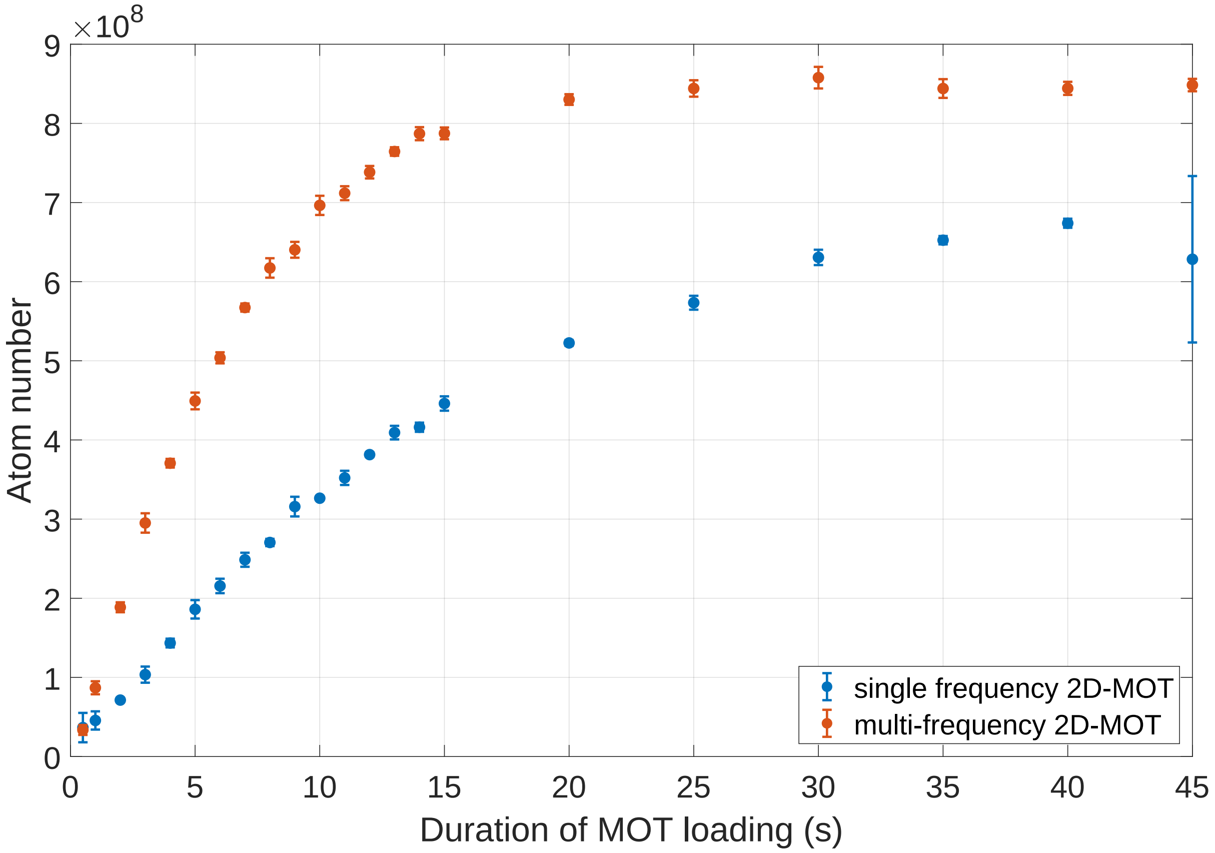

Figure 3.21: Comparison of the multi-frequency 2D-MOT with the simple 2D-MOT scheme - For both cases of the simple 2D-MOT (blue) and the multi-frequency 2D-MOT (orange) we load the MOT for different durations varying between 0.5 s to 45 s. We then perform a cMOT-stage and Gray Molasses cooling to bring all atoms to the $F = 1$-manifold before we determine the atom number via absorption imaging. We note that the GM efficiency is only ca. $80\,\%$.

3.3.3 Compressed MOT

We follow the MOT loading with a so-called compressed MOT (cMOT). By reducing the intensity and the detuning of the light, we go closer to the theoretical temperature minimum at a detuning of $-\Gamma/2$ and zero intensity. By increasing the magnetic field gradient, we can simultaneously increase the density of the atomic cloud and thus the overall phase-space density. We initially tried to keep the magnetic field gradient constant and only changed the detuning in the 3D-MOT. This resulted in an increased phase-space density, but for large atom numbers this caused issues in the subsequent cooling steps. Since the optical density of the cloud is strongly depending on the detuning, most of the cMOT light in the $x-y$ plane was absorbed on the first pass of the beams through the glass cell when tuning the frequencies closer to the atomic resonances. This resulted in a strong beam imbalance between the first pass and the retro-reflex and induced a position shift of the cMOT of several hundred micrometers. For the mode match of the cloud during the loading into the magnetic trap, the initial position of the atoms is essential. We therefore changed our approach to only slightly changing the detuning from $\Delta_{\mathrm{c,3D}} = -6.64\,\Gamma$ ($\Delta_{\mathrm{r,3D}} = -8.16\,\Gamma$) to $\Delta_{\mathrm{c,cMOT}} = -5.62\,\Gamma$ ($\Delta_{\mathrm{r,cMOT}} = -7.14\,\Gamma$) within 40 ms. At the same time we reduce the intensity per beam from $I_{\mathrm{c,3D}} = 21.8\,I_{\mathrm{sat}}$ ($I_{\mathrm{r,3D}} = 10.1\,I_{\mathrm{sat}}$) to $I_{\mathrm{c,cMOT}} = 0.41\,I_{\mathrm{sat}}$ ($I_{\mathrm{r,cMOT}} = 0.19\,I_{\mathrm{sat}}$) while increasing the magnetic field gradient from 25 G/cm to 100 G/cm. As a consequent we get a strong compression of the cloud while avoiding light significant absorption and thus a displacement of the cloud. We end up with still ca. 6×10^8 atoms at a temperature of $801(43)$ µK and a phase-space density of ca. $\sim 3.6 \times 10^{-7}$.

3.3.4 Gray Molasses

The final laser cooling step is the Gray Molasses (GM). After the cMOT, we switch off the MOT coils and only keep the offset coils turned on to cancel any residual magnetic stray fields, that would repeal the degeneracy of the m_F-subspaces[41]. Simultaneously, the MOT light is switched off and we apply light that is blue-detuned to the D1-line through the same optical fibers on the same polarization axes. We realize this by changing the seed frequency of the first TA in the near-resonant laser system (see section 3.3.1). We again use the same EOM as for the 3D-MOT to generate frequency sidebands but with different parameters. The carrier drives a transition from the $F = 2$-manifold which we again label as cooler, while the blue sideband serves as a repumper that drives the transition from the $F = 1$-manifold. The red sideband is again off-resonant. We experimentally find the optimum value for the cooler to repumper ratio to be ca. 4.17. We then set the overall power to be the highest that the laser system can provide, resulting in intensities per beam of $I_{\mathrm{c,GM}} = 28.4\, I_{\mathrm{sat}}$ and $I_{\mathrm{r,GM}} = 6.8\, I_{\mathrm{sat}}$. While the precise value of the overall detuning of both frequencies is not too crucial for the cooling scheme, the final temperature is quite sensitive to the relative detuning. As expected, we find the optimum performance at the two-photon resonance of the Raman transition. This can be explained by the so-called Λ-enhancement, that leads to additional dark states in the system and thus lower temperatures [35]. We achieve the highest phase-space density at detunings of $\Delta_{\mathrm{c,GM}} = \Delta_{\mathrm{r,GM}} = +6.81\,\Gamma$ to the D1 transition[42]. We apply the Gray Molasses cooling for 5 ms. We end up with ca. $80\,\%$ of the atoms that we captured in the MOT at a minimum temperature of $35(2)$ µK and a phase-space density of ca. $\sim 3.3 \times 10^{-5}$.

Optionally, we can then switch off the EOM that generates the repumper. As result, the transition cycle is opened up and the atoms are pumped into the $F = 1$-manifold within 50 µs. We can then remove the remaining atoms in $F = 2$ by shining resonant light onto the atoms for ca. 70 µs. We do this to characterize the performance of the laser cooling. For standard experimental runs, we don't need these extra steps, because we follow the GM with an optical darkstate pumping on the D1-line to $F = 2, m_F = 2$, during which we populate both hyperfine manifolds anyways.

3.4 | Evaporation in the Magnetic Trap

After the Gray Molasses cooling, the phase-space density is ca. $\sim 3.3 \times 10^{-5}$. This is still several orders of magnitude below the phase transition threshold[43]. At typical atomic densities ($n \sim (10^{11} - 10^{13})$ cm^{-3}), the required temperatures are on the order of $T \sim 100$ nK, which cannot be reached for Lithium using only laser cooling techniques[44]. We thus need to employ an evaporative cooling technique by removing the hottest atoms from the cloud and letting the kinetic energy redistribute accordingly. This is an intrinsically very lossy process and we should expect to lose several orders of magnitude in the atom number on the way to reaching the quantum-degenerate regime. From an experimentalist's point of view, the following three aspects are crucial to ensure a fast and efficient evaporation.

---

[41] The precise calibration of the magnetic field compensation was performed in the magnetic trap, the position of which is highly sensitive to stray fields.

[42] The natural linewidths Γ of the D1 and the D2-line are equal.

[43] In a three-dimensional box potential, this threshold is given by $\rho = n\Lambda_T^3 \approx g_{3/2}(1) \approx 2.612$, where n is the atomic density and $\Lambda_T = \sqrt{\frac{2\pi\hbar^2}{mk_{\mathrm{B}}T}}$ is the thermal de-Broglie wavelength [85].

[44] The fundamental temperature limit for laser cooling is the temperature associated with the recoil of a single emitted photon, the so-called recoil temperature T_{R}. This limit depends on the mass m of the atom and the momentum $|\boldsymbol{k}| = 2\pi/\lambda$ of the emitted photon with wavelength λ. For ^{7}Li cooled on the D2 transition this limit is $T_{\mathrm{R}} = (\hbar\boldsymbol{k})^2/(2mk_{\mathrm{B}}) \approx 3$ µK.

1. We need an experimental tool to properly remove only the hottest atoms in a controlled manner.
2. The collision rate must be adequate to redistribute the kinetic energy on a reasonable timescale.
3. The overall particle losses must be kept negligible compared to the particle loss induced by the evaporation.

Our initial plan was to directly load an optical dipole trap from the Gray Molasses and use the Feshbach resonance of ^{7}Li to tune the interaction strength while spilling the hottest atoms from the cloud by reducing the trap depth. However this approach had two flaws. On the one hand, the volume of the dipole trap was limited such that the initial atom number was quite low. On the other hand, the atomic density in the dipole trap rapidly increased during the evaporation and as a consequence the density-dependent three-body losses became the dominating loss-mechanism, preventing a successful evaporation. As discussed in chapter 2, ^{7}Li comes with disadvantageous scattering properties for evaporative cooling. While the elastic collision rate $\Gamma_{\mathrm{el}} = n\sigma v$ that sets the timescale for rethermalization in the gas scales as $\sigma_2 \propto n$, the three-body losses scale as $\sigma_3 \propto n^2$. The large three-body loss coefficient of ^{7}Li sets a limit to experimentally suitable densities to be below $1 \times 10^{13}\,\mathrm{cm}^{-3}$ to keep the three-body losses negligible during typical evaporation timescales. So for an efficient evaporation scheme, we need to control the atomic density dynamically during the evaporation process, which is not possible in an optical dipole trap.

We can avoid both problems of the optical dipole trap by instead using a magnetic quadrupole trap to start the evaporative cooling. This trap is easily implemented by operating the main coils that are already installed in the experiment in anti-Helmholtz mode[45]. In the Zeeman regime, the energy ΔE of a neutral atom in a magnetic field $|\boldsymbol{B}(\boldsymbol{r})|$ is given by

$$\Delta E(\boldsymbol{r}) = m_F g_F \mu_{\mathrm{B}} |\boldsymbol{B}(\boldsymbol{r})|, \tag{3.1}$$

with the magnetic quantum number m_F of the respective state, the Landé-factor g_F and the Bohr magneton μ_{B}. The quadrupole field that is generated by our main coils in anti-Helmholtz configuration can be described by a single parameter b, the gradient of the field along the z-direction:

$$\boldsymbol{B}(\boldsymbol{r}) = b \begin{pmatrix} -x/2 \\ -y/2 \\ z \end{pmatrix}. \tag{3.2}$$

Consequently, the absolute value of the magnetic field is given by

$$|\boldsymbol{B}(\boldsymbol{r})| = b\sqrt{\frac{x^2 + y^2}{4} + z^2}. \tag{3.3}$$

---

[45] This setup provides a linear potential which in terms of mode-matching and achievable elastic collision rate is superior to the quadratic potential one would get with a Ioffe-Pritchard or TOP trap [86].

This leads to the Zeeman shift of the atoms in the quadrupole trap

$$\Delta E(\boldsymbol{r}) = m_F g_F \mu_{\mathrm{B}} b \sqrt{\frac{x^2+y^2}{4} + z^2}. \tag{3.4}$$

Due to the large volume of the magnetic trap, we can capture almost all of the atoms from the Gray Molasses. By applying a tunable radio frequency, we can induce a spin-flip in the atoms with the highest kinetic energy such that they are transferred from a trapped to an untrapped state and are then expelled from the trap. Additionally, we can dynamically change the potential gradient via the electric current through the coils. We thus have control over the atomic density at all times during the evaporation such that we can keep a balance between the elastic two-body collisions and the inelastic three-body losses. We discuss this in more detail in appendix A. However, when using a quadrupole trap, we need to address the issue of Majorana losses that can occur when the atoms move in the vicinity of a true magnetic field zero. We solve this issue by shining a tightly focused blue-detuned laser beam along an axis y' in the $x-y$-plane onto the magnetic field center that repels the atoms. The effective potential $U(\boldsymbol{r})$ for the atoms in the magnetic trap becomes

$$U(\boldsymbol{r}) = m_F g_F \mu_{\mathrm{B}} b \sqrt{\frac{x^2+y^2}{4} + z^2} - mgz + U_{\mathrm{plug}} e^{-2\frac{x'^2+z^2}{w_{\mathrm{plug}}^2}}, \tag{3.5}$$

with the mass m of the atoms, the acceleration of gravity g, the $1/e^2$ beam waist radius of the plug beam w_{plug} and the repulsive potential barrier height U_{plug}. Figure 3.22 shows a visualization of the evaporation in this potential landscape.

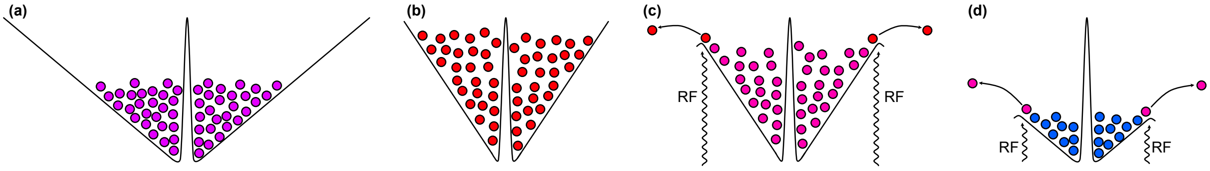

Figure 3.22: Concept of the evaporation in the magnetic trap - **(a)** After the Gray Molasses the atoms are trapped in the magnetic quadrupole trap. **(b)** The trap is adiabatically compressed to increase the density and kick-start the evaporation process. **(c)** The hottest atoms are expelled from the trap by driving an RF transition that is only resonant to the atoms with the most kinetic energy. **(d)** The trap is adiabatically decompressed to manage the density-dependent three-body losses during further evaporation. This illustration is inspired by [45].

3.4.1 Optical Dark State Pumping

At the end of the Gray Molasses, the atoms populate both hyperfine manifolds of the ground-state. For the evaporation in the magnetic trap, we need to prepare the atoms in one of the three magnetically trappable (e.g. low-field seeking) states. As can be seen in equation 3.5, the atoms can be trapped in the magnetic trap as long as $m_F \times g_F > 0$. For the three states $|F=1, m_F=-1\rangle$, $|F=2, m_F=1\rangle$ and $|F=2, m_F=2\rangle$, this results in a positive Zeeman shift and the atoms require additional energy when they move away from the center of the quadrupole field. The other states are either anti-trapped ($m_F \times g_F < 0$) or un-trapped ($m_F = 0$). The $|F=2, m_F=2\rangle$-state is preferable for several reasons. It is an extremal state and as such not prone to spin-changing collisions. It also has the largest value of the product $m_F \times g_F$ which allows for the tightest confinement of the atoms at the same magnetic fields. From equation 3.5 we can also see that the minimum magnetic field gradient has to be large enough to compensate the gravitational sag $b_g = mg/m_F g_F \mu_{\mathrm{B}}$. In the case of ^{7}Li in the $|F = 2, m_F = 2\rangle$-state this is $b_g = 1.2\,$G/cm.

We prepare the atoms in said state via so-called optical dark state pumping. Starting from both groundstate hyperfine manifolds we apply circular polarized light close to the D1 transition to drive σ^+-transitions to the $F = 2$-manifold of the $2^2P_{1/2}$-state. The atoms then decay via spontaneous emission which occurs randomly either via $\sigma^\pm$- or π-transitions. Over several cycles the spontaneous emissions carry no net angular momentum. As a result, the atoms that were initially randomly distributed in the m_F-subspaces accumulate in the $|F = 2, m_F = 2\rangle$-state. From here there is no possible further excitation via a σ^+-transition and the atoms stop scattering light. It is crucial that the light polarization is pure to prevent any further scattering that would further heat the atoms. Figure 3.23 illustrates the optical dark state pumping. To minimize the net momentum transfer during the optical pumping, we apply both light frequencies from two beams with opposing directions $z1$ and $z2$ (see figure 3.17). We apply a small bias field of ca. $1\,$G that provides a quantization axis along the z-direction using the 3D offset coils. To provide the light for the optical dark state pumping we use the laser system almost in the same way as for the Gray Molasses cooling. We shut off the $z2$-beam and the horizontal beams and instead use an additional AOM to shine in light along the DSP/Imaging path (see figure 3.14). We change the detunings to $\Delta_{F=2->2} = 8.5\,\Gamma$ $\Delta_{F=1->2} = 10.2\,\Gamma$ and set the intensities per beam to $I_{F2->2} = 12.4\,I_{\mathrm{sat}}$ and $I_{F1->2} = 8.6\,I_{\mathrm{sat}}$. We set the detunings such that the relative detuning $\delta = \Delta_{F=1->2} - \Delta_{F=2->2}$ is non-zero. With this choice we avoid two-photon Raman transitions from one hyperfine groundstate to the other that would conserve angular momentum. Figure 3.24 shows the atom number in the dark state as a function of the pumping time. To minimize the decrease of the density as the cloud expands, we typically stop the dark state pumping after $150\,$µs at a transfer efficiency close to unity. Further analysis of the atomic cloud's net momentum kick after the dark state pumping indicates that the atoms scatter on average three to four photons before they end up in the dark state. We observe no significant heating of the atoms.

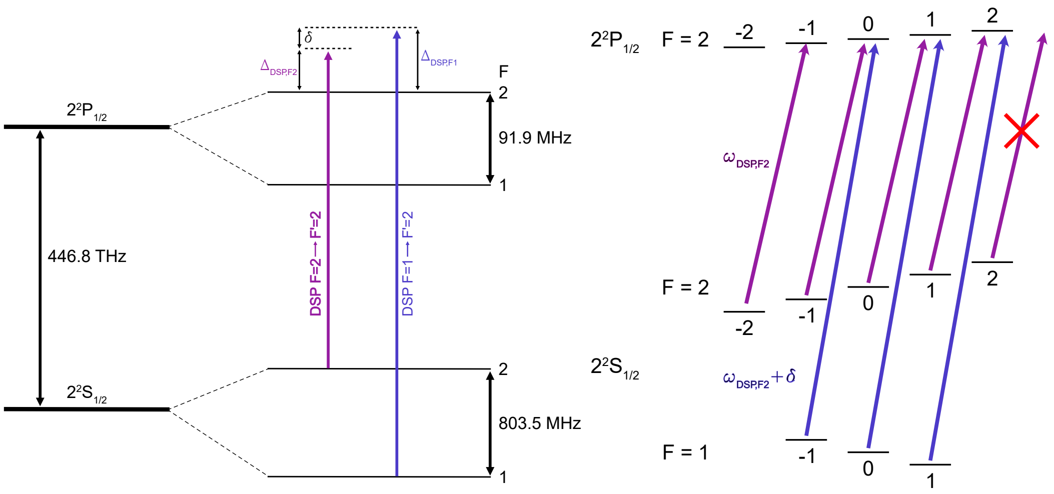

(a) (b)

Figure 3.23: Illustration of the optical dark state pumping - **(a)** We apply blue-detuned light on the D1 transition to excite the atoms from the two hyperfine manifolds of the groundstate to the $F = 2$-manifold of the $2^2P_{1/2}$-state. **(b)** Atoms that initially populate all m_F-substates are transferred to higher m_F-states via σ^+-transitions. The spontaneous decay (not shown) carries a random angular momentum with $\Delta m_F = 0, \pm 1$ and causes no net change of the m_F state. As a result the atoms accumulate in the dark state $|F = 2, m_F = 2\rangle$.

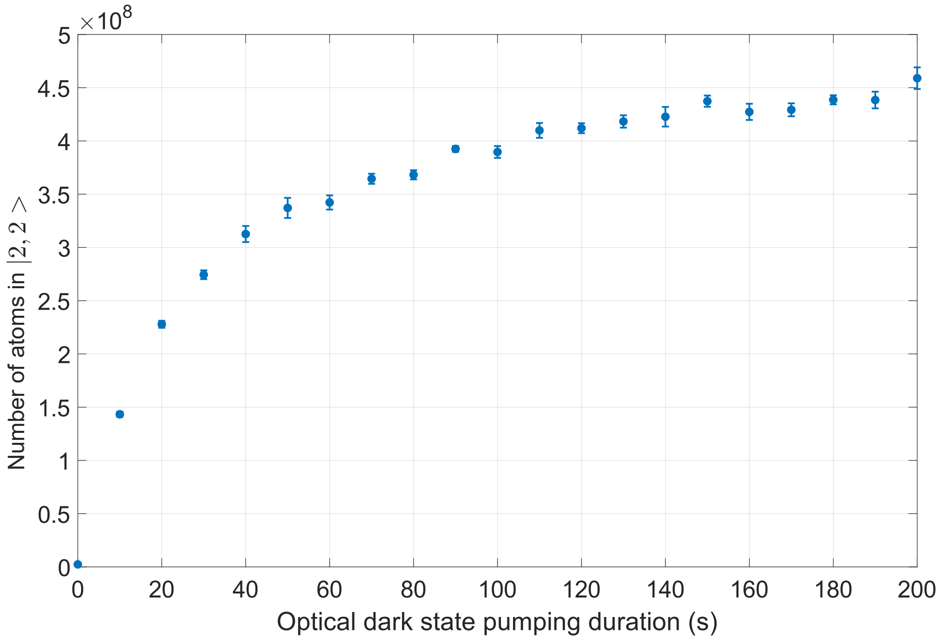

Figure 3.24: Atom number in the dark state as a function of the pumping time - The atom number saturates for pumping times longer than ca. $150\,\mu\mathrm{s}$. We stop the dark state pumping here, to stop scattering additional photons and avoid any further expansion of the cloud that would reduce the phase-space density.

3.4.2 Loading and Adiabatic Compression of the Magnetic Trap

When we initially load the atoms into the magnetic trap after the optical dark state pumping, we need to be careful to not lose phase-space density. The optimal loading procedure is a diabatic projection of the initial density distribution on the magnetic trap potential [66]. There are four mechanisms that could reduce the final PSD in the magnetic trap. A non-zero initial momentum of the whole atomic cloud adds kinetic energy to the atoms in the trap. This is avoided by using two counter-propagating beam paths for the optical dark state pumping. Also, an initial displacement of the cloud's center of mass from the trap center results in additional potential energy after the diabatic projection. We prevent this by ensuring that the cloud's position doesn't change during the cMOT and DSP. Finally, the initial capture gradient of the magnetic trap could be either too steep or too shallow. If it is too steep, we will imprint too much potential energy onto the cloud and if it is too shallow, the cloud will expand and the density will be reduced. One can calculate the optimum gradient for an initial cloud with given temperature and width (see appendix A.2). For our case the calculated optimum gradient is ca. $13\,\mathrm{G/cm}$.

The position of the atoms after the DSP is determined by the cMOT position, which in turn depends on the position of the magnetic field zero of the MOT coils. As discussed in section 3.2.2, the magnetic field zero positions of the MOT coils and Feshbach coils don't align. We thus only use the MOT coils in anti-Hemlholtz mode for the initial loading of the magnetic trap. We empirically optimize the loading procedure and end up with programming a linear current ramp from $0\,\mathrm{A}$ to $20\,\mathrm{A}$ within $10\,\mathrm{ms}$ that would correspond to a linear ramp of the gradient to $18\,\mathrm{G/cm}$. However upon closer inspection of the current with the current transducers, we see that the initial voltage of $30\,\mathrm{V}$ that we apply to the IGBT causes a sudden increase in the current as soon as we open the IGBT to switch on the current. As a result we don't end up with a linear ramp but the current initially overshoots its target value such that we rather apply a gradient of ca. $10\,\mathrm{G/cm}$ within ca. $500\,\mu\mathrm{s}$. The current then slowly adapts to the set value such that it stabilizes at $18\,$G/cm at the end of the ramp. While this behaviour is not directly programmable, it is accurately reproducible in every experiment run. In the future, we might improve the diabatic loading by adding a high voltage capacitor bank to the coil circuit.

Once the atoms are loaded into the trap, we want to kick-start the evaporation process. It can be shown (see appendix A.3) that the elastic collision rate Γ_{el} scales as $\Gamma_{\mathrm{el}} \propto b^{4/3}$ with the magnetic field gradient b, while the PSD remains constant under adiabatic changes of the gradient. It is therefore desirable to use as high magnetic field gradients as possible to start the evaporative cooling. We realize this, by combining both the MOT and the Feshbach coils in anti-Helmholtz configuration to create a magnetic trap with a maximum gradient of $522\,$G/cm at $200\,$A per coil pair. After capturing the atoms with the MOT coils, we linearly ramp up the current in both coils to ca. $199.6\,$A within $22.39\,$ms to create a combined gradient of $500\,$G/cm. This shifts the position of the magnetic field zero by a few hundred micro meter. From this point on, we make sure to only change the current in both coils in common mode to avoid drifts of the magnetic field zero position.

While adiabatically compressing the cloud, we apply a constant radio frequency of $950\,$MHz to remove the hottest atoms. We keep the gradient at $500\,$G/cm for $10\,$ms before measuring the atom number and temperature. The details of this measurement are described in appendix A.4. We end up with ca. 4.4×10^8 atoms at a temperature of ca. $390\,$µK and a peak density of ca. $5 \times 10^{12}\,$cm^{-3} resulting in a PSD of ca. 1×10^{-4}.

3.4.3 Majorana Losses and Optical Plug

When trapping neutral atoms in a magnetic quadrupole field, the motion of the atoms in the trap can induce transitions from trapped low-field seeking states to untrapped high-field seeking states because the field is not static in the atom's moving frame. Near the center of the trap where the magnetic field is small, the atom's magnetic moment cannot adiabatically follow the direction of the magnetic field. This results in a so-called Majorana spin-flip and the atom is lost from the trap. The corresponding loss rate scales as T^{-2} with the temperature T [85]. This process thus poses a fundamental limit to successful evaporative cooling in such a trap. This issue can be solved by 'plugging' the 'Majorana hole' with a tightly focused blue-detuned laser beam that repels the atoms from the trap center [4].

We had initially set up a laser system using a $5\,$W output power single frequency laser at $532\,$nm (footnote [46]) focused to a $1/e^2$ beam waist radius of $18\,$µm. However the achieved repulsive potential barrier height of ca. $600\,$µK was not sufficient to enable successful evaporative cooling. We therefore decided to change the wavelength in order to achieve a higher repulsive potential with less optical power. Even when going much closer to the atomic resonance, heating due to photon scattering is still suppressed, because the atoms are repelled from the regions with the highest intensities. Considering commercially available light sources and the achievable potential barrier height, we chose to use a $660\,$nm multi-mode laser[47] with maximum $1.2\,$W output power[48].

We install the laser on a separate breadboard and couple the light into a polarization-maintaining optical fiber[49]. This fiber-coupled setup avoids pointing instabilities of the plug position that could be caused by an AOM in a free-space setup. We use an AOM[50] in front of the fiber to quickly turn the beam on and off. We also include a mechanical shutter to keep the AOM thermalized while still blocking the beam when the residual photon scattering from the plug might be disadvantageous during the experimental cycle. This setup is depicted in figure 3.25 (a). The beam setup on the experiment table is shown in figure 3.25 (b). We collimate the plug beam in the $x - y$ plane with a commercial fiber collimator[51] to a $1/e^2$ beam waist radius of ca. $725\,\mu\text{m}$. We use a wedged glass window to reflect part of the light onto a photodiode to monitor the optical power[52]. We then magnify the beam with a $3:10$ telescope[53] before we focus it onto the atoms under an angle of ca. 15° with respect to the y-axis. As the final lens, we use a $f = 200\,\text{mm}$ achromat[54] such that we achieve a $1/e^2$ beam waist radius of $w_{\text{plug}} = 18\,\mu\text{m}$ in the focus. This value was chosen as a trade-off between repulsive barrier height and convenience for the experimentalists, since the alignment of smaller foci is more difficult and less stable. We end up with ca. $700\,\text{mW}$ optical power in front of the glass cell so that the potential barrier height in the magnetic trap is ca. $1280\,\mu\text{K}$.

---

[46] Azur Light Systems: ALS-GR-532-5-I-SF

[47] Laser quantum (now Novanta Photonics): gem 660

[48] The polarizability of Lithium at $660\,$nm is ca. 17.5 times larger than at $532\,$nm.

[49] Thorlabs: P3-630PM-FC-2

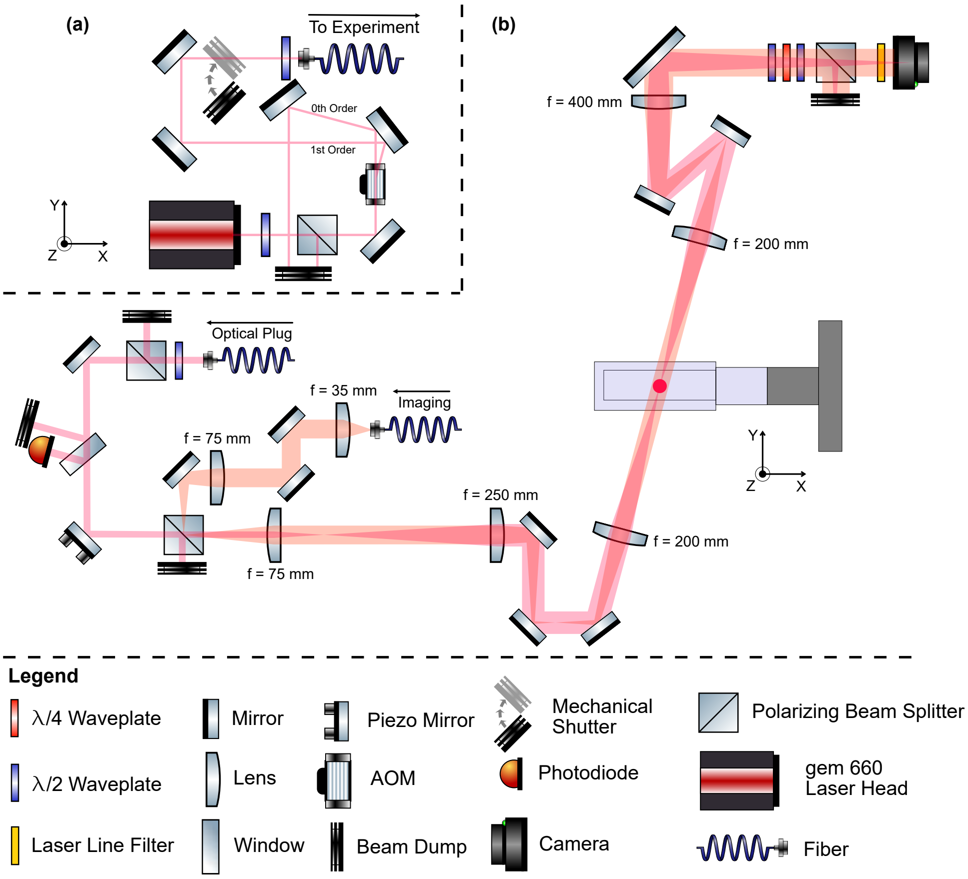
(a)
To Experiment
0th Order
1st Order
Y
Z
X
(b)
f = 400 mm
f = 200 mm
Optical Plug
f = 35 mm
Imaging
f = 75 mm
f = 250 mm
Y
Z
X
f = 200 mm
f = 75 mm
Legend
λ/4 Waveplate
Mirror
Piezo Mirror
Mechanical Shutter
Polarizing Beam Splitter
λ/2 Waveplate
Lens
AOM
Photodiode
gem 660 Laser Head
Laser Line Filter
Window
Beam Dump
Camera
Fiber

Figure 3.25: Laser system for the optical plug - **(a)** We couple the light into a fiber on a separate breadboard and use an AOM as well as a mechanical shutter to turn the light on and off. **(b)** The light for the optical plug (magenta) is first collimated, then enlarged by a telescope and lastly focused onto the atoms. By placing a piezo mirror in front of the expanding telescope, we can precisely adjust the transversal position of the focus. We overlap an imaging beam (orange) with the optical plug to help with this alignment. The beam path lengths are not to scale.

---

[50] Gooch & Housego: AOMO 3080-125

[51] Schäfter + Kirchhoff: 60FC-4-M8-10

[52] We had also used the two reflexes for an intensity lock of the plug beam [87]. However we found it not necessary to actively stabilize the beam's intensity.

[53] Thorlabs: LA1608-B $f = 75\,\text{mm}$, LA1461-B-ML $f = 250\,\text{mm}$

[54] Edmund Optics: ACH YAG-BBAR $f = 200\,\text{mm}$

To help with the adjustment of the plug beam onto the magnetic trap center, we set up an imaging system with a magnification of $M_{\text{plug}} = 2$ along the axis of the optical plug. We overlap the two beams in front of the atoms using a PBS. In front of the camera, we separate the two beams via a combination of $\lambda/2$-, $\lambda/4$-waveplates and a PBS and a laser line filter[55] mounted directly onto the camera. The Rayleigh length of the beam is ca. $z_{\text{R,plug}} \approx 1.5\,\text{mm}$. It is thus sufficient to use a z-translation stage with micrometer screws to adjust the longitudinal focus position onto the Majorana hole. The coarse alignment of the transversal focus position is also done by positioning the final lens with an xy-translation stage. For the fine adjustment we then use a precise mirror mount[56] with linear piezo-actuators[57] that we control via a commercial driver[58] and software [59]. In our first plug setup with the $532\,\text{nm}$ laser, we placed this piezo mirror directly in front of the final focusing lens. However we noticed that the minimum angle step-size $\Delta\theta$ of the piezo mirror in combination with the focal length $f_{\text{final}} = 200\,\text{mm}$ of the final focusing lens resulted in a minimum position change $\Delta x = f_{\text{final}} \cdot \tan(2\Delta\theta)$ that was too large to reliably adjust the transversal focus position. We solve this issue by placing the piezo mirror in front of an expanding $3:10$ telescope with focal lengths $f_1 = 75\,\text{mm}$ and $f_2 = 250\,\text{mm}$ that rescales the minimum focus displacement to $\Delta x' = \frac{f_1}{f_2} f_{\text{final}} \cdot \tan(2\Delta\theta)$. With this we are able to adjust the focus position much more precisely.

A typical adjustment procedure is shown in figure 3.26. We load the magnetic trap and perform RF evaporation to reduce the cloud size. We then tilt the piezo mirror along one axis in equidistant micro-steps and image the cloud along the plug imaging axis. We can directly see the position of the plug beam in the magnetic trap. The inlets in figure 3.26 show absorption images of the cloud for a good and a bad alignment of the plug beam. As we scan the plug beam across the Majorana hole, the atom number first increases and reaches a plateau where the Majorana losses are completely suppressed before the atom number decreases again. We note that the piezo mirror suffers from a severe hysteresis when changing the direction of the tilt. The position of the plug is stable over the course of several weeks to months. However depending on the respective experimental cycle, the thermalization of the magnetic field coils might change resulting in a slight shift of the magnetic field zero. When we worked with MOT loading times of $15\,\text{s}$ or longer, we observed a thermalization of the experiment over ca. $1\,\text{h}$. Ever since we are working with only $5\,\text{s}$ of MOT loading, we don't need to wait for the machine to thermalize. Once the plug beam is properly aligned, we measure the saturation of the optical power. We again perform RF evaporation to reduce the size and temperature of the atomic cloud. We then take absorption images to determine the atom number while reducing the optical power of the plug beam. The results of this measurement are shown in figure 3.27. We see that the atom number saturates for optical powers higher than $500\,\text{mW}$. We are thus confident that the potential barrier is high enough to ensure successful evaporation in the magnetic trap.

We can directly see the influence of the plug beam in absorption images of the magnetic trap taken from the MOT y imaging direction. Figure 3.28 shows the optical density for magnetically trapped atoms with and without the plug beam. In the case without the plug, we can directly see the depletion of atoms near the trap center that is caused by Majorana losses.

---

[55] OptoSigma: VPFHT-25C-6710

[56] Radiant-Dyes: MDI-HS-2-3025-M6

[57] Physik Instrumente: N-470 PiezoMike Linearaktor

[58] Physik Instrumente: E-872.401 Q-Motion

[59] Physik Instrumente: PIMikroMove

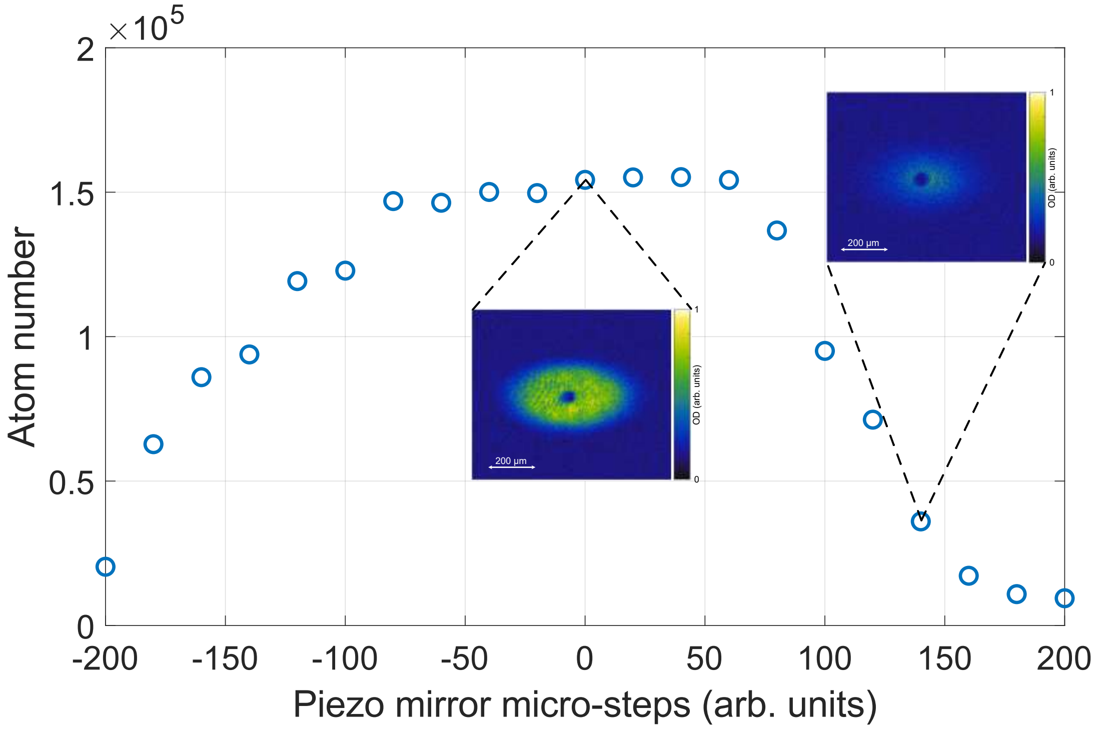

Figure 3.26: Plug adjustment procedure - We prepare atoms in the magnetic trap and perform RF evaporation to reduce the cloud size. We then scan the position of the plug beam and take absorption images along the plug imaging axis. For a good alignment, the Majorana hole is 'plugged' and the atom number reaches a maximum. The inlets show the OD images for a good and a bad alignment of the plug. The color scale is the same in both images.

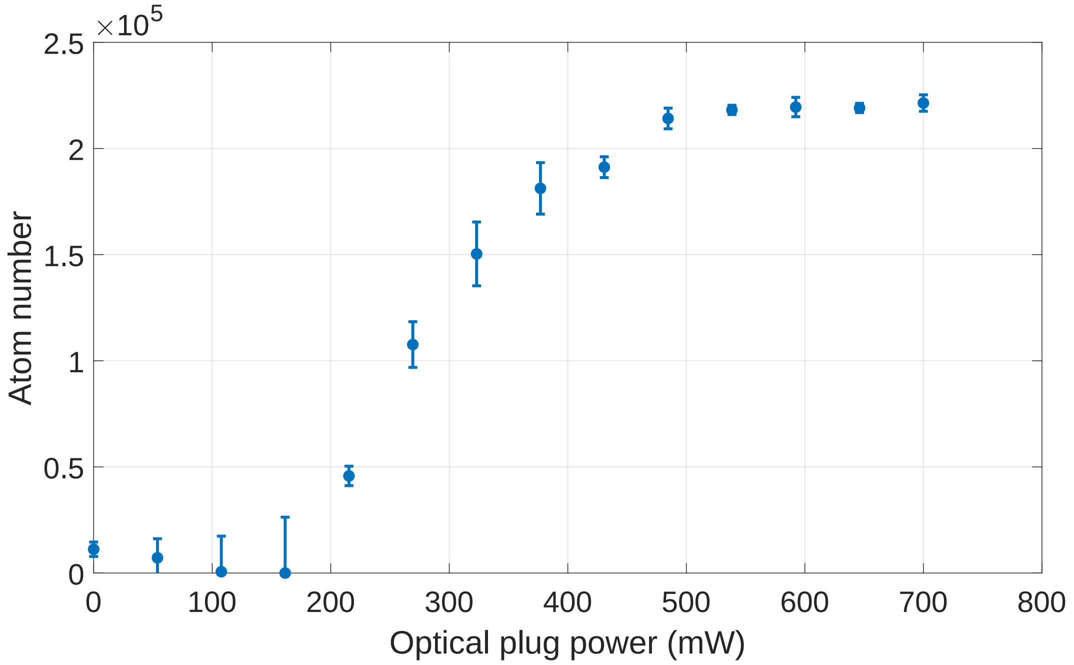

Figure 3.27: Saturation of the optical power of the plug beam - We measure the atom number in the magnetic trap after an RF evaporation and vary the optical power of the plug beam. For more than 500 mW, the atom number is saturated.

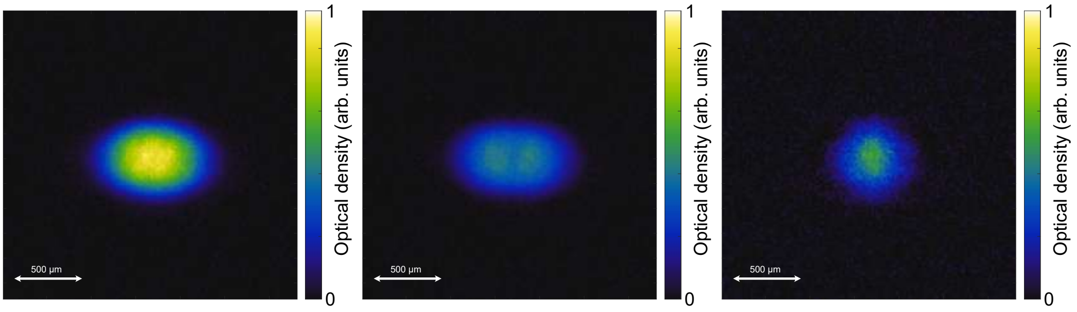

(a) Magnetic trap with plug (b) Without plug (c) Differential image

Figure 3.28: Influence of the plug beam on the optical density - We take in-situ absorption images of the atoms in the magnetic trap along the MOT y direction with **(a)** and without **(b)** optically plugging the Majorana hole. Since we don't image along the plug beam's line of sight, we don't see the repelling of atoms due to the plug. Instead, we can directly observe a depletion of atoms around the center in the magnetic trap without the optical plug. The difference of the first two images is shown in subfigure **(c)**. The color scale is the same for all three images.

After having successfully implemented the optical plug, we noticed that the magnetic trap is highly sensitive to low frequency RF noise. Frequencies in the range from a few kHz to several MHz can drive spin flips in the $F = 2$-manifold near the trap center, resulting in an effective anti-evaporation. We identified two main sources of RF noise that limited the lifetime in the trap. We had to remove the IGBT driver DC-DC converters (see section3.2.2) and the motorized rotation mounts that we previously used to rotate waveplates in the experiment [56]. Once we got rid of these noise sources, the lifetime in the magnetic trap increased by at least one order of magnitude. We measure lifetimes between $143(4)$ s and $15(1)$ s for gradients between 52.2 G/cm and 500 G/cm. Thus, the plugged quadrupole trap provides now the perfect starting conditions for evaporative cooling.

3.4.4 Radio Frequency Evaporation

We use a so-called RF knife to remove the hottest atoms from the magnetic trap. We apply a tunable radio frequency that is generated by mixing a fixed frequency of 800 MHz from an RF signal generator[60] with a tunable frequency in the range of 1 MHz - 200 MHz generated by a digital RF source developed in our group [88, 57]. The signal is amplified with a 30 W amplifier[61] and coupled into our broadband antenna (see figure 3.8). The atoms with the highest kinetic energy have trajectories that bring them in resonance with the applied radio frequency. The RF transition induces a spin-flip and the atoms are then expelled from the trap. By dynamically tuning the frequency we can vary the cut-off for the kinetic energy in the trap.

To enhance the elastic scattering rate for fast rethermalization, we adiabatically compress the magnetic trap to a gradient of 500 G/cm. However as the atomic cloud is cooled, the density increases and the density-dependant three-body losses may become the dominant loss mechanism. To prevent this, we need to adiabatically decompress the magnetic trap during the evaporative cooling. Any shift of the magnetic field center would cause a misalignment of the optical plug and may introduce Majorana losses. We thus simultaneously ramp down the current in both the Feshbach and the MOT coils in common mode. However, as we reduce the magnetic field gradient, the magnetic field zero position might still be shifted due to any residual magnetic stray fields. We thus need to make sure to properly cancel any residual fields with the 3D offset coils. We optimize the stray field compensation by comparing the position of a magnetic trap at a steep gradient (e.g. $500\,\mathrm{G/cm}$) with the position of a trap with a shallower gradient (e.g. $52.2\,\mathrm{G/cm}$), while scanning the current through the offset coils in a certain direction[62]. An example of this optimization is shown in figure 3.29 for the z-axis.

---

[60] Windfreak Technologies: SynthHD (v2)

[61] Mini Circuits: ZHL-30W-252-S+

During his PhD thesis, Niklas Käming developed a direct simulation Monte-Carlo approach to optimize the evaporation in our magnetic trap [89] (footnote [63]). As of writing this thesis, this simulation is not completely functional and we hence empirically optimize the evaporation process. We get the best result by employing three separate evaporation stages with linear ramps of the radio frequency and the magnetic field gradient. These ramps are displayed in figure 3.30 and the respective results for the achieved phase-space density are summarized in table 3.5. We stop the RF evaporation in the magnetic trap before reaching quantum degeneracy after $7.3\,\mathrm{s}$ at a PSD of ca. 9×10^{-2}.

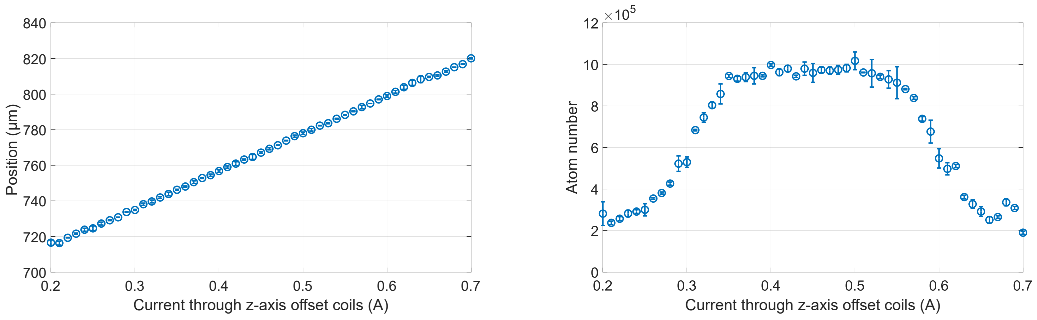

(a) (b)

Figure 3.29: Optimizing the stray field compensation along the z-axis - We load a magnetic trap, perform RF evaporation and adiabatically ramp the magnetic field gradient to $52.2\,\mathrm{G/cm}$. We then image the atoms along the plug imaging axis for different currents through the z-axis offset coils. **(a)** As the offset field is varied we observe a displacement of the trap position along the z-axis. We can compare this to the position of a tightly confined magnetic trap where offset fields don't influence the position as much. **(b)** We plot the atom number as a function of the current through the coils. If the stray fields are badly compensated, the clouds position changes during the adiabatic decompression and the atom number decreases due to Majorana losses. The current range of the observed plateau corresponds to a position range of ca. $30\,\mathrm{\mu m}$, indicating that we work in the well saturated regime of the optical plug power.

Table 3.5: Overview of the evaporative cooling in the magnetic trap - The evaporation takes ca. $7.3\,\mathrm{s}$ during which the phase-space density is increased by ca. three orders of magnitude from 1×10^{-4} to 9×10^{-2}.

Stage	**Duration** (s)	**Atom Number**	**Temperature** (µK)	**Peak Density** n_0 (10^{12} cm^{-3})	**PSD** ρ_0
Capture & Compression	0.03	4.4×10^8	390	5.0	1×10^{-4}
Evaporation Ramp 1	3	1.6×10^8	211	1.8	2×10^{-4}
Evaporation Ramp 2	3.3	1.0×10^7	36	6.8	9×10^{-3}
Evaporation Ramp 3	1	3.2×10^6	16	20.9	9×10^{-2}

---

[62] This procedure is very precise and we use this to also cancel stray fields during the Gray Molasses cooling.

[63] This work is inspired by a similar optimization process implemented at the MIT [45]

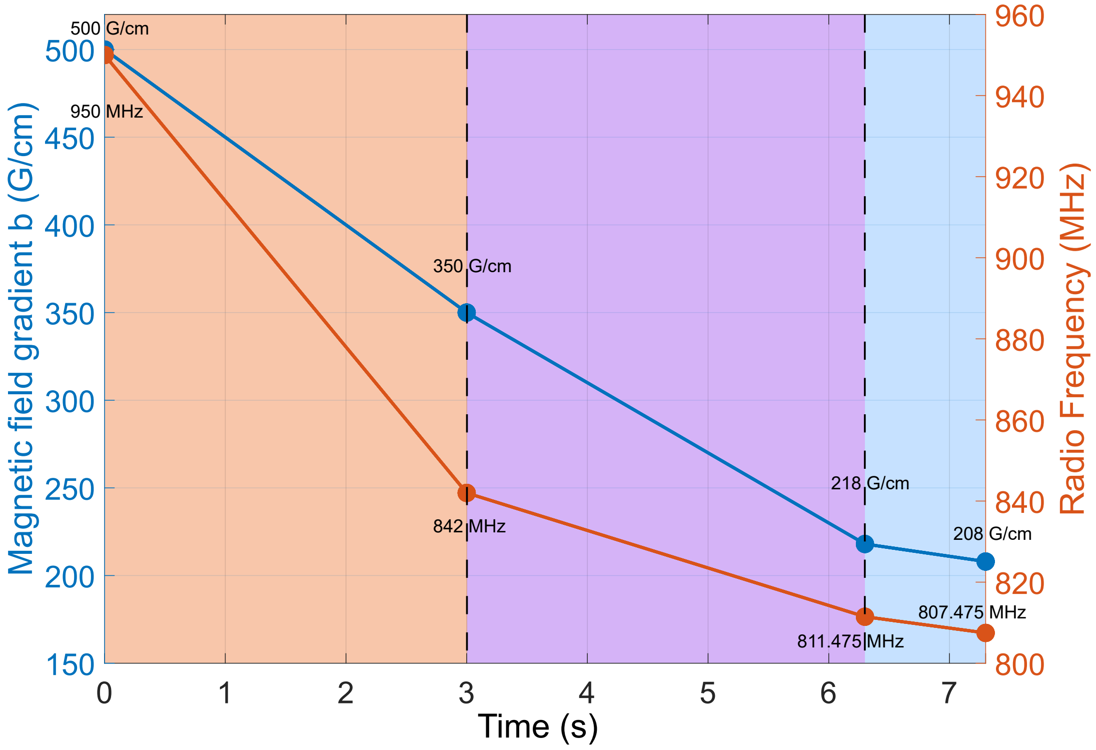

Figure 3.30: Magnetic field gradient and radio frequency during the evaporation - We linearly ramp both the RF and the magnetic field gradient in three separate stages taking overall $7.3\,\mathrm{s}$. The initial capture and compression of the magnetic trap is not shown.

3.5 | Evaporation in the Crossed Optical Dipole Trap

At zero magnetic field, the atoms in the $|F = 2, m_F = 2\rangle$-state experience a negative scattering length of $a_{|2,2\rangle} = (-27.6 \pm 0.5)\,a_0$. These attractive interactions have limited the condensate numbers in early ^{7}Li experiments [41] until [90] showed that condensation near the Feshbach resonances of the $F = 1$-manifold (see section 2.5) is favorable. To address those Feshbach resonances we need to apply DC magnetic fields between ca. $600\,\mathrm{G}$ to $1100\,\mathrm{G}$. This is not compatible with a magnetic trap. We therefore stop the evaporation in the magnetic trap before reaching quantum degeneracy and load the atoms into a crossed optical dipole trap [49]. Here, we perform an adiabatic state transfer from the $|F = 2, m_F = 2\rangle$-state to the $|F = 1, m_F = 1\rangle$-state. We ramp up the bias field close to $702\,\mathrm{G}$ near the Feshbach resonance of $|F = 1, m_F = 1\rangle$ to increase the scattering length to ca. $76\,a_0$. We then evaporatively cool the atoms by lowering the intensity of the dipole trap until we reach quantum degeneracy.

3.5.1 Laser System for the Optical Dipole Trap

Initially, we tried to evaporate in a dipole trap that was only slightly modified from our previous setup described in [56–58] (footnote [64]). However, we could not achieve Bose-Einstein condensation due to heating from unwanted Raman processes that were caused by unfortunate choices of the intersection angles and the multimode nature of the laser source[65]. We have thus set up a completely new laser system with a single-frequency diode pumped solid-state laser[66] at a wavelength of $1064\,\mathrm{nm}$ with a spectral linewidth $\leq 3\,\mathrm{kHz}$ and an optical output power of ca. $56\,\mathrm{W}$. We also planned to change our optical lattice system from a static triangular lattice (described in [57, 58]) to a multi-frequency lattice (MFL) with dynamically tunable geometry (see chapter 4). To save resources, we decided to combine both laser systems.

---

[64] We increased the trap volume and removed the motorized rotation mount that generated RF noise.

[65] IPG Photonics: YLR-100-LP-A

We intersect three fiber-coupled beams under relative angles of $120°$ in the $x-y$ plane. They are focused to a $1/e^2$ beam waist radius of $41(3)\,\mu\mathrm{m}$ [57] ca. $100\,\mu\mathrm{m}$ below the center of the magnetic trap. This is close enough to get a good loading efficiency but still far away from the repelling plug beam and the Majorana hole. The three beams are linearly polarized out of plane. We detune the frequency of the three beams such that the emerging running standing waves propagate faster than the relevant energy-/time-scales. This washes out the interference pattern and the atoms only see the time-averaged harmonic potential. When we want to load the atoms from the harmonic potential into the optical lattice, we simply change the detuning to re-establish the interference of the beams. We can thus use a single laser system to create both the harmonic potential for the creation of the BEC and the optical lattice. Additionally, with this setup the dipole trap and the lattice are always automatically perfectly aligned onto each other. A sketch of the alignment of the three beams as well as CAD models of the focusing telescopes are shown in figure 3.31.

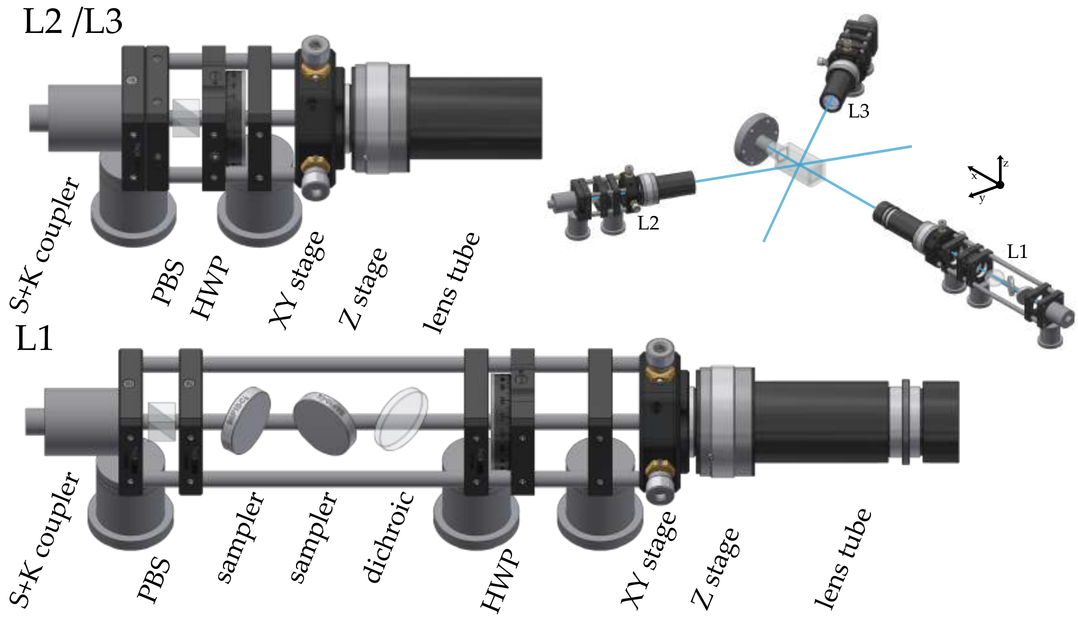

Figure 3.31: Sketch of the dipole trap telescopes and their arrangement around the glass cell - The light is collimated and the polarization is cleaned by a PBS. A $\lambda/2$-waveplate rotates the polarization out of plane and a final lens focuses the beam onto the atoms. The focus position can be adjusted with xyz translation stages. In the $L1$ telescope, a dichroic mirror is used to overlap the beam with an additional imaging beam and two beam samplers are used as pick-ups for the intensity lock. The rest of the intensity lock optics is not shown. Figure adapted from [57].

We label the three beams $L1$, $L2$ and $L3$. The two beams $L2$ and $L3$ pass through the glass cell before they are collimated and guided onto a water-cooled laser beam dump. We pick up part of the light with wedged glass windows and reflect it onto two photo diodes[67] per beam. We use one of the photodiodes for an intensity lock based on [87] and the other for monitoring purposes. The relative intensity noise spectra for one of the lattice beams with and without the intensity lock are shown in figure B.1 of appendix B. The beam $L1$ enters the glass cell on the front face and is dumped into the vacuum chamber. Here, we add two beam samplers[68] in the telescope to also establish an intensity lock and monitoring. Each of the three telescopes starts with a fiber collimator[69] followed by a PBS to clean the polarization. Additional $\lambda/2$-waveplates rotate the polarization out of plane before the final achromatic lenses[70] focus the beams onto the atoms. Each lens is mounted to both a transversal[71] and a longitudinal[72] translation stage. The $L1$ telescope also includes a dichroic mirror[73] that is used to overlap the beam with an imaging beam which is not used in this thesis.

---

[66] Coherent: Mephisto MOPA

[67] Thorlabs: PDA10A2

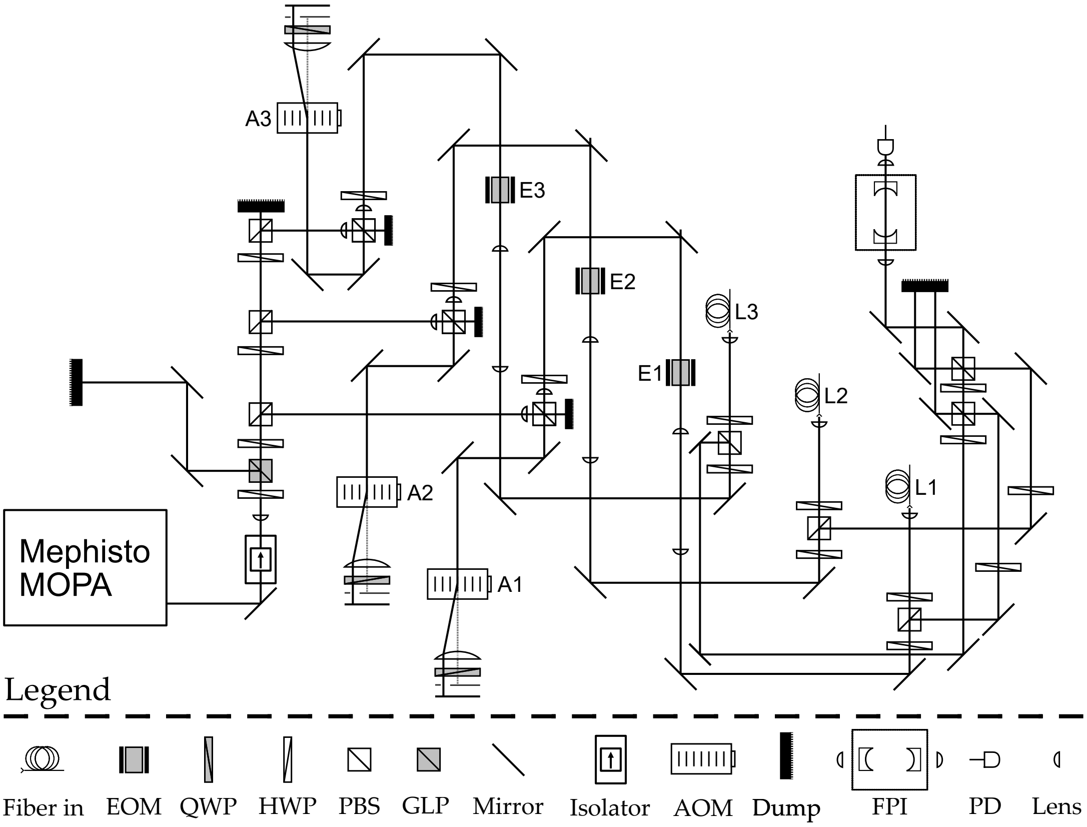

Figure 3.32: Laser system for the optical dipole trap and the optical lattice - We first use an optical isolator to prevent the laser head from damages due to reflections. We then use $\lambda/2$-waveplates, a Glan-laser polarizer (GLP) and PBS to distribute the light to the three beam paths. In each path we install an AOM in double-pass configuration ($A1$, $A2$ and $A3$) and an EOM ($E1$, $E2$ and $E3$) to switch between dipole trap, resonant triangular lattice or multi-frequency lattice. We can monitor the sidebands via a FPI and a photodiode (PD). As a library for optical components the author used [57, 81].

Figure 3.32 shows the laser system in front of the optical fibers. The laser has an output power of up to $56\,\mathrm{W}$. We first install an optical isolator[74] to prevent damage to the laser head caused by back-reflections. A $\lambda/2$-waveplates in combination with a GLP can be used to guide most of the optical power into a beam dump for safe adjustment of the optics. This is followed by a series of $\lambda/2$-waveplates and PBS to distribute the power equally to the three beam paths. If necessary, this setup can be extended for additional beams in the future. In order to switch between optical dipole trap and lattice, we need to adjust the frequency of each beam individually without damaging the optical fiber due to pointing instabilities. We thus install an AOM[75] ($A1$, $A2$ and $A3$) in double-pass configuration in each of the three beam paths. We also use these AOMs for fast switching and to control the intensity of each beam. The EOMs ($E1$, $E2$ and $E3$)[76] can be used to modulate frequency sidebands onto each beam. We monitor the sidebands by reflecting part of the light from PBS in front of the fibers onto a Fabry-Perot cavity. We use high power single mode polarization-maintaining photonic crystal fibers[77] that we couple with commercial fiber collimators[78]. If we use the maximum accessible optical power, we expect to couple ca. $10\,$W through each fiber. This setup is designed to provide light for an optical dipole trap for evaporation and matter-wave microscopy (see chapter 5) as well as a multi-frequency lattice with tunable geometry or a deep triangular pinning lattice for conventional quantum gas microscopy.

---

[68] Thorlabs: BSF10-C

[69] Schäfter + Kirchhoff: 60FC-SMA-T-23-M25-03

[70] Thorlabs: AC254-150-C, $f = 150\,\mathrm{mm}$

[71] Thorlabs: CXY1

[72] Thorlabs: SM1ZM

[73] Thorlabs: DMLP900

[74] EOT (now Coherent): PavosUltra+ 4mm Isolator-1064nm-000- 045-21C-56W

3.5.2 Loading the Optical Dipole Trap and Adiabatic State Transfer

As long as we don't work with deep pinning lattices for conventional quantum gas microscopy, we don't need the full power of the laser system. We thus limit the optical power to ca. $4\,$W per beam in order to get a better resolution for the intensity lock. The trapping potential U_{dip} for an optical dipole trap with the intensity distribution $I(\boldsymbol{r})$ is given by [49]:

$$U_{\mathrm{dip}}(\boldsymbol{r}) = -\frac{3\pi c^2}{2\omega_0^3}\left(\frac{\Gamma}{\omega_0-\omega}+\frac{\Gamma}{\omega_0+\omega}\right) I(\boldsymbol{r}), \tag{3.6}$$

with the speed of light c, the resonance frequency ω_0 and the natural linewidth Γ of the atomic transition and the laser frequency of the dipole trap ω. With the three non-interfering Gaussian beams, the resulting potential can be approximated by a harmonic potential

$$U(x,y,z) \approx \frac{1}{2}m(\omega_x^2x^2+\omega_y^2y^2+\omega_z^2z^2), \tag{3.7}$$

with the mass of Lithium m and the respective trap frequencies $\omega_{x,y,z}$. To start loading the atoms into the dipole trap, we linearly ramp up the power of the three beams to $3.5\,$W each within $50\,$ms, while we keep the magnetic field gradient at $208\,$G/cm. With the $1/e^2$ beam waist radii of $41\,$µm this results in an attractive potential depth of $U(0) = -240.6\,$µK and trap frequencies of $\omega_x = \omega_y = 2\pi \times 2.86\,$kHz and $\omega_z = 2\pi \times 4.13\,$kHz, respectively. At this trap depth the dipole trap already starts to dominate and part of the atoms are transferred from the magnetic trap to the dipole trap. We then adiabatically ramp down the magnetic field gradient to zero within $50\,$ms. At the same time, we ramp up a bias field of ca. $0.1\,$G along the z-axis with the 3D offset coils to maintain the polarization of the atoms. The direction of this field is chosen such that the magnetic field zero is shifted upwards away from the dipole trap during the adiabatic turn-off of the magnetic trap. We end up with ca. 1.1×10^6 atoms in the dipole trap at a temperature of $24.4(1)\,$µK and a PSD of ca. 9.7×10^{-3}.

We then perform a so-called Landau-Zener sweep to adiabatically transfer the atoms from the $|F = 2, m_F = 2\rangle$-state to the $|F = 1, m_F = 1\rangle$-state. We couple the two states off-resonantly by applying a radio frequency signal and then adiabatically sweep the coupling across the resonance so that the internal state of the atoms is changed via an avoided crossing. At a bias field B_0, the resonant coupling frequency ν_{res} between the two states is given by the energy difference of the two states as

---

[75] Gooch & Housego: AOMO3080-197

[76] QUBIG: EOM PM7-NIR_2.2, EOM PM7-NIR_7.8, EOM PM7-NIR_9.9

[77] NKT Photonics: Photonic crystal fiber, aeroGUIDE POWER-15-PM, length $5\,$m

[78] Schäfter + Kirchhoff: 60FC-SMA-T-23-M25-03

$$h\nu_{\mathrm{res}}(B_0) = E_{|2,2\rangle}(B_0) - E_{|1,1\rangle}(B_0) \tag{3.8}$$

$$\nu_{\mathrm{res}}(B_0) \approx 803.5\,\mathrm{MHz} + 2.1\,\mathrm{MHz/G} * B_0, \tag{3.9}$$

where we used $\mu_{\mathrm{B}} \approx 1.4\,\mathrm{MHz/G}$. One can now either smoothly vary the coupling radio frequency at a fixed bias field or one can vary the bias field while keeping the radio frequency constant. The resonant coupling of the two states must be strong enough to allow for fast and efficient sweeps. We found that the coupling strength of our broadband antenna that we use for the RF evaporation in the magnetic trap was not sufficient. We thus built a custom impedance-matched antenna (see figure 3.10a) with a measured input return loss of ca. $-36\,\mathrm{dB}$ at $813.625\,\mathrm{MHz}$. With this antenna we measure resonant Rabi frequencies of ca. $2\pi \times 10\,\mathrm{kHz}$ with an RF power of $40\,\mathrm{dBm}/10\,\mathrm{W}$ at a bias field of ca. $4.8\,\mathrm{G}$. As we now linearly ramp the magnetic bias field B_0 from $0.1\,\mathrm{G}$ across the resonance at $4.8\,\mathrm{G}$ to $9.5\,\mathrm{G}$ within $40\,\mathrm{ms}$, the atoms are transferred from the $|F = 2, m_F = 2\rangle$-state to the $|F = 1, m_F = 1\rangle$-state. Figure 3.33 shows the relative population of both states during this sweep. The measured fidelity is indistinguishable from $100\,\%$.

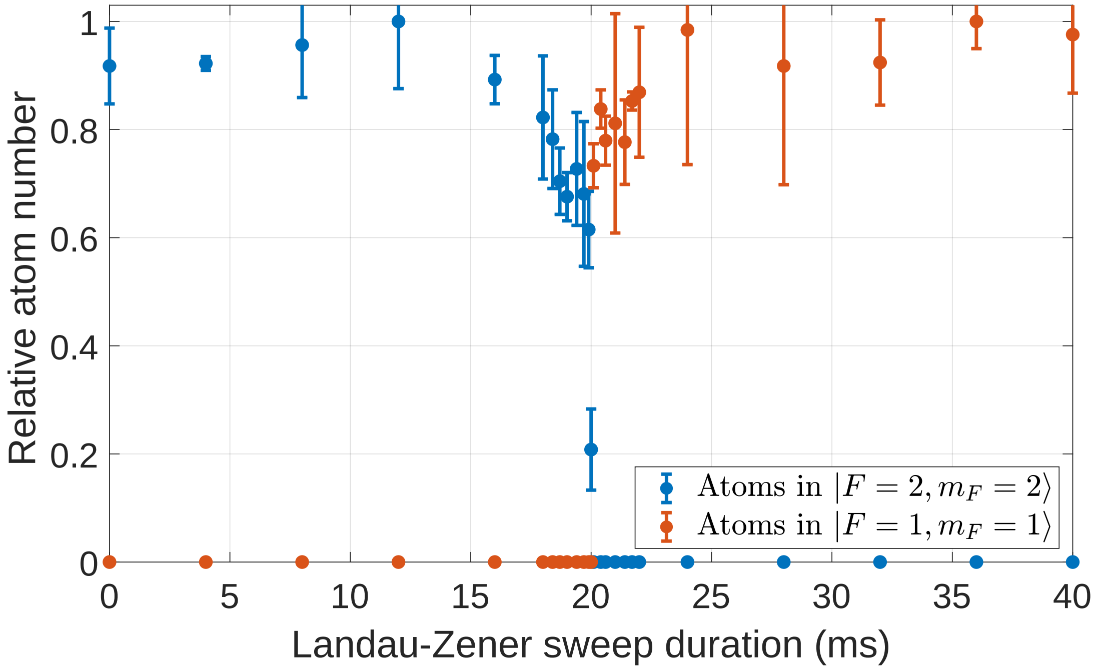

Figure 3.33: Adiabatic state transfer in the optical dipole trap - We apply a constant radio frequency of $813.625\,\mathrm{MHz}$ to couple the two states, while linearly ramping the magnetic field across the resonance. We transfer the atoms to the $|F = 1, m_F = 1\rangle$-state with a fidelity of almost $100\,\%$.

3.5.3 Evaporation near the Feshbach Resonance

After the Landau-Zener sweep, we linearly ramp down the bias field from the 3D offset coils to zero while ramping up the current through the Feshbach coils in Helmholtz configuration to generate a homogeneous field of $702\,\mathrm{G}$ within $100\,\mathrm{ms}$. At this magnetic field close to the Feshbach resonance, the atoms in state $|F = 1, m_F = 1\rangle$ experience a scattering length of ca. $76\,a_0$, allowing for fast rethermalization during evaporative cooling. Once the magnetic field ramp is complete, we start lowering the intensity of the dipole trap beams according to the following formula:

$$I(t) = I_0 \exp\left\{\left(-\frac{t}{\tau}\right)\right\}, \tag{3.10}$$

where I_0 is the initial intensity and τ is the characteristic time constant of the evaporation. We empirically find the optimum evaporation time constant at $\tau = 0.2\,\mathrm{s}$. We evaporate for $0.8\,\mathrm{s}$ and reduce the initial power of $3.5\,\mathrm{W}$ per beam to ca. $64\,\mathrm{mW}$ per beam, corresponding to a final trap depth of $U_{\mathrm{final}}(0) = -4.4\,\mu\mathrm{K}$ and trap frequencies of $\omega_x = \omega_y = 2\pi \times 386\,\mathrm{Hz}$ and $\omega_z = 2\pi \times 536\,\mathrm{Hz}$. With this exponential ramp, we get an almost pure BEC of ca. 1×10^5 atoms at a temperature of ca. $220\,\mathrm{nK}$ and a condensate fraction of $94\,\%$. Taking into account some time for the initialization of every run and taking the absorption images, the overall cycle time is ca. $14\,\mathrm{s}$. Figure 3.34 shows absorption images of the cloud at varying steps during the evaporation process.

In a three-dimensional harmonic trap, the transition temperature T_{C} and the condensate fraction N_{C}/N are given by [91]:

$$k_{\mathrm{B}}T_{\mathrm{C}} \approx 0.94 h\bar{f}N^{1/3} \tag{3.11}$$

$$\frac{N_{\mathrm{C}}}{N} = 1 - \left(\frac{T}{T_C}\right)^3, \tag{3.12}$$

where N_{C} is the number of particles in the condensate, N is the total atom number, k_{B} is the Boltzmann constant, h is Planck's constant and $\bar{f}$ is the geometric mean of the trap frequencies. For our final trap frequencies at the end of the evaporation, this corresponds to a transition temperature of $913\,\mathrm{nK}$ at 1×10^5 atoms. We measure the onset of Bose-Einstein condensation at a temperature of $900(50)\,\mathrm{nK}$.

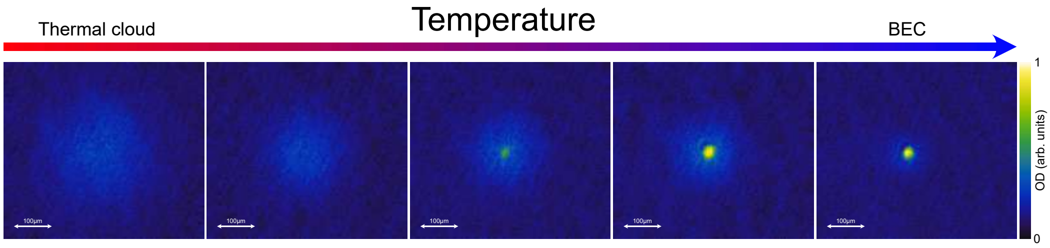

Figure 3.34: Evaporation in the optical dipole trap - We stop the evaporation process at varying times during the exponential decrease of the optical potential and take absorption images after $2\,\mathrm{ms}$ time of flight at $702\,\mathrm{G}$. We thus end up with atomic clouds of varying temperature. The longer we perform the evaporation, the colder the cloud gets before we achieve Bose-Einstein condensation.

CHAPTER 4

A Multi-Frequency Optical Lattice for Dynamic Control of the Lattice Geometry

Making use of the optical dipole force [49], one can create periodic potentials for ultracold neutral atoms, by interfering two or more laser beams of the same frequency. This can then be used to emulate condensed matter systems, in particular crystals with a periodic spatial structure [8, 92]. These experiments come with a high degree of control, as the interactions can be tuned via Feshbach resonances [11] and the dimensionality and lattice structure can be chosen by the experimentalist [93], enabling us to even study exotic systems far beyond condensed matter physics. At the same time, it is possible to access both the momentum distribution of the atoms via time-of-flight experiments as well as the real-space distribution [15, 16].

The ability to tune the geometry of the optical lattice between different lattice structures is not only appealing for realizing different model systems within the same experimental setup but also dynamic tunablitiy opens the way to exploring new types of driven systems as well as accessing new preparation and quench methods. There are several different approaches on a dynamic control of the lattice geometry. When using $d+1$ laser beams in d dimensions, the resulting optical lattice has an intrinsically stable geometry which is in turn also static [94]. The geometry depends on the polarization of the lattice beams, which can typically be tuned only slowly compared to relevant time-scales in the experiment. Approaches for a fast dynamical tuning of the geometry rely on additional laser beams or frequencies [95–101] but with the exception of [19, 102] require phase locks for a controlled and stable geometry.

During this theses, we implemented the multi-frequency approach from [19], that combines the passive stability of the lattice geometry with the ability to tune the lattice geometry between triangular [103, 104] and honeycomb [97, 105] lattice on the µs-scale without the need of a phase lock. The multi-frequency lattice was set up and characterized by the author together with Justus Brüggenjürgen under the supervision of Christof Weitenberg.

4.1 | Tuning of the Lattice Geometry

The concept of the multi-frequency lattice is to overlay three independent 1D lattices such that they form a combined 2D hexagonal lattice. By independently controlling the phase of each 1D lattice, one can tune the overall geometry between a triangular lattice (where the nodes of all three lattices overlap in the same points) via boron-nitride lattices to a honeycomb lattice (where one of the 1D lattices is shifted by half a lattice constant). The three 1D lattices are realized by interfering three laser beams in the $x-y$ plane under relative intersection angles of 120°. Each lattice beam with wavevector $\boldsymbol{k}_\mathrm{i}$, $(\mathrm{i}=1,2,3)$ is linearly polarized out of plane and has two frequency components, such that each frequency appears twice. There are thus in total three frequencies ν_a, ν_b and ν_c. Each frequency pair then forms a 1D-lattice, the translation of which can be controlled by varying the phase of the corresponding frequency components in one of the beams. This concept is illustrated in figure 4.1.

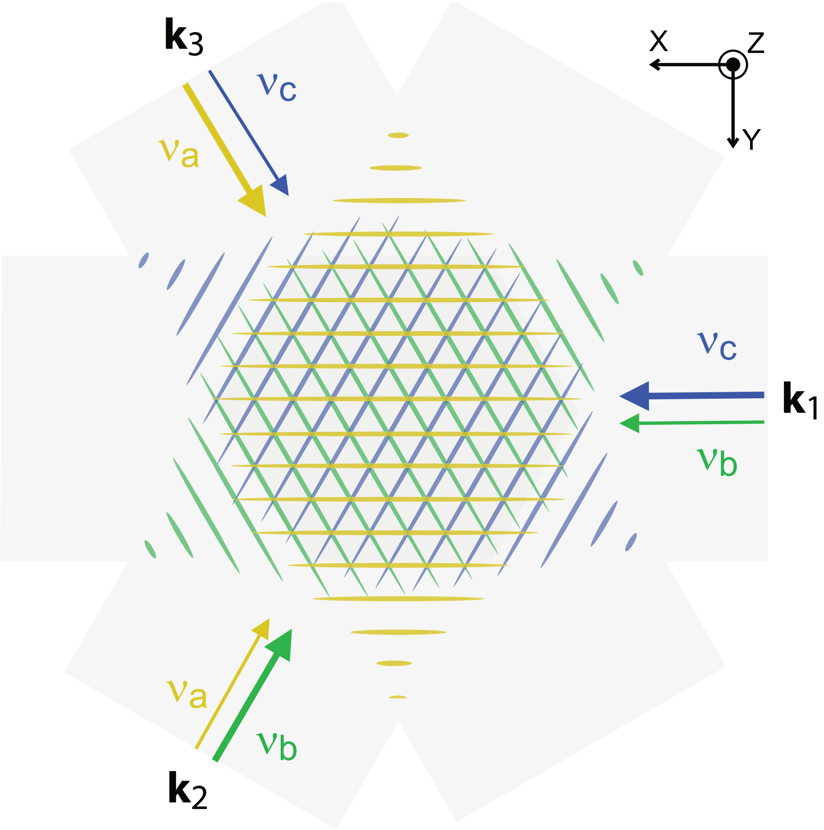

Figure 4.1: Concept of the multi-frequency lattice - Three laser beams with two frequency components each are superimposed under relative angles of 120°. Three 1D lattices are created via pairwise interference. By controlling the relative phase of the frequency pairs, the corresponding lattices can be translated and the overall geometry can be tuned. Figure adapted from [19].

Each 2D optical lattice potential that is created by interference of three beams with wavevectors $\boldsymbol{k}_\mathrm{i}$, $(\mathrm{i}=1,2,3)$ can be expressed as a sum of three 1D lattices [19]:

$$V_\mathrm{Pot}(\boldsymbol{r}) = V_0 + 2\sum_{\mathrm{i}=1}^{3} V_\mathrm{i}\cos\left(\boldsymbol{b}_\mathrm{i}\cdot\boldsymbol{r}+\phi_\mathrm{i}\right) \tag{4.1}$$

with an energy offset V_0, the 1D lattice depths V_i, the reciprocal lattice vectors $\boldsymbol{b}_\mathrm{i}$ and the phases of the three lattices ϕ_i. We define the reciprocal lattice vectors as $\boldsymbol{b}_\mathrm{i} = \boldsymbol{k}_\mathrm{i} - \boldsymbol{k}_{\mathrm{i}+1}$ with $\boldsymbol{k}_4 = \boldsymbol{k}_1$. We note that the reciprocal lattice vectors $\boldsymbol{b}_\mathrm{i}$ appear rotated by 90° with respect to the lattice wavevectors $\boldsymbol{k}_\mathrm{i}$ and that $|\boldsymbol{b}_\mathrm{i}| = \sqrt{3}|\boldsymbol{k}_\mathrm{i}|$, where $|\boldsymbol{k}_\mathrm{i}| = 2\pi/\lambda$ with the wavelength λ of the laser light. It can be shown [19] that the three independent phases ϕ_i correspond to two degrees of freedom that define the position of the lattice in 2D space and a third one, that defines the geometry of the potential. The geometry is then defined by a single parameter, the so-called geometry phase ϕ_g:

$$\phi_\mathrm{g} = \sum_{\mathrm{i}=1}^{3}\phi_\mathrm{i}. \tag{4.2}$$

In the case of $V_1 = V_2 = V_3 = V$, varying the geometry phase tunes the lattice geometry between a triangular lattice with lattice spacing $a_{\text{latt}} = 2/3\lambda$ and a honeycomb lattice which is a triangular lattice with two lattice sites per unit cell. Figure 4.2 depicts the potential landscapes for different values of the geometry phase ϕ_g. For $\phi_\text{g} = 0.5$ the resulting potential landscape is a triangular lattice where the potential barrier height between two adjacent lattice sites is $8/9$ of the total depth. $\phi_\text{g} = 0$ results in a honeycomb lattice which is an inverted triangular lattice. Hence, the potential barrier height is only $1/9$ of the total depth. We note that for the case of imbalanced 1D lattices the geometry can be tuned even further to realize for example distorted square lattices.

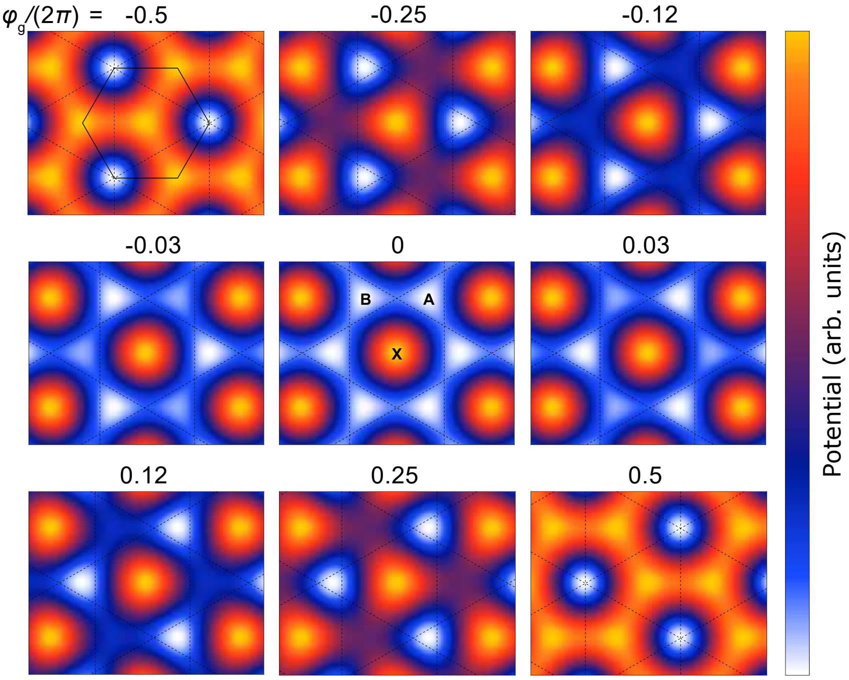

Figure 4.2: Tuning the lattice potential via the geometry phase - We show potential landscapes for nine different values of the geometry phase $\phi_\text{g} = -0.5, -0.25, -0.12, 0, 0.12, 0.25, 0.5$. The black dashed lines denote the positions of the minima for the three 1D lattices. The solid black line in the top left image shows a possible choice for a unit cell. In the central image, the two distinguishible lattice sites per unit cell of the honeycomb lattice are labeled A and B. Figure adapted from [106].

4.2 Implementation

We realize the multi-frequency lattice experimentally with the laser system described in section 3.5. It serves both as the optical dipole trap for evaporation to Bose-Einstein condensation and as our lattice setup. Details on the optical components and the exact beam path can be found in subsection 3.5.1 and figures 3.31 and 3.32, respectively. A simplified cartoon picture of the laser system is shown in figure 4.3a. The laser source is a single-frequency diode pumped solid-state laser[79] at a wavelength of $\lambda = 1064\,$nm with an optical output power of ca. $56\,$W. The light is split into three beam paths and coupled into three fibers labeled L_i $(\text{i} = 1, 2, 3)$, corresponding to the beams with the wavevectors $\boldsymbol{k}_\text{i}$ mentioned above. We use AOMs (A_i) in double-pass configuration to set the relative detunings of the three beams. EOMs (E_i) can be used to modulate frequency sidebands onto each beam individually. Figure 4.3b shows the frequency spectra of the three lattice beams that form the multi-frequency lattice. The three 1D lattices operate at the frequencies ν_a, ν_b and ν_c, separated by the frequency differences ν_α, ν_β and ν_γ respectively. For each frequency ν_a, ν_b and ν_c a carrier of one beam interferes with the sideband from another beam. If the frequency differences are chosen such that the interference patterns from the off-resonant sidebands move faster than the relevant energy-/timescales they only contribute to the potential as an additional harmonic confinement.

---

[79] Coherent: Mephisto MOPA

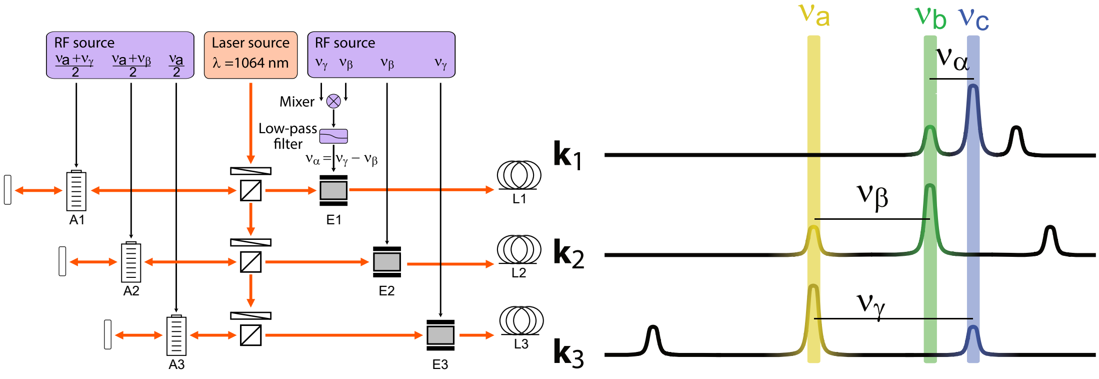

(a) (b)

Figure 4.3: Implementation of the multi-frequency lattice - **(a)** The light is split into three beam paths via $\lambda/2$-waveplates and PBS. Each beam then passes through an AOM (A_i) $(i = 1, 2, 3)$ in double-pass configuration and an EOM (E_i) before they are coupled into fibers L_i. Additional beam-shaping and polarization optics are left out for clarity. The complete optical setup is shown in figure 3.32. **(b)** Cartoon picture of the resulting spectrum for each beam. For each frequency ν_a, ν_b and ν_c, a carrier of one beam coincides with the sideband of another beam. Figure adapted from [19].

Since every 1D lattice comes from the interference of a carrier with a first sideband, the overall lattice depth is reduced as compared to the resonant triangular lattice with three interfering beams. The lattice depth is now proportional to the product $J_0(\eta_\mathrm{i}) \times J_1(\eta_\mathrm{j})$ with the Bessel functions of the first kind $J_{0,1}$ and the modulation indices $\eta_\mathrm{i,j}$ of the corresponding beams. This value is maximized for $\eta_1 = \eta_2 = \eta_3 = \eta \approx 1.08$. We monitor the carrier to sideband ratio for all three beams with a Fabry-Pérot cavity and tune the RF power until this condition is fulfilled. Here, the lattice depth of the triangular lattice is reduced by a factor $J_0(1.08) \times J_1(1.08) \approx 0.34$. For the honeycomb lattice, this factor is only ca. 0.68 since for the conventional honeycomb lattice the polarization would have had to be in-plane and thus reducing the lattice depth to begin with.

The specific choice of the frequencies is a consequence of several aspects. The necessary detunings of the three carriers should be in a range that is accessible with standard AOMs, limiting us to a few tens of MHz detuning between the carriers. At the same time higher order sidebands should contribute to the interference as little as possible. We thus base the frequency differences on multiples of the pair $(2, 7, 9)$. Here the first resonance is between a $+6$th and a $+2$nd order of sidebands. At a modulation index of $\eta \approx 1.08$ the amplitude of the emerging lattice is suppressed by a factor 1×10^{-5} with respect to the main lattice. Finally, the smallest frequency difference shall be much larger than the relevant energy-/timescales in the lattice. For ^{7}Li atoms in a lattice with wavelength $\lambda = 1064\,\mathrm{nm}$, the kinetic energy scale is given by the recoil energy $E_\mathrm{rec}/h = 25.18\,\mathrm{kHz}$. Combining all these requirements we ended up with the somewhat arbitrary choice of

$$\begin{aligned} \nu_\mathrm{a} &= 162.22\,\mathrm{MHz}, & \nu_\alpha &= 2.22\,\mathrm{MHz} \\ \nu_\mathrm{b} &= 160.00\,\mathrm{MHz}, & \nu_\beta &= 7.77\,\mathrm{MHz} \\ \nu_\mathrm{c} &= 152.23\,\mathrm{MHz}, & \nu_\gamma &= 9.99\,\mathrm{MHz}, \end{aligned} \tag{4.3}$$

where ν_a, ν_b and ν_c denote the frequency offset from the laser source. Particularly, we chose these frequencies because they were already successfully implemented in [19] and we already had purchased the matching EOMs months prior.

We now discuss the stability of the geometry, which is directly dependent on the stability of the geometry phase. EOMs have a resonant circuit that is precisely matched to the resonance frequency. If this resonance is slightly altered for example due to thermal drifts, this would result in a change in the phase of the frequency sidebands. We thus thermally stabilize the EOMs via a feedback loop and a Peltier element. From figure 4.3b we can directly see that the time derivatives of the phases ϕ_i of the three 1D lattices are given by:

$$\begin{aligned}\partial_t\phi_1 &= (\nu_\mathrm{c} - \nu_\alpha) - \nu_\mathrm{b}\\ \partial_t\phi_2 &= (\nu_\mathrm{b} - \nu_\beta) - \nu_\mathrm{a}\\ \partial_t\phi_2 &= (\nu_\mathrm{a} - \nu_\gamma) - \nu_\mathrm{c}.\end{aligned} \tag{4.4}$$

As a consequence, the time dependence of the geometry phase is given as

$$\partial_t\phi_\mathrm{g} = \sum_{\mathrm{i}=1}^{3}\phi_\mathrm{i} = \nu_\gamma - \nu_\alpha - \nu_\beta. \tag{4.5}$$

Thus ϕ_g is constant as long as

$$\nu_\alpha = \nu_\gamma - \nu_\beta. \tag{4.6}$$

This is a crucial requirement for a stable geometry phase. To ensure that this condition is fulfilled, we derive all the RF signals for the EOMs from the same digital RF source with four channels that was developed in our group [88, 57]. Since this digital source has a finite frequency/phase resolution and bit depth, we cannot simply set three of the outputs to 2.22 MHz, 7.77 MHz and 9.99 MHz. Instead we subtract the two larger frequencies ν_β and ν_γ with a mixer[80] to create the smaller one ν_α. A low-pass filter[81] is used to suppress the addition of the two frequencies. The three frequencies are then fed through a voltage variable attenuator (VVA)[82] that we use to control the RF power. The RF signals are then amplified via a pre-amplifier[83] and a high-power amplifier[84] before they are coupled to the EOMs. The finite frequency/phase resolution of the RF source also causes a phase drift between the AOMs. However here, the resulting phase drift acts on two 1D lattices at the same time but with different signs. Consequently, the geometry stays constant while only the translation of the lattice is affected.

4.3 | Calibration of the Geometry Phase

Though the three radio frequencies for generating the sidebands originate from the same device, the RF signals may still have an unknown phase delay ϕ_offset caused by the electronics. It is hence necessary to calibrate the geometry phase ϕ_g for given EOM phases $\phi_\mathrm{a,b,c}$ that we set in the experiment control. We expect a simple linear dependence of the form:

$$\phi_\mathrm{g} = \phi_\mathrm{a} + \phi_\mathrm{b} - \phi_\mathrm{c} + \phi_\mathrm{offset}, \tag{4.7}$$

---

[80] Mini Circuits: ZFM-2+
[81] Mini Circuits: BLP-2.5+
[82] Mini Circuits: ZX73-2500-S+
[83] Mini Circuits: ZFL-500LN
[84] Mini Circuits: ZHL-1A-S+

where ϕ_c enters with a different sign, because here a sideband of opposite sign is used. To get a first estimate of the geometry phase we try to replicate the measurement of the staggered flux in momentum space from [19]. In the momentum space interpretation of the multi-frequency lattice, one can define a triangular momentum space lattice that is spanned by the reciprocal lattice vectors [107, 108]. Tunneling between the sites of this lattice corresponds to Bragg reflections. In the momentum space picture the atoms then acquire the phase of the relative 1D lattice ϕ_i when tunneling along a lattice vector $\boldsymbol{b}_i$. A visualization of the triangular momentum space lattice is shown in figure 4.4. The staggered flux through the triangular plaquettes of the momentum space lattice is then given by [19]:

$$\Phi = \sum_{i=1}^{3} (\pi + \phi_i) = \pi + \phi_g. \tag{4.8}$$

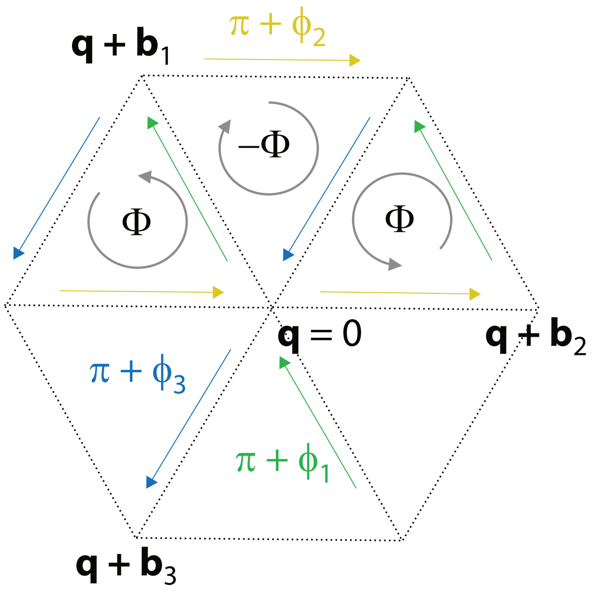

Figure 4.4: Visualization of the staggered flux in the momentum lattice - When tunneling around a plaquette of the triangular momentum lattice, a particle acquires the phase Φ which is solely determined by the geometry phase ϕ_g. Figure taken from [19].

We experimentally realise a quantum walk in the momentum space via Kapitza-Dirac scattering. We first detune the three beams such that the carriers and the sidebands are all off-resonant to each other. The lattice beams thus only act as a harmonic trap for the atoms. We then set the optical power to a certain value with a feedback loop on the RF power on the AOMs. To initiate the quantum walk, we then switch the detunings of the beams to re-establish the interference of the three 1D lattices. We keep the lattices on for a short time (typically a few µs) such that real space movement of the atoms is negligible. We then shut off the laser beams via the AOMs. After a free expansion time, we take absorption images and measure the population in the momentum modes of interest. We define regions of interest around the six 1st order peaks (see the inlets in figure 4.5) and average the population of the related momenta which we label p_a and p_b. We then define the imbalance I as

$$I = \frac{p_a - p_b}{p_a + p_b}. \tag{4.9}$$

We repeat this measurement while varying the phase ϕ_c, so the phase of the RF signal ν_γ that is coupled onto EOM L_3. From equation 4.7 we expect to linearly tune the geometry phase ϕ_g in this manner. The result of this measurement is shown in figure 4.5.

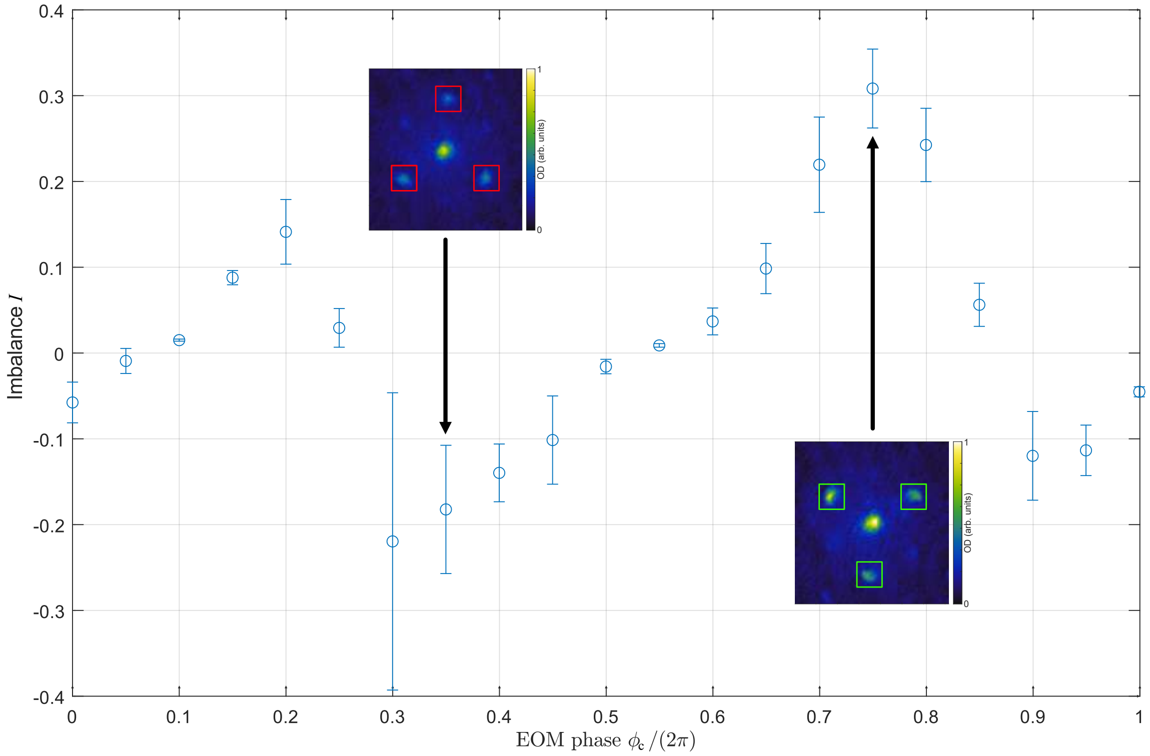

Figure 4.5: Calibration of the geometry phase - We plot the imbalance between the first order peak populations along and opposite to the reciprocal lattice vectors as a function of the phase ϕ_c.

As an effect of the staggered flux, we would expect a breaking of inversion symmetry for all geometry phases except for the cases of the triangular and honeycomb lattices [19]. For the triangular lattice ($\phi_\mathrm{g}/(2\pi) = 0.5$) the staggered flux (see equation 4.8) is $\Phi = 0$ and for the honeycomb lattice ($\phi_\mathrm{g}/(2\pi) = 0$) it is $\Phi = \pi = -\pi$. In between this zero-crossings of the imbalance we expect a sinusoidal curve [19]. However our data don't match these expectations. We identify two phases where the imbalance is clearly zero at $\phi_\mathrm{c}/(2\pi) = 0.05$ and $\phi_\mathrm{c}/(2\pi) = 0.55$. These could correspond to the triangular and the honeycomb lattice, however we cannot explain the other two zero-crossings around $\phi_\mathrm{c}/(2\pi) = 0.25$ and $\phi_\mathrm{c}/(2\pi) = 0.85$. Thus this measurement is inconclusive and we need a different approach to calibrate the geometry phase.

A different approach to calibrate the geometry phase that is discussed in [19], is to use the technique of quantum gas magnifying [18] (also called matter-wave microscopy in this thesis) to study the imbalances between the A and B sites close to the honeycomb lattice in real space. We implement the matter-wave lens via the same laser system that we use for the optical lattice and the evaporation to BEC. By letting the system evolve in a harmonic trap for a quarter period, followed by a free expansion, we magnify the system before taking absorption images. We can thus image the magnified real space density distribution in the lattice with single lattice-site resolution. More details on this can be found in chapter 5. When loading the lattice with a set phase of $\phi_\mathrm{c}/(2\pi) = 0.05$ we are able to obtain images of a triangular lattice distribution as is displayed in figure 4.6a. When going to the phase of $\phi_\mathrm{c}/(2\pi) = 0.55$, we completely lose the atomic signal. We attribute this to issues with our intensity lock at that time. Since the bandgap in the honeycomb lattice is smaller than in the triangular lattice, low-frequency noise during the adiabatic loading of the lattice may introduce strong parametric heating. Though this is a further indication that $\phi_\mathrm{c}/(2\pi) = 0.05$ might correspond to a geometry phase of $\phi_\mathrm{g}/(2\pi) = 0.5$ (i.e. a triangular lattice), this is still not conclusive. As will be further discussed in section 5.4, for coherent states in optical lattices so-called Talbot copies of the density distribution emerge during the matter-wave protocol. When varying the evolution time in the harmonic trap, these copies of the original lattice structure are separated by the so-called Talbot time T_{Talbot}, which is given by the recoil energy of the lattice. In our case, this time is on the order of $13\,\mu\mathrm{s}$ and it is thus experimentally difficult to distinguish between the original image and Talbot copies. In between such copies, the density distribution might be completely inverted and it is thus not possible to obtain the geometry phase from these images. An example of such an inverted density distribution is shown in figure 4.6b. Here, we prepared a resonant triangular lattice without using the sidebands of the EOMs. When imaging in between two Talbot copies, the resulting density distribution resembles that of a honeycomb lattice which is an inverted triangular lattice. The effects of the Talbot copies can be avoided by freezing out the coherence before the imaging protocol [18]. However at the time of taking these data, we could not increase the lattice depth enough without heating and significant atom loss due to the above mentioned issues with the intensity lock.

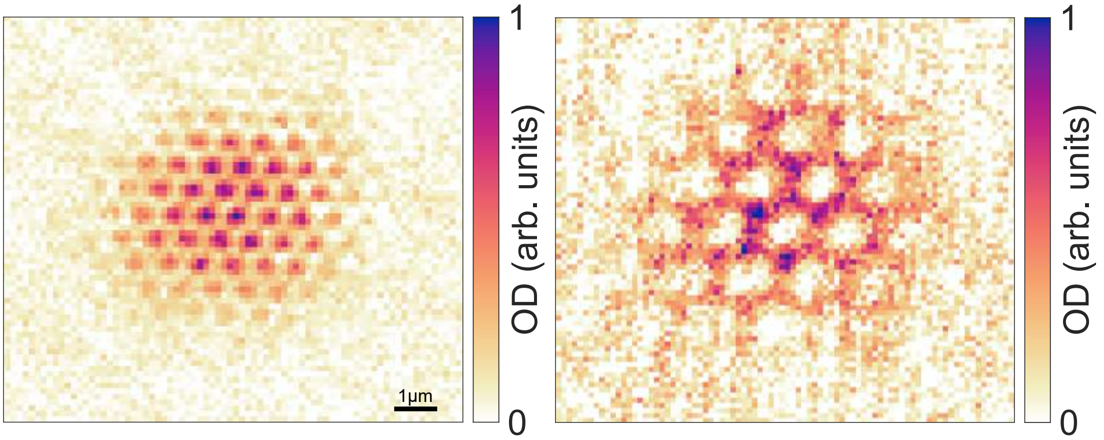

(a) (b)

Figure 4.6: Images of the density distribution of the atoms in the lattice obtained via matter-wave microscopy - **(a)** 1.4×10^4 atoms in a multi-frequency lattice with $\phi_c/(2\pi) = 0.05$. At this phase we get the optimum signal whereas the atomic signal vanishes at $\phi_c/(2\pi) = 5.05$. We attribute this atom loss to heating effects in the honeycomb lattice. **(b)** Matter-wave microscopy of a resonant triangular lattice in between two Talbot copies. The density profile is inverted and resembles that of a honeycomb lattice.

While working on this matter-wave microscopy we noticed that at certain parameter sets, we could observe a lattice structure even for off-resonant laser beams. Figure 4.7 shows such an image where the beams L_1 and L_2 are detuned by $1\,\mathrm{MHz}$ while the beam L_3 is detuned by $14\,\mathrm{MHz}$. The observed lattice structure appears to have the same spatial periodicity as the corresponding resonant lattices. Since the detuning is much larger than the kinetic energy scale of the moving lattices $E_{\mathrm{rec}} = (\hbar^2 k^2)/(2m) = h \times 25.18\,\mathrm{kHz}$, we would naively expect no density modulation. Upon more thorough consideration, we need to compare the detuning to the on-site trap frequency ω_{site} in the moving 1D lattice at a given lattice depth V_0. It is given as $\hbar\omega_{\mathrm{site}} = \sqrt{2(V_0/E_{\mathrm{rec,latt}})} \cdot E_{\mathrm{rec,latt}}$, where we introduced $E_{\mathrm{rec,latt}} = (\hbar^2 b^2)/(2m) = h \times 75.53\,\mathrm{kHz}$ as the recoil energy with respect to the reciprocal lattice vector $b = \sqrt{3} \cdot 2\pi/\lambda$. At typical lattice depths of only a few $E_{\mathrm{rec,latt}}$ this frequency should still be negligible compared to the detuning of the beams. Additionally, if the atoms were affected by the moving lattice, we would expect to observe heating and atom loss instead of a static density pattern. We observe this effect for detunings of up to $4\,\mathrm{MHz}$ in all three combinations of beams and for small detunings even in two combinations at the same time. We find that the threshold optical power above which this effect occurs depends on the detuning. For $1\,\mathrm{MHz}$ detuning the threshold is at $50\,$mW per beam and it increases non-linear to $400\,$mW per beam at a detuning of $4\,$MHz.

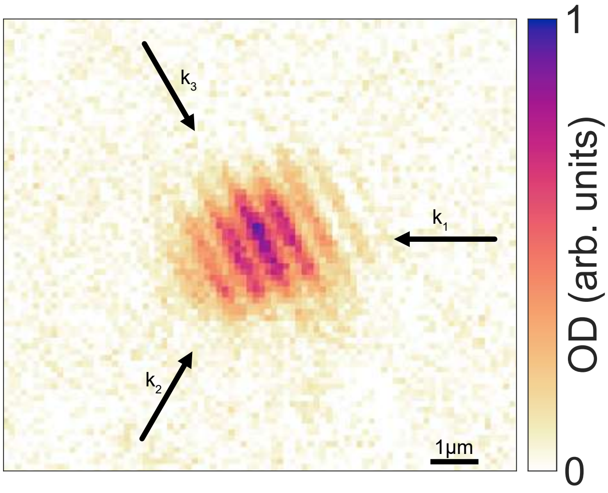

Figure 4.7: 1D lattice structure from off-resonant beams - In-situ image of the density distribution of 1.4×10^4 atoms in a harmonic trap consisting of three detuned laser beams magnified via matter-wave microscopy. The beams L_1 and L_2 are detuned by $1\,$MHz while L_3 is detuned by $14\,$MHz with respect to L_2.

So far we have not understood the origin of these observations. We think it might be related to the spontaneous crystallization in Bose-Einstein condensates discussed in [109, 50]. Though the lattice beams are much further red-detuned as in those publications, the intensities are also much higher such that we reach a comparable regime.

These additional lattices appear in certain parameter regimes even when a 2D multi-frequency lattice is present. Repeating the same experimental sequence can lead to vast differences in the observed geometry, indicating that the phases of the additional lattices are random. However, this effect may also be caused by an overall unstable geometry that for example may be the result of thermal drifts in the EOMs. Since we cannot distinguish these processes, it is not possible to reliably operate the multi-frequency lattice as long as these additional lattice structures are present. We think that these additional lattices also might contribute to the measurement of the staggered flux and could explain the deviations of our data from the expectations. To solve this, we decided to change the base frequency differences of the three 1D lattices to larger values. We propose new frequencies of

$$\begin{aligned} \nu'_{\mathrm{a}} &= 182.5\,\mathrm{MHz}, \qquad & \nu'_{\alpha} &= 10\,\mathrm{MHz} \\ \nu'_{\mathrm{b}} &= 172.5\,\mathrm{MHz}, \qquad & \nu'_{\beta} &= 35\,\mathrm{MHz} \\ \nu'_{\mathrm{c}} &= 137.5\,\mathrm{MHz}, \qquad & \nu'_{\gamma} &= 45\,\mathrm{MHz}. \end{aligned} \tag{4.10}$$

With this choice we can still use the same AOMs and we can re-use the $9.99\,$MHz EOM. We have ordered and installed the corresponding EOMs at $35\,$MHz and $45\,$MHz. However as of writing this thesis we have not yet tested the multi-frequency approach again. Instead we work with resonant triangular lattices and use the EOMs to help adiabatically loading into the lattice at a given harmonic confinement.

4.4 | Outlook

Considering further investigation of the lattice structures that emerge from off-resonant lattice beams, we could rule out the influence of the running standing waves by rotating the polarization in one of the beams to in-plane polarization. Additionally, we could prepare resonant triangular lattices and only turn on one of the EOMs to create a single off-resonant beam. Via matter-wave microscopy we could then check if the phase of these density patterns is truly random. Having exchanged the EOMs in the laser system, the next step is the calibration of the geometry phase. Once we can reliably tune the geometry of the lattice, there are several interesting topics that we could study. As shown in [19] it is possible to use the multi-frequency lattice for excitations to higher Bloch bands. Recently, the realization of a chiral superfluid in a 2nd Bloch band of a boron-nitride optical lattice has been reported [100]. In real-space the corresponding orbital shows a vortex that could be imaged directly via matter-wave microscopy. Furthermore, the dynamic tunability of the geometry could be implemented in novel Floquet-schemes by combining it with the well established techniques of lattice-shaking [110, 105] and amplitude modulation [111]. Lastly, a quench of the lattice geometry could be applied to state tomography measurements [112, 105, 113]. Preliminary measurements of a static system were performed in [106]. It would be interesting to expand this data set to different interaction strengths using the broad Feshbach resonances of ^{7}Li.

CHAPTER 5

Matter-Wave Microscopy of ^{7}Li

Ultracold atoms in optical lattices are a prolific model system to study complex quantum mechanical processes. The advent of quantum gas microscopes [15, 16], which combine single site resolution of optical lattices with single atom sensitivity, has lead to the observation of a vast number of phenomena [17]. Yet, they are technically complex, requiring high resolution imaging techniques, cooling of the atoms in high power pinning lattices and computer algorithms to reconstruct the atomic distribution. Additionally, quantum gas microscopes suffer from parity projections due to light-assisted collisions and, with the exception of [114, 115], are limited to 2D systems because the high-resolution objectives narrow the depth of focus. This issue can be overcome by other alternative approaches such as electron [116] or ion [117] microscopy, but at the cost of low single atom detection fidelity. We also mention super-resolution microscopes [118, 119] that can even access sub-lattice density information but require scanning techniques to do so. All these methods have in common that they try to increase the spatial resolution of the measurement apparatus. A complementary approach was experimentally demonstrated in [18]; related ideas were proposed in [120, 121]. Instead of increasing the resolution of the measurement, one can first magnify the system of interest via matter-wave optics before applying standard absorption imaging techniques. This enables single shot measurements of the column density of 3D systems with sub-lattice resolution.

During this thesis, we adapted this technique to build a matter-wave microscope with an optical matter-wave lens. As an advancement of the technique presented in [18], where a magnetic trap was used for the harmonic confinement, this allows a spin-independent magnification of the system and thus we can use the broad Feshbach resonance of ^{7}Li to tune the interactions, which have a crucial influence on the technique [18]. The concept is based on matter-wave optics in the time domain. It is illustrated in figure 5.1. Starting with atoms in a 2D optical lattice of tubes, we project the density distribution onto a harmonic potential with trapping frequency $\omega = 2\pi/T$, in our case realized by three non-interfering red-detuned laser beams intersecting under $120°$. We use a $T/4$ evolution in this harmonic trap to perform a Fourier transform between the momentum distribution and the spatial distribution [122–126] and follow this with a time of free expansion t_{tof}. This time of flight acts as a second Fourier transform and thus the initial spatial distribution is reproduced with a magnification $M \approx \omega t_{\mathrm{tof}}$.

We start this chapter with a theoretical description of the matter-wave protocol and the derivation of the focusing condition. We then discuss deviations from this condition, before presenting our implementation of the technique. We end with the demonstration of a coherence measurement with single-site resolution. This technique was experimentally implemented and the data were taken together with Justus Brüggenjürgen under the supervision of Christof Weitenberg.

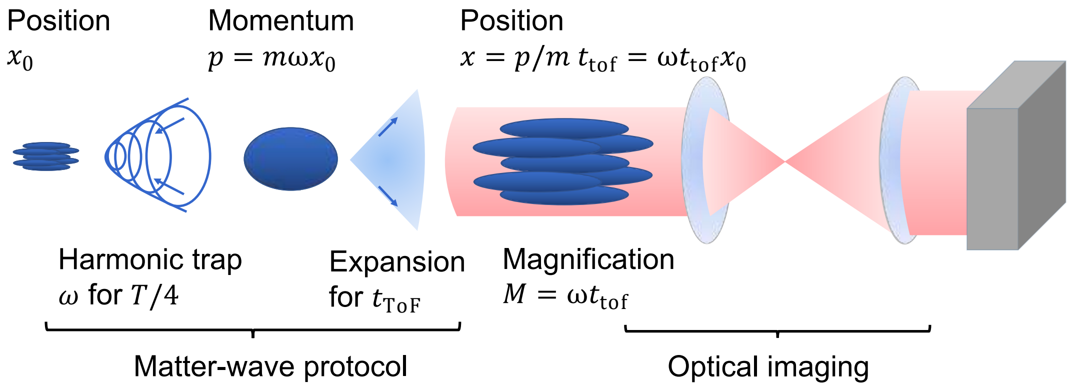

Figure 5.1: Working principle of the matter-wave microscope - The density distribution of ultracold atoms in an optical lattice is magnified using matter-wave optics, consisting of a pulsed evolution time in a harmonic trap and a free expansion. With standard absorption imaging we can then image the magnified density distribution with singe lattice-site resolution. Figure adapted from [18].

5.1 | Theoretical Description of the Matter-Wave Lens

The basic idea of the matter-wave microscopy comes from the fact that both free expansions in time of flight, as well as the evolution in a harmonic trap result in Fourier transformations between real space and momentum space. Starting from an initial real space density distribution, two of these transformations can be combined to end up back in the real space but with a magnification that may differ from one. In a simple classical picture we can easily understand this concept by imagining a particle at rest that is displaced by a distance x_0 from the center of a harmonic potential with angular frequency ω. After a quarter period in this potential, the particle will be located at the trap center and all its potential energy will have been transferred to kinetic energy with a velocity $v = -\omega x_0$. When switching off the harmonic potential, the particle then continues to move with this velocity. After a given time of flight t_{tof} the particle's new position is then given as $x' = -\omega x_0 t_{\text{tof}}$. Thus the position of the particle after this protocol is magnified by the product $M = -\omega t_{\text{tof}}$.

In real applications, the initial momenta of the particles in the system will not be zero. We thus need to derive a focusing condition which takes into account the admixture of initial momenta to the final position. In the following we will derive this focusing condition for quantum-mechanical position and momentum operators in the Heisenberg picture. We note that equivalent considerations can be made in the Schrödinger picture describing the evolution of quantum field operators. This directly shows that the matter-wave optics also reproduces the correlations [127]. Here, we focus on 1D systems, however the derivation of the focusing condition can easily be generalized to 2D or 3D systems under the assumption that $\omega_x = \omega_y = \omega_z$. We start with the 1D Hamiltonian of a particle with mass m in a harmonic oscillator with angular frequency ω which is given as:

$$\hat{H}_{\text{ho}} = \frac{\hat{p}^2}{2m} + \frac{m\omega\hat{x}^2}{2}, \tag{5.1}$$

with the position operator $\hat{x}$ and the momentum operator $\hat{p}$. The equations of motions for this Hamiltonian are

$$\partial_t \hat{x} = \frac{i}{\hbar}\left[\hat{H}_{\text{ho}}, \hat{x}\right] = \frac{\hat{p}}{m} \tag{5.2}$$

$$\partial_t \hat{p} = \frac{i}{\hbar}\left[\hat{H}_{\text{ho}}, \hat{p}\right] = -m\omega^2\hat{x}. \tag{5.3}$$

For an evolution time t_{ho} in the harmonic oscillator, these equations of motion are solved by

$$\begin{aligned}\hat{x}(t_{\text{ho}}) &= \hat{x}(0)\cos(\omega t_{\text{ho}}) + \frac{\hat{p}(0)}{m\omega}\sin(\omega t_{\text{ho}}) &(5.4)\\ \hat{p}(t_{\text{ho}}) &= \hat{p}(0)\cos(\omega t_{\text{ho}}) - m\omega\hat{x}(0)\sin(\omega t_{\text{ho}}), &(5.5)\end{aligned}$$

with the initial position and momentum operators $\hat{x}(0)$ and $\hat{p}(0)$. After the time t_{ho} the harmonic potential is shut off and the atoms can freely expand for a time of flight t_{tof}, during which the momenta remain fixed. The position operator then becomes

$$\begin{aligned}\hat{x}(t_{\text{ho}} + t_{\text{tof}}) &= \hat{x}(t_{\text{ho}}) + t_{\text{tof}}\frac{\hat{p}(t_{\text{ho}})}{m}\\ &= \hat{x}(0)\left(\cos(\omega t_{\text{ho}}) - t_{\text{tof}}\omega\sin(\omega t_{\text{ho}})\right)\\ &+ \hat{p}(0)\left(\frac{1}{m\omega}\sin(\omega t_{\text{ho}}) + \frac{t_{\text{tof}}}{m}\cos(\omega t_{\text{ho}})\right).\end{aligned} \tag{5.6}$$

The focusing condition is now met when the contribution of the initial momentum $\hat{p}(0)$ vanishes. This is the case when

$$\tan(\omega t_{\text{ho}}) = -\omega t_{\text{tof}}. \tag{5.7}$$

We can then write the resulting position operator as

$$\begin{aligned}\hat{x}(t_{\text{ho}} + t_{\text{tof}}) &= \hat{x}(0)[\cos(\omega t_{\text{ho}}) + \tan(\omega t_{\text{ho}})\sin(\omega t_{\text{ho}})]\\ &= \hat{x}(0)\frac{1}{\cos(\omega t_{\text{ho}})} = \hat{x}(0)\frac{1}{\cos[\arctan(\omega t_{\text{tof}})]}\\ &= \hat{x}(0)\sqrt{1 + (\omega t_{\text{tof}})^2}.\end{aligned} \tag{5.8}$$

The initial density distribution is thus magnified by the factor $M = \sqrt{1 + (\omega t_{\text{tof}})^2}$. For the case off $\omega t_{\text{tof}} \gg 1$, this simplifies to $M = \omega t_{\text{tof}}$. Figure 5.2 shows a graphical visualization of the focusing condition. We decompose the position operator into its two components $\hat{x}(0)$ and $\hat{p}(0)$ with time-dependent coefficients $c_x(t)$ and $c_p(t)$ such that $\hat{x}(t) = c_x(t)\hat{x}(0) + c_p(t)\hat{p}(0)$. In the coordinate space of this coefficients, the evolution in the harmonic trap starting at point $A = (c_x, c_p) = (1, 0)$ corresponds to a rotation around $O = (c_x, c_p) = (0, 0)$ with an angle given by ωt_{ho}. Upon reaching point B, we initiate the free expansion which is represented by a straight line since during the time of flight $\hat{p} = \partial_t\hat{x} = \text{const.}$. The length of this straight line is given by ωt_{tof}. The focusing condition is again met when $c_p(t) = 0$ at point C. This is realized when the angle θ_{tof} satisfies the condition $\theta_{\text{tof}} = \arctan(\omega t_{\text{tof}}) = -\omega t_{\text{ho}} + n\pi$, where n is an integer. The magnification M is then given as the hypotenuse of the triangle OBC as $M = \sqrt{(1)^2 + (\omega t_{\text{tof}})^2}$. As illustrated in the figure, this magnification protocol leads to a parity reflection for every second odd multiple of $T/4$. However since this is not important for us, we always refer to the magnification as $|M|$.

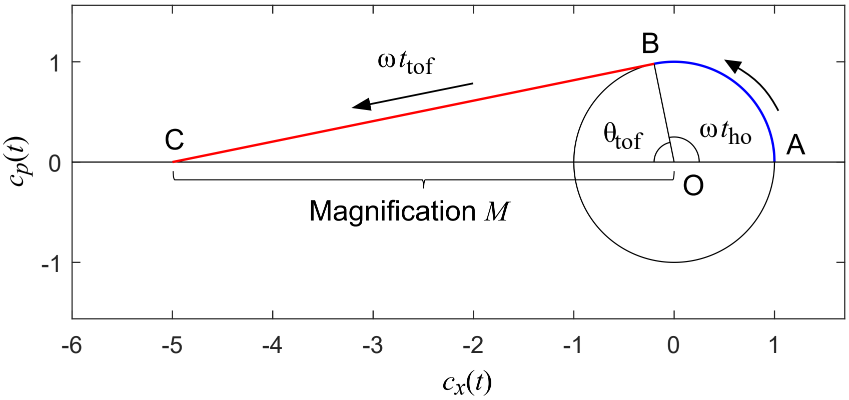

Figure 5.2: Graphical illustration of the focusing condition - We decompose the position operator $\hat{x}(t)$ into the two time-dependent coefficients $c_x(t)$ and $c_p(t)$ and show the trajectory in this coordinate space during the matter-wave protocol. Starting at point A the harmonic trap causes a rotation around the origin O with the angle ωt_{ho} to the point B. When initiating the free expansion, the momentum remains constant resulting in a propagation as a straight line of length ωt_{tof}. The focusing condition is met at point C where $c_p(t) = 0$. This is the case when $\theta_{\mathrm{tof}} = \arctan(\omega t_{\mathrm{tof}}) = -\omega t_{\mathrm{ho}} + n\pi$, where $n \in \mathbb{Z}$. The magnification is then given as the length of the line $\overline{OC}$ as $M = \sqrt{1 + (\omega t_{\mathrm{tof}})^2}$. Figure taken from [127].

It can be shown, that a focusing condition can always be obtained even if the harmonic trap is not turned on and off instantly but also for time-varying harmonic confinements [127, 128]. However in these cases, the magnification may deviate from the simple expression derived above. This is crucial, since experimentally the harmonic traps will always be shut on or off within a finite time. We also note, that one could replace the free expansion with an evolution in a second harmonic trap with different trap frequency ω_2 [128]. With ω_1 being the trap frequency of the first harmonic trap, the magnification would then be given by $M = \omega_1/\omega_2$. Alternating between the two traps for n times would thus lead to a magnification of $M = (\omega_1/\omega_2)^n$. In real-life experiments this is limited by the finite size of harmonic traps. Once the particles start to probe the anharmonic parts of the trap, this framework starts to fail and aberrations occur.

5.2 | Deviations from the Focusing Condition

In the following, we discuss how experimental inaccuracies affect the matter-wave microscope. We first consider the case of a small variation of the harmonic evolution time. It can be shown [128] that for small deviations from the focusing conditions in the harmonic trap $t_{\mathrm{ho}} \mapsto t_{\mathrm{ho}} + \delta t$, the position operator becomes:

$$\hat{x}(t_{\mathrm{tof}} + (t_{\mathrm{ho}} + \delta t)) \sim -M \left[\hat{x}(0) + \frac{\delta t}{m}\hat{p}(0)\right] \tag{5.9}$$

which is, up to a factor $-M$, identical to the expression for the position operator after a short time of flight δt:

$$\hat{x}(t_{\mathrm{tof}} = \delta t)) \sim \left[\hat{x}(0) + \frac{\delta t}{m}\hat{p}(0)\right]. \tag{5.10}$$

Hence, an inaccuracy in the harmonic evolution time can be directly mapped to the diffusion of the initial density distribution at a corresponding time of flight. We use the Rayleigh criterion to find the maximum spread σ_{site} of a single lattice sites' density distribution that still allows to distinguish two individual lattice sites and find that $\sigma_{\mathrm{site}} < 0.35 a_{\mathrm{latt}}$. This sets a limit to a maximum time deviation δt that depends on the initial density distribution of the Wannier functions. We consider a triangular lattice with a lattice spacing of $a_{\mathrm{latt}} = 709\,\mathrm{nm}$ and depth of $6E_{\mathrm{rec}}$ and find that $\delta t_{\mathrm{max}} = 4\,\mathrm{\mu s}$. This is just within the resolution of our experiment which is set by the *ADwin Pro II* system to $1\,\mathrm{\mu s}$. We note that this also sets the condition for the maximum eccentricity of a 2D harmonic trap which is given as $|T_x/4 - T_y/4| < 2\delta t_{\mathrm{max}}$.

Next, we consider analogously small variations of the time of flight. This is of real experimental relevance, because we work with imaging pulses of finite duration t_{image}, thus essentially probing different times of flight at the start and the end of the pulse. We thus study the case of $t_{\mathrm{tof}} \mapsto t_{\mathrm{tof}} + t_{\mathrm{image}}$. Again, this can be mapped to a direct time of flight from the lattice but with a rescaled δt [128]

$$\hat{x}((t_{\mathrm{tof}} + t_{\mathrm{image}})) + t_{\mathrm{ho}}) \propto \hat{x}(\delta t) \tag{5.11}$$

$$\delta t \sim \frac{t_{\mathrm{image}}}{(\omega t_{\mathrm{tof}})^2}. \tag{5.12}$$

With Lithium atoms, one typically works with imaging pulses of duration $t_{\mathrm{image}} \leq 10\,\mathrm{\mu s}$ [129]. With typical magnifications of $M > 20$ this is completely negligible. Instead, the time of flight mainly affects the magnification M as can be seen by taking the derivative of the position operator at the end of the matter-wave protocol with respect to t_{tof}:

$$\partial_{t_{\mathrm{tof}}}\hat{x}(t_{\mathrm{tof}} + t_{\mathrm{ho}}) = \partial_{t_{\mathrm{tof}}}\hat{x}(0)\sqrt{1 + (\omega t_{\mathrm{tof}})^2} = \frac{\omega^2 t_{\mathrm{tof}}}{\sqrt{1 + (\omega t_{\mathrm{tof}})^2}}\hat{x}(0) \overset{\omega t_{\mathrm{tof}} \gg 1}{\approx} \omega\hat{x}(0). \tag{5.13}$$

We now consider atoms that are initially displaced by a distance x_0 from the trap center. Substituting the position operator $\hat{x}(0)$ from above with x_0, we see that during the imaging pulse, the atoms travel the distance $\delta x = t_{\mathrm{image}}\omega x_0$. Requiring again $\delta x < 0.35\,a_{\mathrm{latt}}$, to make sure that the signal from two lattice sites doesn't overlap, we can define a maximum initial displacement x_{max} from the trap center. Taking into account the magnification at the end of the matter-wave protocol we get

$$x_{\mathrm{max}} = \frac{0.35\,a_{\mathrm{latt}}M}{\omega t_{\mathrm{image}}} = 0.35\,a_{\mathrm{latt}}\frac{t_{\mathrm{tof}}}{t_{\mathrm{image}}}. \tag{5.14}$$

For typical parameters of $t_{\mathrm{tof}} = 3.5\,\mathrm{ms}$ and $t_{\mathrm{image}} = 10\,\mathrm{\mu s}$ we find a maximum system size of ca. 250 lattice sites in diameter that can be magnified. Due to the strong harmonic confinement in our lattice, we typically prepare lattices with only ca. 10 lattice sites in diameter.

Lastly, we want to discuss the optical Talbot effect. As coherent light with wavelength λ_{L} is diffracted from a periodic lattice structure with lattice constant a_{latt}, the image of this lattice is repeated at regular distances z_{Talbot} given by:

$$z_{\mathrm{Talbot}} = \frac{2a_{\mathrm{latt}}^2}{\lambda_{\mathrm{L}}}. \tag{5.15}$$

Typically in optical lattice experiments with ultracold atoms, both the lattice constants and the wavelengths used for imaging are on the order of $a_{\mathrm{latt}} \sim \lambda_{\mathrm{L}} \lesssim 1\,\mathrm{\mu m}$. At these length scales the Talbot length z_{Talbot} is also in a comparable regime and the Talbot effect can thus typically not be resolved due to the finite depth of focus. However when the lattice constant is enlarged before the absorption images are taken, this effect may play an important role [130]. We typically work with trap frequencies of $\omega \approx 2\pi \times 1\,\mathrm{kHz}$ and time of flights of $t_{\mathrm{tof}} \approx 3.5\,\mathrm{ms}$ resulting in a magnifications of $M \approx 22$. At these settings, the lattice constant in the triangular lattice is magnified to ca. $a_{\mathrm{latt,magnified}} = 15.6\,\mu\mathrm{m}$. We then perform absorption imaging at a wavelength of $\lambda_{\mathrm{L}} = 671\,\mathrm{nm}$. This results in a Talbot length of $z_{\mathrm{Talbot}} = 725\,\mu\mathrm{m}$. We then use an optical magnification of $M_{\mathrm{optical}} = 2.14$ to focus the image onto our camera. Consequently, the Talbot length is scaled in the imaging plane by a factor M^2_{optical}. We can thus scan through the optical Talbot copies by moving our camera on the mm-scale. Our imaging system is set up along the axis of gravitation. Thus during the free expansion, the atoms fall towards the camera, accelerated by the force of gravity. After $t_{\mathrm{tof}} \approx 3.5\,\mathrm{ms}$ they already fell a distance of ca. $60\,\mu\mathrm{m}$. For longer times of flight, e.g. $t_{\mathrm{tof}} \approx 5\,\mathrm{ms}$ they already traveled twice the distance. It is thus advisable to use a fixed time of flight and only change the harmonic confinement to vary the magnification. Otherwise, one would have to adjust the optical imaging system along with the matter-wave imaging.

5.3 | Implementation

We implement the matter-wave lens via an optical dipole trap. We use the same setup as for the lattice and the evaporation to BEC (see section 3.5.1). The trap consists of three beams at a wavelength $1064\,\mathrm{nm}$ focused to a $1/e^2$ beam waist radius $41\,\mu\mathrm{m}$ intersecting under $120°$. We remove the interference by detuning the beams with respect to each other. We use maximum optical powers of $3.5\,\mathrm{W}$ per beam which corresponds to radial trap frequencies of $\omega_x = \omega_y = \omega_r = 2\pi \times 2.86\,\mathrm{kHz}$ and an axial trap frequency of $\omega_z = 2\pi \times 4.13\,\mathrm{kHz}$. The ratio between in- and out-of-plane trap frequency is ca. $1 : 1.44$. Since we use the same laser system for the lattice and the harmonic trap, we don't need to align them onto each other. However, we still need to make sure that the three beams are well aligned, to achieve a trap that is as isotropic and as harmonic as possible. Here we profit from the three-fold setup, since the harmonic region for an isotropic trap consisting of three beams is larger than for a comparable trap consisting of only two beams overlapped under $90\,°$. We first have to align the axial position of the three foci. We do this by measuring the radial trap frequencies of the single beams $\omega_{r,L_{\mathrm{i}}}$ at the position of their intersection. We prepare a BEC in the intersection point of all three beams and then shut off two of the beams. We purposefully misalign the beams a bit, such that this results in a dipole mode oscillation in the remaining beam. We enhance the signal by following the hold time in the single beam with a short time of flight and measure the displacement as a function of the hold time. An exemplary measurement of the radial frequency of beam L_2 at a power of $450\,\mathrm{mW}$ is shown in figure 5.3. We perform this measurement for all beams and find that the measured trap frequencies don't match. We attribute this to a bad alignment of the longitudinal focus positions. The Rayleigh range for a waist of $41\,\mu\mathrm{m}$ at a wavelength $\lambda = 1064\,\mathrm{nm}$ is $z_{\mathrm{R}} \approx 5\,\mathrm{mm}$. We adjust the position of the final lenses in the corresponding telescopes and repeat this measurement. With this iterative procedure we are able to maximize and equalize the radial trap frequency for all three beams ensuring a good alignment of the longitudinal focus position. The transversal focus position is adjusted in a similar manner. We again induce dipole modes by shutting off two of the three beams and use a time of flight after the hold time in the trap to magnify the oscillation amplitude. At a known radial frequency of the beam we can also obtain direct information about the real displacement in this way. We can use this to adjust the lattice beams onto each other within a deviation of maximum $1\,\mu\mathrm{m}$ (footnote [85]). With this procedure we are able to get a decently isotropic trap for the matter-wave lens. For a precise tuning of the isotropy via the beam balance we use a measurement described in the next section 5.4.

---

[85] The adjustment procedure for all three beams typically takes ca. $30\,\mathrm{min}$-$60\,\mathrm{min}$ and has to be repeated every few weeks due to thermal drifts of the apparatus.

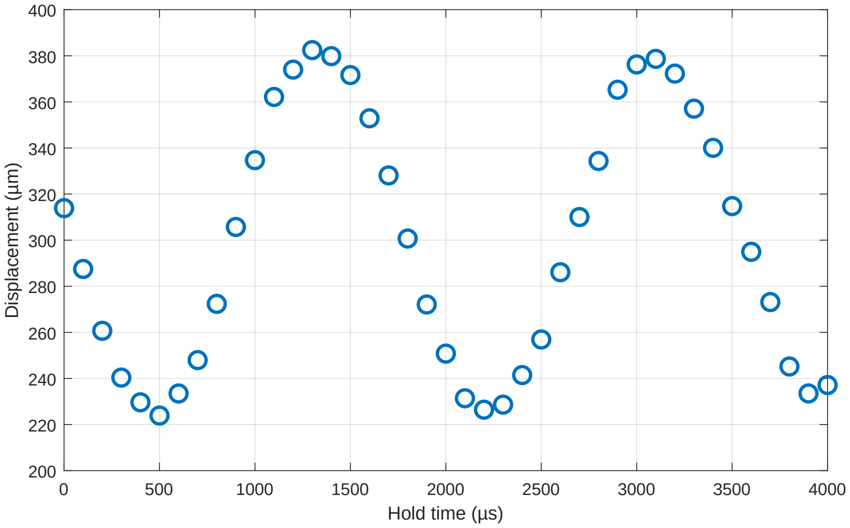

Figure 5.3: Measuring the single beam trap frequencies - For each beam we measure the radial trap frequency for varying optical powers. We purposefully misalign the beam from the BEC center and shut off the other two beams. This initiates a dipole mode oscillation of the atoms in the single beam trap. We vary the hold time in the trap and use a short time of flight of 2.5 ms to magnify the oscillation amplitude. This figure shows the measurement for beam L_2 at a power of 450 mW corresponding to a measured radial trap frequency of $\omega_{r,L_2} = 2\pi \times 567$ Hz.

We initiate the matter-wave protocol by shutting off the lattice and projecting onto the harmonic trap. This is done by changing the detunings from the interfering lattice to the non-interfering dipole trap. To resolve the lattice structure we have to ensure that the Bragg peaks at $\hbar k$ lie still within the harmonic region of the trap after the first Fourier transformation. The position x_k of the momenta at the end of the $T/4$ pulse is given as $x_k = (2\hbar k)/(m\omega)$. We can thus see that this condition is better fulfilled for larger trap frequencies. Consequently, we find that we get the best signals for parameters with more power in the dipole trap than in the lattice. We can achieve this in two different ways. Using an RF switch[86] we can change the RF source for the AOMs. With this, we change the optical power and the frequency of the three beams simultaneously. However the optical power is then not controlled by our intensity lock anymore. We typically work with trap frequencies of ca. $\omega_r \sim 2\pi \times 1$ kHz corresponding to a harmonic evolution time of $t_{\text{ho}} \approx T/4 \sim 250$ µs. As derived in section 5.2, small deviations from that time may not exceed 4 µs. We thus need to make sure that the trap frequency is stable and reproducible on the percent level. Consequently the optical powers need to be stable on the order of ca. $10\,\%$. While this fulfilled on the shot to shot basis, we are not confident in this technique considering potential long-term drifts. We thus alternatively use a scheme where we can rely on our intensity lock. Here we make use of the fact that there always is a focusing condition even for time-dependent harmonic traps as described in section 5.1. We initialize the matter-wave lens by shutting off the lattice via the frequency of the AOMs and then ramp up the beam power to the desired value within 100 µs. We then hold the system for the remainder of the harmonic evolution time. After a time of flight of typically 3.5 ms we take absorption images with an optical magnification of $M_{\text{optical}} = 2.14$.

The concept of the matter-wave lens that we introduced in section 5.1 is only valid for non-interacting particles. Collisions during the matter-wave protocol will inevitably diffuse the obtained image, which was found to be a limiting factor in [18]. This is especially important for imaging of coherent systems as for those at the end of the harmonic evolution the initial momentum distribution is realized in real space leading to high atomic densities at the Bragg peaks of the lattice. We can study the role of the interactions by adjusting the interaction strength with the broad Feshbach resonance of ^{7}Li. We find that it is crucial to shut off the interactions before we initiate the matter-wave protocol. To illustrate this, we compare two images with and without interactions during the matter-wave protocol shown in figure 5.4. For a scattering length of ca. $76\,a_0$ (figure 5.4a) the initial density distribution is washed out while for a scattering length of ca. $1.4\,a_0$ (figure 5.4b) the initial atomic density distribution is obtained.

---

[86] Mini circuits: ZASWA-2-50DRA+

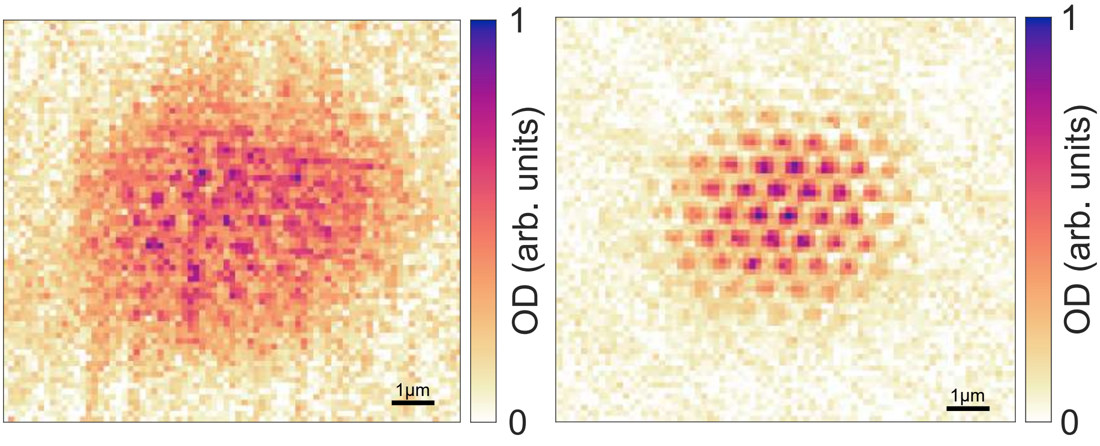

(a)

(b)

Figure 5.4: Influence of interactions during the matter-wave protocol - Matter-wave microscopy of 1.4×10^4 atoms in the ground-state of a triangular lattice at a magnetic field of **(a)** $702\,\text{G}$ corresponding to a scattering length of ca. $76\,a_0$ and **(b)** $560\,\text{G}$ corresponding to a scattering length of ca. $1.4\,a_0$. The presence of interactions during the matter-wave protocol distorts the image. The matter-wave magnification for both images is $M \approx \omega t_{\text{tof}} = 2\pi \times 1.08\,\text{kHz} \times 3.5\,\text{ms} \approx 23.8$.

The magnification may be slightly altered by the time-dependent harmonic trap. However upon comparing the apparent lattice spacing in figure 5.4b with the known lattice spacing in the triangular lattice of $a_{\text{latt}} = 2/3\lambda = 709\,\text{nm}$ we find that the magnification can be well approximated by $M \approx \omega t_{\text{tof}} = 2\pi \times 1.08\,\text{kHz} \times 3.5\,\text{ms} \approx 23.8$.

Currently we shut off the interactions via a slow magnetic field ramp within $10\,\text{ms}$ before initializing the matter-wave protocol. To study also strongly interacting systems, we need a technique to shut off the interactions much faster at the start of the harmonic evolution. To this end, we have built a narrow-resonance RF antenna (see section 3.2.3) to address a transition between the $|F = 1, m_F = 1\rangle$-state and the $|F = 1, m_F = 0\rangle$-state at a magnetic field of $690\,\text{G}$. Here, the scattering length of the $|F = 1, m_F = 1\rangle$-state is still ca. $52\,a_0$ while for the $|F = 1, m_F = 0\rangle$-state it is ca. $5\,a_0$. We achieve a Rabi frequency of $7\,\text{kHz}$ and plan to use a π-pulse to shut off the interactions. This has yet to be tested. Alternatively, one could employ a Raman transition to achieve much higher Rabi frequencies that are also independent of the magnetic field [131].

5.4 | The Matter-Wave Talbot Effect

As mentioned in the previous section, the presence of interaction limits the application of the matter-wave microscope to incoherent systems. However with the broad Feshbach resonance of ^{7}Li, we can shut off the interactions and study coherent systems on a single-site level. The first coherent effect that we study is the matter-wave Talbot effect. In section 5.2 we briefly introduced the optical Talbot effect, where coherent light that is diffracted from a grating with periodicity a_{latt} experiences a periodic revival of this pattern in distances $z_{\text{Talbot}} = a_{\text{latt}}^2/\lambda_{\text{L}}$. Analogously, the Talbot effect is also present for matter-waves [132–134]. In the context of cold atoms in optical lattices this can be understood as follows: we consider a coherent ground-state in a 1D optical lattice of lattice spacing a_{latt}. We can decompose the wavefunction of said state in the plane wave basis with wavevectors that are integer multiples of $k = 2\pi/a_{\text{latt}}$. When switching off the optical lattice, the dynamics is given by the corresponding kinetic energies $E_n = n^2(\hbar k)^2/(2m)$ $(n \in \mathbb{Z})$. These are all multiples of the same fundamental energy, the recoil energy of the lattice. The inverse of the corresponding frequency is the Talbot time

$$T_{\text{Talbot}} = 2\pi\frac{2m}{\hbar k^2} = 2\pi\frac{2ma_{\text{latt}}^2}{\hbar(2\pi)^2} = \frac{2a_{\text{latt}}^2}{h/m}. \tag{5.16}$$

For time of flight in an infinitely large periodic system, the wavefunction after integer multiples of T_{Talbot} would always be identical to the wavefunction at $t_{\text{tof}} = 0$. For $t_{\text{tof}} = \frac{2n-1}{2}T_{\text{Talbot}}$ the wavefunction is displaced by $a_{\text{latt}}/2$ which we call an anti-revival. In real systems with finite correlation length, the magnitude of the revivals is reduced for larger times. This can be used to directly access the g_1 correlation function [135, 136]. We define the strength of the n^{th} revival as the overlap between the initial state at $t_{\text{tof}} = 0$ and the state after a $t_{\text{tof}} = nT_{\text{Talbot}}$. Then the strength of the n^{th} revival is directly proportional to the g_1 correlation function of lattice sites with distance $2n$ and the strength of the n^{th} anti-revival is directly proportional to the g_1 correlation function of lattice sites with distance $2n-1$. A graphical visualization of the Talbot effect in 1D and 2D is given in figure 5.5.

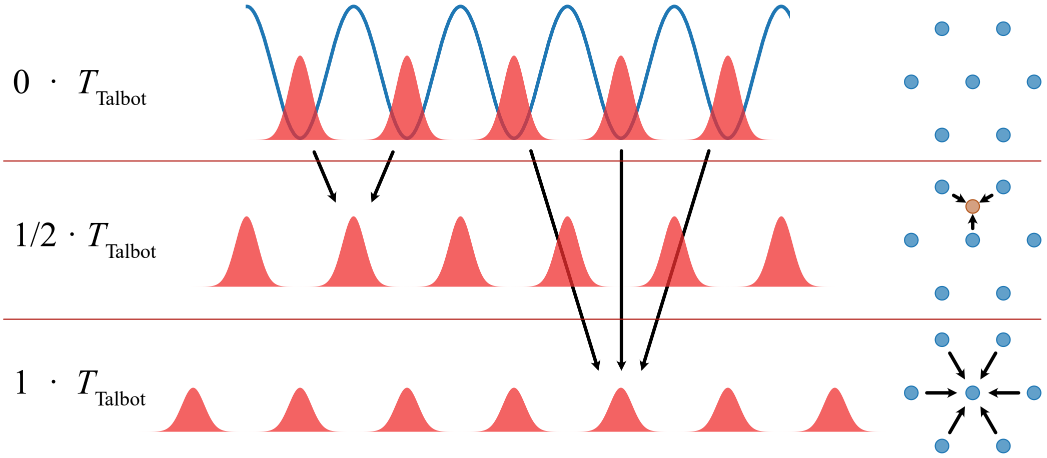
$0 \cdot T_{\text{Talbot}}$
$1/2 \cdot T_{\text{Talbot}}$
$1 \cdot T_{\text{Talbot}}$

Figure 5.5: Visualization of the Talbot effect in 1D and 2D - A coherent matter-wave is released from a periodic potential either in 1D or 2D. After the Talbot time $T_{\text{Talbot}} = 2ma_{\text{latt}}^2/h$ the initial density distribution is recovered. After half a Talbot time, the density distribution experiences a translation by $a_{\text{latt}}/2$.

In a 2D triangular lattice, the allowed wavevectors are linear combinations of the reciprocal lattice vectors $\boldsymbol{b}_{\text{i}}$ with $\text{i} = 1, 2, 3$. Following the argumentation from above, all energies are then integer multiples of the fundamental energy

$$E_{\text{rec,latt}} = \frac{\hbar^2(\sqrt{3}\frac{2\pi}{\lambda})^2}{2m} = h \times 75.53\,\text{kHz}. \tag{5.17}$$

This corresponds to a Talbot time of ca. $T_{\text{Talbot}} \approx 13.2\,\mu\text{s}$.

In the following we want to focus on the direct imaging of Talbot revivals from atoms in the ground-state of a 2D triangular lattice. Preliminary data on this topic was already presented in [128], but the finite interaction strength limited the resolution of the matter-wave protocol. As mentioned above we can initialize the matter-wave protocol via two different approaches. We can use an RF switch to almost instantaneously increase the RF power on the AOMs while switching the frequencies of the three lattice beams to a non-interfering harmonic trap. With this method the imaging of the Talbot revivals is straight-forward. We can switch off all potentials via an additional RF switch, wait for a certain amount of time and then initiate the matter-wave protocol. However we found that for a precise measurement of the Talbot revivals the timing is crucial and we were not too confident in the long-term stability of this matter-wave lens. We thus use our second approach to initialize the magnification by switching the AOM frequencies while keeping the intensity lock on. We then ramp up the power in the beams to the final value within $100\,\mu\mathrm{s}$ and wait for the rest of the $T/4$ pulse.

In section 5.2 we argued that small deviations from the focusing conditions in the harmonic trap can be mapped to small initial time of flights. Consequently, we can also adapt the harmonic evolution time t_{ho} to image the density distribution after a short time of flight. The position operator after a time of flight $t_{\mathrm{tof}} = nT_{\mathrm{Talbot}}$ is given by

$$\hat{x}(t_{\mathrm{tof}} = nT_{\mathrm{Talbot}}) = \hat{x}(0) + nT_{\mathrm{Talbot}}\frac{\hat{p}(0)}{m}. \tag{5.18}$$

Comparing this to the position operator for the evolution in a harmonic trap

$$\hat{x}(t_{\mathrm{ho}}) = \hat{x}(0)\cos(\omega t_{\mathrm{ho}}) + \frac{\hat{p}(0)}{m\omega}\sin(\omega t_{\mathrm{ho}}) \tag{5.19}$$

we can see that for

$$t_{\mathrm{ho}} = \frac{1}{\omega}\arctan(n\omega T_{\mathrm{Talbot}}) \tag{5.20}$$

the position operator becomes

$$\hat{x}(t_{\mathrm{ho}}) = \hat{x}(nT_{\mathrm{Talbot}})\cos(\omega t_{\mathrm{ho}}) = \frac{\hat{x}(nT_{\mathrm{Talbot}})}{\sqrt{1+(n\omega T_{\mathrm{Talbot}})^2}}. \tag{5.21}$$

It follows that we can image the n^{th} Talbot revival just by tuning the harmonic evolution time t_{ho} in the matter-wave protocol. The magnification is then re-scaled to $M' = \sqrt{\frac{1+(\omega t_{\mathrm{tof}})^2}{1+(n\omega T_{\mathrm{Talbot}})^2}}$. Figure 5.6 shows a graphical representation of this mapping. We note that this mapping also allows us to image Talbot revivals of negative order by tuning the harmonic evolution time in the other direction. It also follows from equation 5.20 that the Talbot revivals are not equidistant in the harmonic evolution time t_{ho}.

We now use this approach to directly image the Talbot revivals in the 2D lattice. We prepare the atoms in the ground-state, initiate the matter-wave protocol as described above and vary the evolution time t_{ho} in the harmonic trap. As expected we see a density distribution that varies between triangular lattices at integer Talbot revivals and a honeycomb lattice which is the inverted triangular lattice at anti-revivals. In between these revivals, the density distribution gets washed out. We analyze these images by performing a Fourier analysis on the OD images. We then plot the contrast for one of the corresponding momentum components as a function of the harmonic evolution time. The result of this measurement is shown in figure 5.7. We can now identify the 0^{th} Talbot revival which corresponds to the original image of the density distribution. The measured Talbot time of $13\,\mu\mathrm{s}$ matches well to our calculated prediction of $13.2\,\mu\mathrm{s}$ within the experimental resolution of $1\,\mu\mathrm{s}$. By performing this analysis on all three axes at the same time, we can very precisely measure the eccentricity of the harmonic

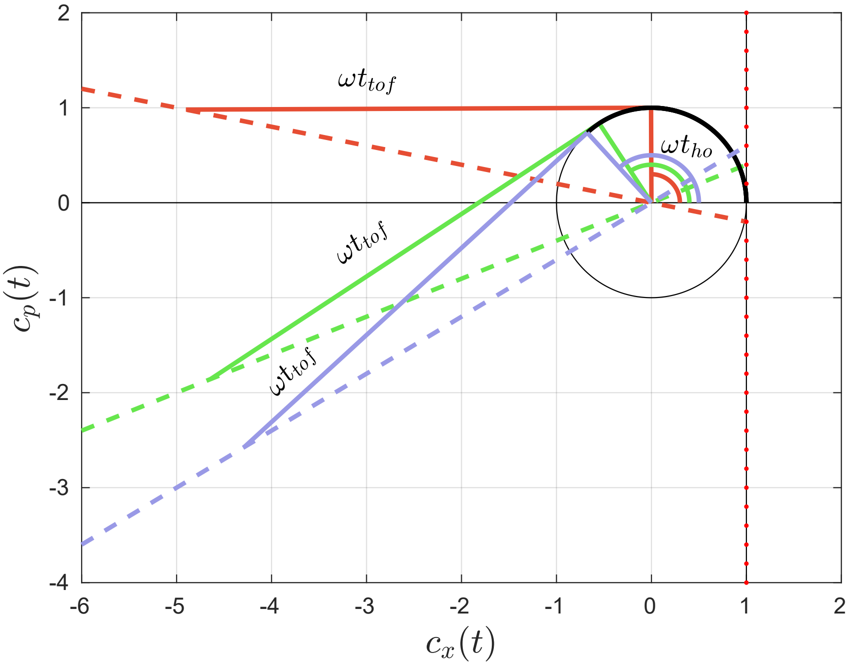

Figure 5.6: Mapping free evolution to the evolution in a harmonic trap - The vertical line at $c_x = 1$ indicates possible realisations of the time dependent position operator $\hat{x}(t) = c_x(t)\hat{x}(0) + c_p(t)\hat{p}(0)$ during time of flight. The red points on that line indicate the equidistant Talbot revivals. We consider the cases of three different harmonic evolution times t_{ho} (red, green and blue circular arcs), starting from $(c_x(0), c_p(0)) = (1, 0)$. The positions at the end of the matter-wave protocols correspond to the respective Talbot revivals as indicated by the straight dotted lines. Figure taken from [128].

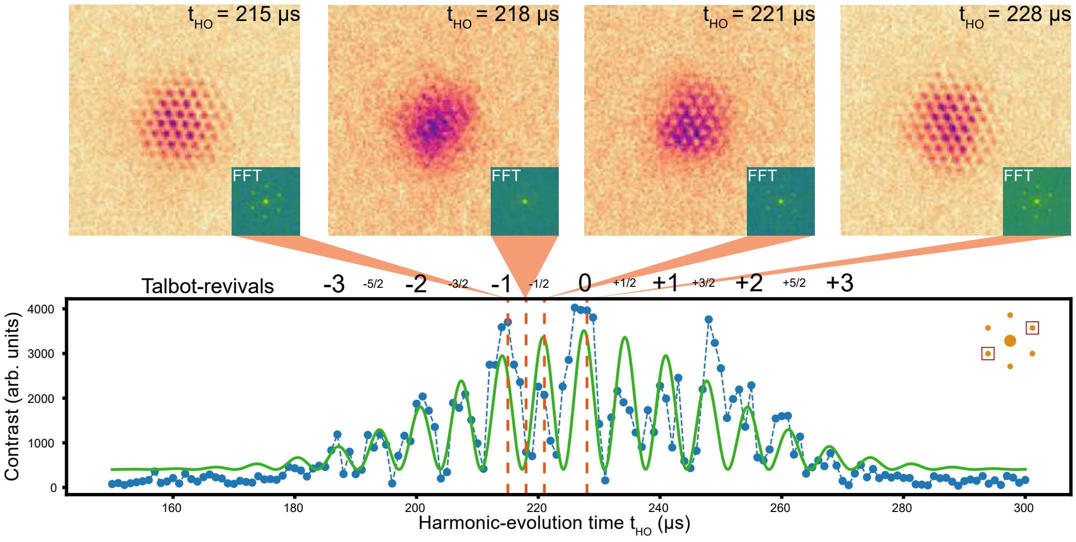

Figure 5.7: Analysis of the Talbot revivals - We vary the harmonic evolution time t_{ho} while taking images of the density distribution with the matter-wave microscope. For integer multiples of the Talbot time, we observe revivals of the original density pattern (OD images in the top row). We perform a Fourier analysis for each individual image (inlets in the top row) and plot the contrast of the corresponding momenta as a function of the harmonic evolution time (blue circles connected by dashed blue lines). The green solid curve is a heuristic sinusoidal fit with a Gaussian envelope. We can see that the contrast vanishes over ca. four Talbot revivals which corresponds well to the system size of ca. 8×8 lattice sites. While writing this thesis, this measurement was performed by my PhD colleague Justus Brüggenjürgen who also wrote the computer code for the analysis. We both equally contributed to the interpretation of the Data.

trap, because any anisotropy would result in a timing mismatch of the corresponding Talbot revivals. In fact, we use this measurement to set the beam balance for the matter-wave protocol to create an isotropic harmonic trap. As of writing this thesis, we work on expanding these measurements to extract the g_1 correlation function for gases of different temperatures. Preliminary measurements show that the number of observable revivals drops with increasing temperature. By employing the high precision thermometry presented in [18], we are able to extract the temperature from the density profile of single shot images. This is still a work in progress though and more on this topic will be found in the upcoming thesis of my PhD colleague Justus Brüggenjürgen.

5.5 Conclusion and Outlook

In this chapter we have demonstrated matter-wave microscopy of Lithium atoms in an optical lattice via an optical matter-wave lens, allowing for spin-independent imaging. Using the broad Feshbach resonance of ^{7}Li, we are able to turn off the interactions during the matter-wave protocol and image coherent systems. This is nicely illustrated by observing the Talbot revivals of a coherent state in a 2D triangular optical lattice. With this technique we get access to the g_1 correlation function and study it for clouds of different temperature. So far we analyzed the Talbot revivals globally over the whole system. By employing a phase-retrieval algorithm we hope to access the phase information of single lattice sites [137]. A promising next experimental step will be to also study systems with interactions. For this purpose we have built an RF antenna that might be used to transfer the atoms from an interacting to a non-interacting internal state at the beginning of the matter-wave protocol. If we find the Rabi frequency to be not sufficiently high, we might use a magnetic field independent Raman transition instead. In the future, we plan to combine the matter-wave microscopy with the technique of free-space fluorescence imaging that has been already demonstrated for ^{87}Rb [138–140] and ^{6}Li [141] enabling us to enter the regime of spin-resolved single particle detection.

CHAPTER 6

Conclusion and Outlook

In this thesis, we presented the apparatus with which we perform matter-wave microscopy of degenerate ^{7}Li gases in an optical lattice. In chapter 2, we summarized the properties of the bosonic isotope ^{7}Li that are important for the successful creation of quantum degenerate gases from an experimentalists point of view. Here, mainly the disadvantageous collisional properties pose unique challenges on the pathway to degeneracy. Balancing the low elastic collision rate and the high three-body loss rate requires a precisely engineered experimental cycle, which we presented in chapter 3. Through improvements of the 2D- and 3D-MOT, we were able to increase the particle number after the sub-Doppler cooling by a factor of $\sim 5-10$. We developed an experimental sequence that allows us to handle the disadvantageous scattering properties of ^{7}Li by adiabatically compressing and decompressing a newly implemented plugged magnetic quadrupole trap during RF evaporation. Before reaching quantum degeneracy, we transfer the atoms into an optical dipole trap and, after an internal state transfer, evaporatively cool them to Bose-Einstein condensation in the vicinity of a Feshbach resonance.

In chapter 4 we presented our approach on a multi-frequency optical lattice, which in principle allows us to dynamically tune the geometry of the lattice structure smoothly between a triangular and a honeycomb lattice via boron-nitride like lattices. We introduced the concept of the geometry phase as the single parameter that describes the lattice structure and gave a detailed description of the experimental implementation. First calibration measurements of the geometry phase gave inconclusive results. We identified a phenomenon of additional lattice structures that appear even when the laser beams are detuned far beyond the relevant energy/time scales. We attribute the issues with the inconclusive geometry phase to these additional lattices and propose to solve this issue in the future by going to even further detunings. To this end, we have already built in new EOMs in the laser system, the effect of which on the geometry phase has yet to be tested.

Finally, in chapter 5 we demonstrated the first realization of a matter-wave microscope with an optical matter-wave lens. This allows for a spin-independent magnification protocol. Consequently, we can use the broad Feshbach resonances of ^{7}Li to tune the interaction strength during the matter-wave protocol. We first presented a theoretical description of the focusing condition and studied the influence of small deviations. We then presented the experimental procedure to image the density distribution of atoms in triangular optical lattices with single lattice-site resolution. We used this to measure the matter-wave Talbot effect for a coherent state, which in the future will enable us to access the g_1 correlation function.

We currently work on expanding upon these results by studying systems with different temperature. The high precision thermometry presented in [18] allows to extract the temperature from the density profiles in single shots. Complementary, we also plan to improve the analysis by employing a phase-retrieval algorithm to access the phase information of single lattice sites

[137]. We also work on experimental schemes to shut off the interactions immediately at the start of the matter-wave protocol. This would enable the study of interacting systems. For further studies of strongly correlated systems it would be very important to also reach single atom sensitivity by means of spin-resolved free-space fluorescence imaging [138, 141]. For the measurements presented in this thesis, the objective with NA of 0.5 [57] was temporarily removed from the setup. As an important step towards single-atom sensitive imaging, we will reinstall the objective in the near future. We also want to mention that the experimental apparatus is still suited for conventional quantum gas microscopy. The combination of this with the new technique of matter-wave microscopy could be fruitful.

With these additions to the matter-wave microscope, we could further investigate the observed lattice structures that emerge from off-resonant laser beams to compare it to the mechanism of [109, 50]. With a working multi-frequency lattice we could then study also different lattice geometries like boron-nitride lattices and use quenches of the lattice geometry to excite the system to higher Bloch bands [19]. Here, the most interesting subject of study would be a chiral superfluid, the realization of which was recently reported in such a system [100]. With the matter-wave microscope combined with a high-resolution objective we could directly image the vortex in the corresponding orbital. We can also think of applying the matter-wave microscopy in contexts outside of optical lattices. Via a cyclic amplitude modulation in our optical dipole trap, we could induce vortices in the BEC and directly access the healing length for different interaction strengths via matter-wave microscopy. By further investigation of rapidly rotating Bose gases, we could create artificial magnetic fields and explore the physics of the lowest Landau level [142–145]. We could realize such rotating traps also via holographic measures with a digital mirror device or a liquid crystal spatial light modulator. In the limit of only few particles and rotation frequencies close to the trap frequency, we could enter a fractional quantum hall state similar to the state that has recently been realized in a lattice with magnetic flux [146]. The excitations of the ground-state are then to believed to experience anyonic behavior that we might be able to access with the matter-wave microscope.

APPENDIX A

Thermodynamic Considerations in the Magnetic Quadrupole Trap

A.1 | General Considerations on the Trapping Potential

In the Zeeman regime, the energy ΔE of a neutral atom in a magnetic field $|\boldsymbol{B}(\boldsymbol{r})|$ is given by

$$\Delta E(\boldsymbol{r}) = m_F g_F \mu_\mathrm{B} |\boldsymbol{B}(\boldsymbol{r})|, \tag{A.1}$$

with the magnetic quantum number m_F of the respective state, the Landé-factor g_F and the Bohr magneton μ_B. Near the center, the quadrupole field that is generated by our main coils in anti-Helmholtz configuration can be described by a single parameter b, the gradient of the field along the z-direction:

$$\boldsymbol{B}(\boldsymbol{r}) = b \begin{pmatrix} -x/2 \\ -y/2 \\ z \end{pmatrix}. \tag{A.2}$$

Consequently, the absolute value of the magnetic field is given by

$$|\boldsymbol{B}(\boldsymbol{r})| = b\sqrt{\frac{x^2+y^2}{4} + z^2}. \tag{A.3}$$

We introduce the parameter $P := m_F g_F \mu_\mathrm{B} b$ such that we can express the potential U for the atoms as

$$U(\boldsymbol{r}) = P\sqrt{\frac{x^2+y^2}{4} + z^2} - mgz, \tag{A.4}$$

where m is the atomic mass of ^{7}Li and g is the acceleration of gravity. The influence of gravity can be neglected as long as $b >> b_g = mg/m_F g_F \mu_\mathrm{B} = 1.2\,\mathrm{G/cm}$. During the evaporation in the magnetic trap the minimum gradient that we apply is $52.2\,\mathrm{G/cm}$. We thus neglect the gravitational sag for the following considerations.

A.2 | Diabatic Loading of the Magnetic Trap

In the following, we want to determine the best way to load the atoms into the magnetic trap. Here we only cover diabatic loading. After the Gray Molasses cooling, the initial atomic density profile can be approximated by a three-dimensional Gaussian distribution

$$n_\mathrm{i}(\boldsymbol{r}) = N \prod_{\mathrm{j}=1}^{3} \frac{1}{\sqrt{2\pi}\sigma_\mathrm{j}} e^{-\frac{x_j^2}{2\sigma_\mathrm{j}^2}}. \tag{A.5}$$

Following [147], we assume an isotropic cloud with initial size $\sigma_\mathrm{i} = \sigma_1 = \sigma_2 = \sigma_3$. We can calculate the potential energy U_Pot in the magnetic trap by projecting the spatial distribution onto the potential of the magnetic trap (while ignoring the gravitational sag).

$$U_\mathrm{Pot} = P \int_{-\infty}^{+\infty} \int_{-\infty}^{+\infty} \int_{-\infty}^{+\infty} \left(\sqrt{\frac{x^2+y^2}{4} + z^2} \right) n_\mathrm{i}(\boldsymbol{r}) dx dy dz. \tag{A.6}$$

Using the virial theorem we get the following relation between the initial temperature of the Gray Molasses T_i and the final temperature in the magnetic trap T_f [148]

$$\frac{9}{2} N k_\mathrm{B} T_\mathrm{f} = \frac{3}{2} N k_\mathrm{B} T_\mathrm{i} + U_\mathrm{Pot}, \tag{A.7}$$

with the Boltzmann constant k_B. By solving equation A.6 one finds [147]:

$$T_\mathrm{f} = \frac{T_\mathrm{i}}{3} + \kappa \frac{P\sigma_i}{k_\mathrm{B}} \tag{A.8}$$

$$\kappa \approx 0.24. \tag{A.9}$$

The density distribution $n_\mathrm{f}(\boldsymbol{r})$ in the magnetic trap is given by [149]

$$n_\mathrm{f}(\boldsymbol{r}) = \frac{N}{32\pi} \left(\frac{P}{k_\mathrm{B} T_\mathrm{f}} \right)^3 \exp\left\{ \left[-P \frac{\sqrt{\frac{x^2+y^2}{4} + z^2}}{k_\mathrm{B} T_\mathrm{f}} \right] \right\}. \tag{A.10}$$

It follows that the peak density $n_\mathrm{f}(0)$ is given by

$$n_\mathrm{f}(0) = \frac{N}{32\pi} \left(\frac{P}{k_\mathrm{B} T_\mathrm{f}} \right)^3. \tag{A.11}$$

By multiplying this with the thermal de-Broglie wavelength $\Lambda_T = (\frac{h^2\beta}{2\pi m})^{1/2}$ with $\beta = (k_\mathrm{B}T_\mathrm{f})^{-1}$ we can express the peak phase-space density ρ_0 in the magnetic trap as

$$\begin{aligned} \rho_0 &= n_\mathrm{f}(0)\Lambda_T^3 \\ &= \left(\frac{NP^3\beta^3}{32\pi} \right) \left(\frac{h^2\beta}{2\pi m} \right)^{3/2}. \end{aligned} \tag{A.12}$$

Rewriting this result in terms of b we get

$$\begin{aligned} \rho_0(N, b, T_\mathrm{i}, \sigma_i) &= \frac{N}{32\pi} \left(\frac{h^2}{2\pi m} \right)^{3/2} \frac{P^3}{(k_\mathrm{B}T_\mathrm{f})^{9/2}} \\ &\overset{A.8}{=} \frac{N}{32\pi} \left(\frac{h^2}{2\pi m} \right)^{3/2} \frac{m_F^3 g_F^3 \mu_\mathrm{B}^3 b^3}{(\frac{k_\mathrm{B}T_\mathrm{i}}{3} + \kappa m_F g_F \mu_\mathrm{B} b \sigma_i)^{9/2}}. \end{aligned} \tag{A.13}$$

By taking the derivative with regard to b we can find the optimum magnetic field gradient b_0 for given initial parameters T_i, σ_i as

$$b_0 = \frac{2k_\mathrm{B}T_\mathrm{i}}{3\kappa m_F g_F \mu_\mathrm{B} \sigma_i}. \tag{A.14}$$

Diabatically turning on the magnetic trap with this gradient b_0 will maximize the phase-space density. This is called mode matching. In a shallower trap, the atomic cloud would spread out and the atomic density would be reduced. In a tighter confinement, the magnetic trap imprints too much potential energy onto the atoms. Either way the phase-space density would decrease. Figure A.1 shows the acquired peak phase-space density as a function of the capture gradient b for two different initial conditions with the same initial phase-space density. For the case of the initial temperature and size of the atomic cloud after the Gray Molasses and optical dark state pumping in our system, we calculate an optimum capture gradient of ca. $13\,\mathrm{G/cm}$. We note that around the optimum the PSD is not too sensitive to the actual value of b. Increasing the gradient by a factor of three barely halves the resulting PSD. We thus empirically scan for optimum experimental parameters around this calculated value (see section 3.4.2). We remark that both initial conditions have an initial peak phase-space density of $\rho_\mathrm{i} = 3.5 \times 10^{-5}$ which is a factor of ca. ~ 3 less than after the mode match. This does not violate Liouville's theorem because we diabatically load the atoms with a Gaussian density distribution into a linear trap with a different density distribution function. When loading a Gaussian density distribution into a harmonic trap, the maximum possible peak phase-space density ratio after the transfer 1 [85].

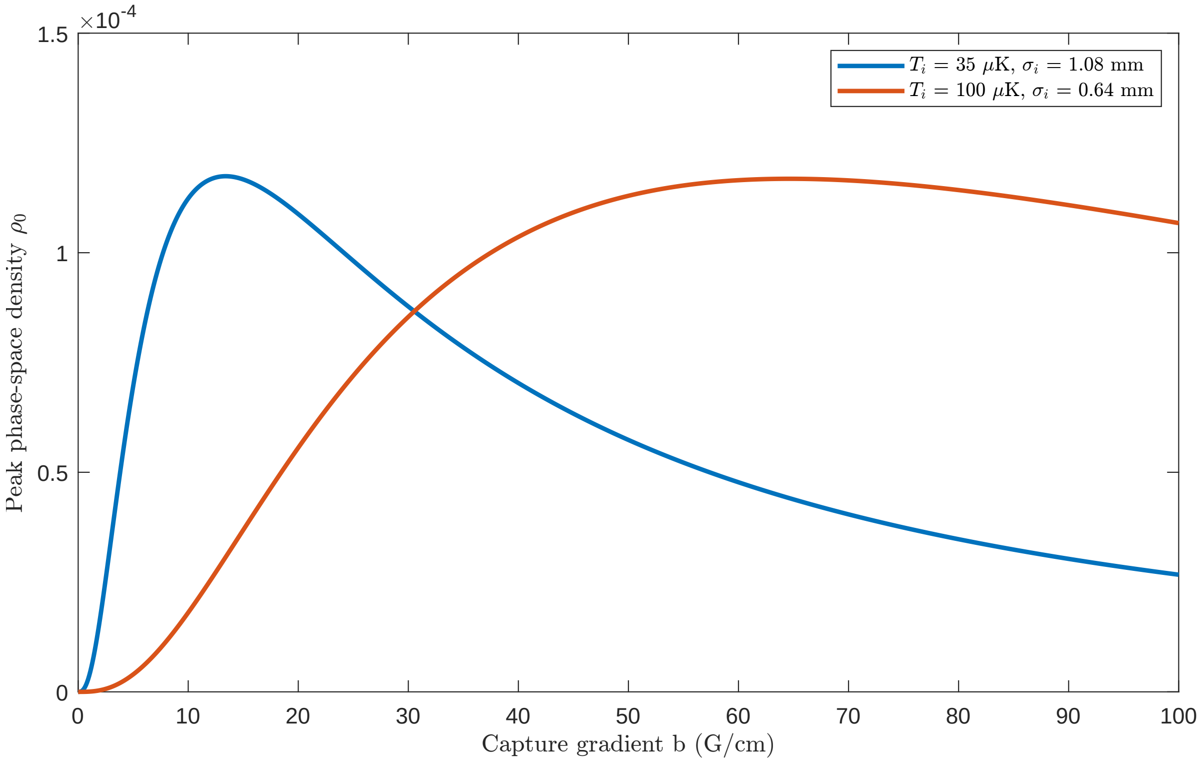

Figure A.1: Peak phase-space density in the magnetic trap as a function of the capture gradient - We plot the peak phase-space densities from equation A.13 for two different initial conditions with the same initial peak phase-space-density of $\rho_\mathrm{i} = 3.5 \times 10^{-5}$ but with different initial temperatures T_i and sizes σ_i. The blue curve corresponds to our starting conditions after the Gray Molasses and optical dark state pumping, whereas the orange curve covers the case for a hotter but more dense initial atomic cloud. We can see that the optimum capture gradient for our magnetic trap should be ca. $13\,\mathrm{G/cm}$.

A.3 | Adiabatic Compression/Decompression

By further analysing the above expressions for the phase-space density, we can gain more insights into the thermodynamics of linear magnetic traps. We know from Liouville's theorem that the phase-space density remains constant under adiabatic manipulation of the trap. We thus can see from equation A.12 that as we adiabatically vary the gradient b of the magnetic trap, the quantity $P^3/T^{9/2}$ must be constant. It follows that for adiabatic variation of b

$$n_0 \propto b \tag{A.15}$$

$$T \propto b^{2/3}. \tag{A.16}$$

These two results can be combined to show that the elastic collision rate $\Gamma_{el} = n\sigma v$ scales as $\Gamma_{\mathrm{el}} \propto b^{4/3}$. We can thus increase the collision rate by adiabatically compressing the magnetic trap to enhance the evaporation process. Adiabatically decompressing the trap can be used to keep the atomic density n_0 at a reasonable level to reduce three-body losses.

To increase the phase-space density, we perform RF evaporation in the magnetic trap while adiabatically decompressing it. However as the magnetic field gradient is changed, the potential energy of the cloud also changes and the applied radio frequency needs to be adjusted accordingly. Let's assume a change of the magnetic field gradient from $b \mapsto b' = \alpha b$. Using the above scaling laws, one can show that the energy ΔE of the radio frequency has to be adjusted to $\Delta E \mapsto \Delta E' = \alpha^{2/3}\Delta E$ to keep the cut-off radius at the same relative density.

We also note that the phase-space density ρ_0 scales linearly with the particle number $\rho_0 \propto N$ whereas with respect to the temperature it scales as $\rho_0 \propto T^{-9/2}$. This stands in contrast to the temperature scaling of the PSD in the Gray Molasses or in optical dipole traps where $\rho_0 \propto T^{-3/2}$. Here we want to emphasize that during the search for optimum experimental parameters the temperature in the linear magnetic trap is much more crucial than what an experimentalist might be used to from harmonic confinements.

A.4 | Measurement of the Phase-Space Density

As we experimentally optimize the evaporation, we need to determine the resulting phase-space density for each parameter setting. For this we can use equation A.12. For each run, we know the value of the experimental parameter P. We thus need to measure the atom number N and the temperature T of the atoms. While the density profile of the atoms in the magnetic trap is given by equation A.10, one can argue [150, 151] that it is not too different from a Gaussian profile such that reliable results can be obtained without adjusting our analysis model. We can thus use a Gaussian fit to extract the atom number N from absorption images. For measuring the temperature of the cloud, we use two independent methods.

The first method is based on measuring the in-situ density profile for single absorption images. We fit a Gaussian distribution to the cloud and measure the full width at half maximum R_{FWHM} of the cloud's density distribution for a given magnetic field gradient b. The temperature can then be calculated using the relation [151]

$$T_{\mathrm{in-situ}} = \frac{2\mu_{\mathrm{B}}}{5k_{\mathrm{B}}} b R_{\mathrm{FWHM}}. \tag{A.17}$$

As a second method, we use standard free ballistic expansion to measure the temperature. We shut off the confining potential and let the system expand for varying times. For each time of flight, we take a destructive absorption image and fit a Gaussian density distribution to the obtained OD image. Assuming again also an initially Gaussian density distribution with width σ_0, we can link the Gaussian width σ of the cloud after some time of flight t to the temperature T_{ToF}:

$$\sigma(t) = \sqrt{\left(\frac{k_{\mathrm{B}} T_{\mathrm{ToF}}}{m}\right) t^2 + \sigma_0^2}. \tag{A.18}$$

Both methods are however limited. For both methods we assume Gaussian density distributions that introduce a small systematic error on the order of a few percent [151]. For the in-situ images, we need to be careful that the Zeeman shift in the cloud might alter the measured density distribution. Additionally, the anisotropy of the magnetic field in combination with the Clebsch-Gordan coefficients for different transitions causes a distortion in the obtained optical density profiles. These effects are more prominent for large clouds at relatively high gradients. Both cases of possible distortions are shown in figure A.2. In these cases we cannot extract a reasonable in-situ density profile. We used to circumvent this by taking absorption images directly after shutting off the magnetic field within ca. 50 µs assuming that the density distribution wouldn't change that much in this short time period. The temperatures obtained in this manner are in good agreement with the temperatures that we measured using the ballistic expansion method. However, in September 2021 while calibrating the magnetic trap, we noticed a malfunction in the electric insulation of the coils. When switching off too large electric currents, the high induction voltages cause an electric arch from the coils to their aluminum holder. To avoid this, we typically limit the maximum magnetic field gradient that we switch off to 52.2 G/cm. We can however still get good measurements of the temperatures for larger magnetic field gradients by adiabatically ramping the gradient down to said value before taking the images for either of the two methods. We then use equations A.15 and A.16 to calculate the initial density and temperature at the larger gradient. We confirmed that the temperatures that we obtain with this procedure match the temperatures for both the in-situ imaging and ballistic expansion method at high magnetic field gradients. We now mostly use the ballistic expansion method at a final magnetic field gradient of 52.2 G/cm to avoid further damaging of the electric insulation.

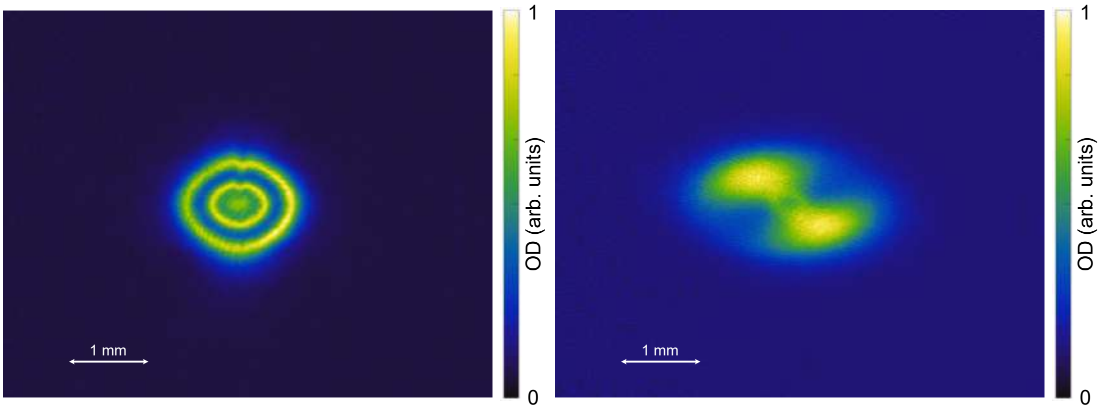

(a) (b)

Figure A.2: Distorted in-situ images of the OD in the magnetic trap - **(a)** At large magnetic field gradients and large atom numbers, the Zeeman shift changes the atomic resonance over the size of the cloud. The absorption imaging light drives spatially different transitions resulting in the observed shell-like structure. **(b)** The anisotropic magnetic field and thus quantization axis in the magnetic trap causes the OD to appear anisotropic as well.

APPENDIX B

Relative Intensity Noise of the Optical Dipole Trap/Lattice Laser

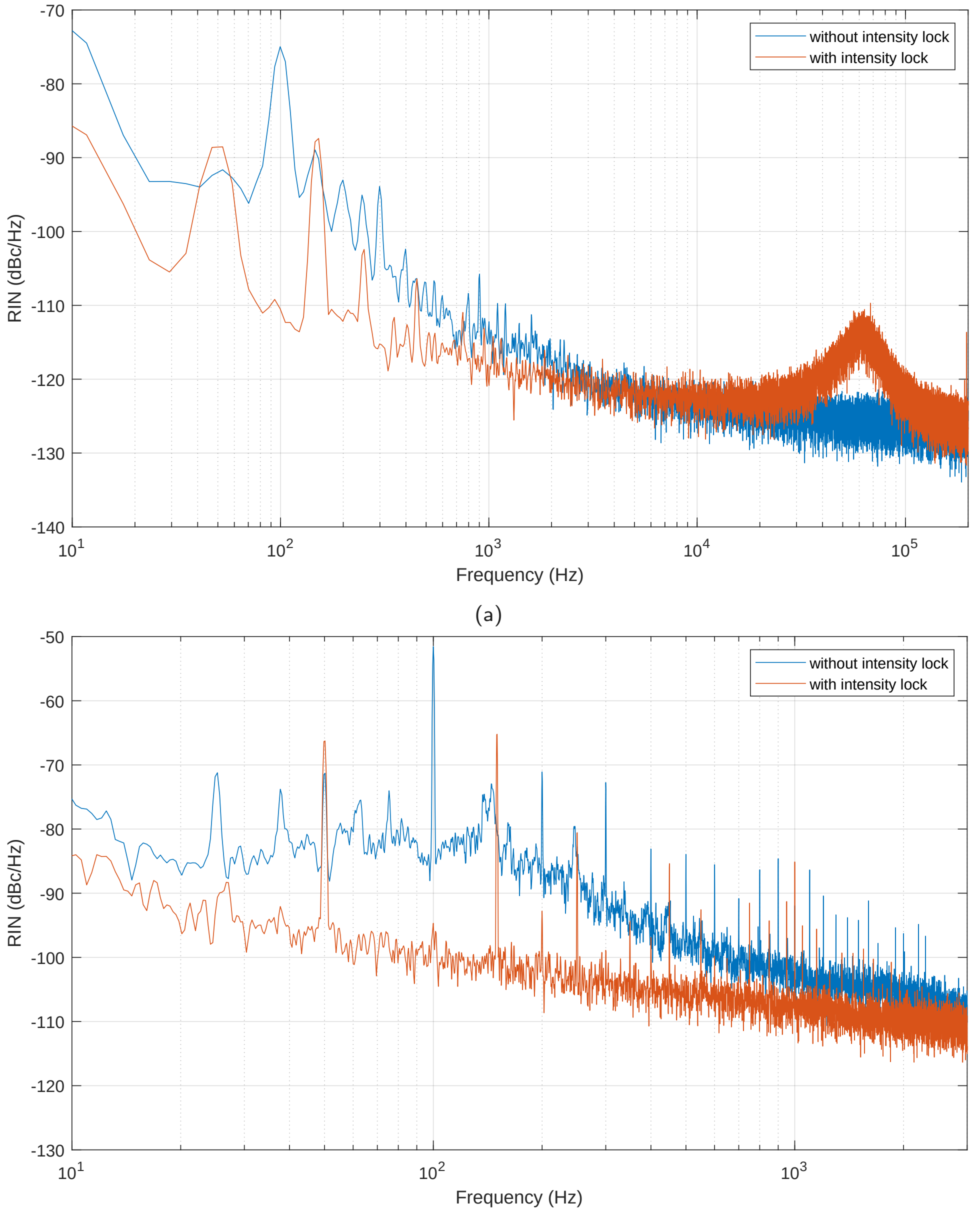

(a)

(b)

Figure B.1: Relative intensity noise (RIN) spectra of the optical dipole trap/lattice laser - We measure the RIN with two different resolutions. We investigate the lower-frequency regime between $10\,$Hz and $12\,$kHz with a resolution of $366\,$mHz and the higher-frequency range between $10\,$Hz and $250\,$kHz with a resolution of $5.8\,$Hz. The data presented here were taken for the beam L_3 at a power of ca. $1\,$W. The RIN spectra for the other beams and different powers look similar. The data were taken with an audio analyzer UPV from Rohde & Schwarz.

Bibliography

[1] R. P. Feynman. “Simulating physics with computers”. In: *International Journal of Theoretical Physics* 21.6-7 (1982), pp. 467–488. DOI: `10.1007/bf02650179` (cit. on p. 1).

[2] M. H. Anderson, J. R. Ensher, M. R. Matthews, C. E. Wieman, and E. A. Cornell. “Observation of Bose-Einstein Condensation in a Dilute Atomic Vapor”. In: *Science* 269.5221 (1995), pp. 198–201. DOI: `10.1126/science.269.5221.198` (cit. on p. 1).

[3] C. C. Bradley, C. A. Sackett, J. J. Tollett, and R. G. Hulet. “Evidence of Bose-Einstein Condensation in an Atomic Gas with Attractive Interactions”. In: *Phys. Rev. Lett.* 75.9 (1995), pp. 1687–1690. DOI: `10.1103/PhysRevLett.75.1687` (cit. on p. 1).

[4] K. B. Davis, M. Mewes, M. R. Andrews, N. J. van Druten, D. S. Durfee, D. M. Kurn, and W. Ketterle. “Bose-Einstein Condensation in a Gas of Sodium Atoms”. In: *Phys. Rev. Lett.* 75.22 (1995), pp. 3969–3973. DOI: `10.1103/PhysRevLett.75.3969` (cit. on pp. 1, 44).

[5] I. Bloch, J. Dalibard, and S. Nascimbène. “Quantum simulations with ultracold quantum gases”. In: *Nature Physics* 8.4 (2012), pp. 267–276. DOI: `10.1038/nphys2259` (cit. on p. 1).

[6] A. Hemmerich and T. W. Hansch. “Two-dimesional atomic crystal bound by light”. In: *Phys. Rev. Lett.* 70.4 (1993), pp. 410–413. DOI: `10.1103/PhysRevLett.70.410` (cit. on p. 1).

[7] G. Grynberg, B. Lounis, P. Verkerk, J. Courtois, and C. Salomon. “Quantized motion of cold cesium atoms in two- and three-dimensional optical potentials”. In: *Phys. Rev. Lett.* 70.15 (1993), pp. 2249–2252. DOI: `10.1103/PhysRevLett.70.2249` (cit. on p. 1).

[8] I. Bloch. “Ultracold quantum gases in optical lattices”. In: *Nature Physics* 1.1 (2005), pp. 23–30. DOI: `10.1038/nphys138` (cit. on pp. 1, 57).

[9] D. Jaksch, C. Bruder, J. I. Cirac, C. W. Gardiner, and P. Zoller. “Cold Bosonic Atoms in Optical Lattices”. In: *Phys. Rev. Lett.* 81.15 (1998), pp. 3108–3111. DOI: `10.1103/PhysRevLett.81.3108` (cit. on p. 1).

[10] J. Hubbard. “Electron correlations in narrow energy bands”. In: *Proceedings of the Royal Society of London. Series A. Mathematical and Physical Sciences* 276.1365 (1963), pp. 238–257. DOI: `10.1098/rspa.1963.0204` (cit. on p. 1).

[11] C. Chin, R. Grimm, P. Julienne, and E. Tiesinga. “Feshbach resonances in ultracold gases”. In: *Reviews of Modern Physics* 82.2 (2010), pp. 1225–1286. DOI: `10.1103/RevModPhys.82.1225` (cit. on pp. 1, 57).

[12] M. Greiner, O. Mandel, T. Esslinger, T. W. Hansch, and I. Bloch. “Quantum phase transition from a superfluid to a Mott insulator in a gas of ultracold atoms”. In: *Nature* 415.6867 (2002), pp. 39–44. DOI: `10.1038/415039a` (cit. on p. 1).

[13] R. Jordens, N. Strohmaier, K. Gunter, H. Moritz, and T. Esslinger. "A Mott insulator of fermionic atoms in an optical lattice". In: *Nature* 455.7210 (2008), pp. 204–7. DOI: `10.1038/nature07244` (cit. on p. 1).

[14] U. Schneider, L. Hackermuller, S. Will, T. Best, I. Bloch, T. A. Costi, R. W. Helmes, D. Rasch, and A. Rosch. "Metallic and Insulating Phases of Repulsively Interacting Fermions in a 3D Optical Lattice". In: *Science* 322.5907 (2008), pp. 1520–5. DOI: `10.1126/science.1165449` (cit. on p. 1).

[15] W. S. Bakr, A. Peng, M. E. Tai, R. Ma, J. Simon, J. I. Gillen, S. Folling, L. Pollet, and M. Greiner. "Probing the Superfluid-to-Mott insulator Transition at the Single-Atom Level". In: *Science* 329.5991 (2010), pp. 547–50. DOI: `10.1126/science.1192368` (cit. on pp. 1, 57, 67).

[16] J. F. Sherson, C. Weitenberg, M. Endres, M. Cheneau, I. Bloch, and S. Kuhr. "Single-atom-resolved fluorescence imaging of an atomic Mott insulator". In: *Nature* 467.7311 (2010), pp. 68–72. DOI: `10.1038/nature09378` (cit. on pp. 1, 57, 67).

[17] S. Kuhr. "Quantum-gas microscopes: a new tool for cold-atom quantum simulators". In: *National Science Review* 3.2 (2016), pp. 170–172. DOI: `10.1093/nsr/nww023` (cit. on pp. 1, 67).

[18] L. Asteria, H. P. Zahn, M. N. Kosch, K. Sengstock, and C. Weitenberg. "Quantum gas magnifier for sub-lattice-resolved imaging of 3D quantum systems". In: *Nature* 599 (2021), pp. 571–575. DOI: `10.1038/s41586-021-04011-2` (cit. on pp. 1, 2, 63, 64, 67, 68, 73, 78, 79).

[19] M. N. Kosch, L. Asteria, H. P. Zahn, K. Sengstock, and C. Weitenberg. "Multifrequency optical lattice for dynamic lattice-geometry control". In: *Phys. Rev. Research* 4 (2022), p. 043083. DOI: `10.1103/PhysRevResearch.4.043083` (cit. on pp. 2, 57, 58, 60–63, 66, 80).

[20] D. A. Steck. *Rubidium 85 D Line Data*. `http://steck.us/alkalidata`. 2008 (cit. on p. 3).

[21] D. A. Steck. *Rubidium 87 D Line Data*. `http://steck.us/alkalidata`. 2001 (cit. on p. 3).

[22] D. A. Steck. *Cesium D Line Data*. `http://steck.us/alkalidata`. 1998 (cit. on pp. 3, 8).

[23] D. A. Steck. *Sodium D Line Data*. `http://steck.us/alkalidata`. 2000 (cit. on p. 3).

[24] T. G. Tiecke. "Properties of Potassium". In: (2019) (cit. on p. 3).

[25] M. E. Gehm. *Properties of* ^{6}*Li*. `https://jet.physics.ncsu.edu/techdocs/pdf/PropertiesOfLi.pdf`. 2003 (cit. on pp. 3, 6, 11).

[26] R. G. Hulet, J. H. V. Nguyen, and R. Senaratne. "Methods for preparing quantum gases of lithium". In: *Rev Sci Instrum* 91.1 (2020), p. 011101. DOI: `10.1063/1.5131023` (cit. on pp. 3, 4, 13, 14, 29).

[27] C. B. Alcock, V. P. Itkin, and M. K. Horrigan. "Vapour Pressure Equations for the Metallic Elements: 298–2500K". In: *Canadian Metallurgical Quarterly* 23 (1984), pp. 309–313 (cit. on p. 3).

[28] *Quantities, units, and symbols in physical chemistry*. eng. 3rd ed. Cambridge, UK: RSC Pub., 2007 (cit. on p. 4).

[29] *WebElements*. `https://www.webelements.com`. Accessed: 2023-07-23 (cit. on p. 4).

[30] Y. Zhang, J. R. G. Evans, and S. Yang. "Corrected Values for Boiling Points and Enthalpies of Vaporization of Elements in Handbooks". In: *Journal of Chemical & Engineering Data* 56.2 (2011), pp. 328–337. DOI: `10.1021/je1011086` (cit. on p. 4).

[31] D. Das and V. Natarajan. "Absolute frequency measurement of the lithium D lines: Precise determination of isotope shifts and fine-structure intervals". In: *Phys. Rev. A* 75.5 (2007). DOI: `10.1103/PhysRevA.75.052508` (cit. on pp. 5–7).

[32] C. J. Sansonetti, C. E. Simien, J. D. Gillaspy, J. N. Tan, S. M. Brewer, R. C. Brown, S. Wu, and J. V. Porto. "Absolute Transition Frequencies and Quantum Interference in a Frequency Comb Based Measurement of the $^{(6,7)}$Li D lines". In: *Phys. Rev. Lett.* 107.2 (2011), p. 023001. DOI: `10.1103/PhysRevLett.107.023001` (cit. on pp. 5–7).

[33] W. I. McAlexander, E. R. Abraham, and R. G. Hulet. "Radiative lifetime of the 2P state of lithium". In: *Phys. Rev. A* 54.1 (1996), R5–R8. DOI: `10.1103/physreva.54.r5` (cit. on pp. 5, 6).

[34] J. Walls, R. Ashby, J. J. Clarke, B. Lu, and W. A. van Wijngaarden. "Measurement of isotope shifts, fine and hyperfine structure splittings of the lithium D lines". In: *The European Physical Journal D* 22.2 (2003), pp. 159–162. DOI: `10.1140/epjd/e2003-00001-5` (cit. on pp. 6, 7).

[35] A. T. Grier, I. Ferrier-Barbut, B. S. Rem, M. Delehaye, L. Khaykovich, F. Chevy, and C. Salomon. "Λ-enhanced sub-Doppler cooling of lithium atoms in D1 gray molasses". In: *Phys. Rev. A* 87.6 (2013). DOI: `10.1103/PhysRevA.87.063411` (cit. on pp. 6, 27, 39).

[36] A. Beckmann, K. D. Böklen, and D. Elke. "Precision measurements of the nuclear magnetic dipole moments of ^{6}Li, ^{7}Li, ^{23}Na, ^{39}K and ^{41}K". In: *Zeitschrift für Physik* 270.3 (1974), pp. 173–186. DOI: `10.1007/bf01680407` (cit. on pp. 7, 8).

[37] E. Arimondo, M. Inguscio, and P. Violino. "Experimental determinations of the hyperfine structure in the alkali atoms". In: *Reviews of Modern Physics* 49.1 (1977), pp. 31–75. DOI: `10.1103/RevModPhys.49.31` (cit. on pp. 7, 8).

[38] *The NIST Reference on Constants, Units, and Uncertainty*. `https://physics.nist.gov/cgi-bin/cuu/Value?gem`. Accessed: 2023-07-24 (cit. on p. 8).

[39] L. Windholz, M. Musso, G. Zerza, and H. Jager. "Precise Stark-effect investigations of the lithium D_1 and D_2 lines". In: *Phys. Rev. A* 46.9 (1992), pp. 5812–5818. DOI: `10.1103/physreva.46.5812` (cit. on p. 8).

[40] M. E. Gehm. "Preparation of an optically-trapped degenerate Fermi gas of ^{6}Li: Finding the route to degeneracy". Duke University, North Carolina, Jan. 2003 (cit. on pp. 8–11).

[41] C. C. Bradley, C. A. Sackett, and R. G. Hulet. "Bose-Einstein Condensation of Lithium: Observation of Limited Condensate Number". In: *Phys. Rev. Lett.* 78.6 (1997), pp. 985–989. DOI: `10.1103/PhysRevLett.78.985` (cit. on pp. 11, 12, 50).

[42] K. Kim, S. Huh, K. Kwon, and J.-y. Choi. "Rapid production of large ^{7}Li Bose-Einstein condensates using D_1 gray molasses". In: *Phys. Rev. A* 99.5 (2019). DOI: `10.1103/PhysRevA.99.053604` (cit. on pp. 11, 14, 16).

[43] H. J. Metcalf and P. van der Straten. *Laser Cooling and Trapping*. Graduate Texts in Contemporary Physics. New York, NY: Springer, 1999. DOI: `10.1007/978-1-4612-1470-0` (cit. on p. 12).

[44] E. R. I. Abraham, W. I. McAlexander, J. M. Gerton, R. G. Hulet, R. Côté, and A. Dalgarno. "Triplet s-wave resonance in ^{6}Li collisions and scattering lengths of ^{6}Li and ^{7}Li". In: *Phys. Rev. A* 55.5 (1997), R3299–R3302. DOI: `10.1103/PhysRevA.55.R3299` (cit. on pp. 12, 15).

[45] J. Amato-Grill. "A Fast ^{7}Li-based Quantum Simulator". PhD Thesis. Harvard University, 2019 (cit. on pp. 12, 16, 41, 49).

[46] J. M. Gerton, C. A. Sackett, B. J. Frew, and R. G. Hulet. "Dipolar relaxation collisions in magnetically trapped ^{7}Li". In: *Phys. Rev. A* 59.2 (1999), pp. 1514–1516. DOI: `10.1103/PhysRevA.59.1514` (cit. on pp. 13, 16).

[47] E. A. Burt, R. W. Ghrist, C. J. Myatt, M. J. Holland, E. A. Cornell, and C. E. Wieman. "Coherence, Correlations, and Collisions: What One Learns about Bose-Einstein Condensates from Their Decay". In: *Phys. Rev. Lett.* 79.3 (1997), pp. 337–340. DOI: `10.1103/PhysRevLett.79.337` (cit. on pp. 13, 16).

[48] D. M. Stamper-Kurn, M. R. Andrews, A. P. Chikkatur, S. Inouye, H. J. Miesner, J. Stenger, and W. Ketterle. "Optical Confinement of a Bose-Einstein Condensate". In: *Phys. Rev. Lett.* 80.10 (1998), pp. 2027–2030. DOI: `10.1103/PhysRevLett.80.2027` (cit. on pp. 13, 16).

[49] R. Grimm, M. Weidemüller, and Y. B. Ovchinnikov. "Optical Dipole Traps for Neutral Atoms". In: *Advances In Atomic, Molecular, and Optical Physics* **42**. Vol. 42. Academic Press, 2000, pp. 95–170. DOI: `https://doi.org/10.1016/S1049-250X(08)60186-X` (cit. on pp. 14, 50, 53, 57).

[50] I. Dimitrova, W. Lunden, J. Amato-Grill, N. Jepsen, Y. Yu, M. Messer, T. Rigaldo, G. Puentes, D. Weld, and W. Ketterle. "Observation of two-beam collective scattering phenomena in a Bose-Einstein condensate". In: *Phys. Rev. A* 96.5 (2017). DOI: `10.1103/PhysRevA.96.051603` (cit. on pp. 14, 16, 65, 80).

[51] Z. A. Geiger, K. M. Fujiwara, K. Singh, R. Senaratne, S. V. Rajagopal, M. Lipatov, T. Shimasaki, R. Driben, V. V. Konotop, T. Meier, and D. M. Weld. "Observation and Uses of Position-Space Bloch Oscillations in an Ultracold Gas". In: *Phys. Rev. Lett.* 120.21 (2018), p. 213201. DOI: `10.1103/PhysRevLett.120.213201` (cit. on pp. 14, 16).

[52] N. Gross and L. Khaykovich. "All-optical production of ^{7}Li Bose-Einstein condensation using Feshbach resonances". In: *Phys. Rev. A* 77.2 (2008). DOI: `10.1103/PhysRevA.77.023604` (cit. on pp. 14, 16).

[53] T. Ikemachi, A. Ito, Y. Aratake, Y. Chen, M. Koashi, M. Kuwata-Gonokami, and M. Horikoshi. "All-optical production of dual Bose–Einstein condensates of paired fermions and bosons with ^{6}Li and ^{7}Li". In: *Journal of Physics B: Atomic, Molecular and Optical Physics* 50.1 (2017). DOI: `10.1088/1361-6455/50/1/01lt01` (cit. on pp. 14, 16).

[54] M. S. Safronova, U. I. Safronova, and C. W. Clark. "Magic wavelengths for optical cooling and trapping of lithium". In: *Phys. Rev. A* 86.4 (2012). DOI: `10.1103/PhysRevA.86.042505` (cit. on p. 14).

[55] P. M. Duarte, R. A. Hart, J. M. Hitchcock, T. A. Corcovilos, T. L. Yang, A. Reed, and R. G. Hulet. "All-optical production of a lithium quantum gas using narrow-line laser cooling". In: *Phys. Rev. A* 84.6 (2011). DOI: `10.1103/PhysRevA.84.061406` (cit. on p. 14).

[56] M. Fischer. "An Optical Dipole Trap and an Accordion Lattice for a Quantum Gas Microscope". Master's Thesis. University of Hamburg, 2018 (cit. on pp. 15, 48, 50).

[57] A. Kerkmann. “A novel Apparatus for Quantum Gas Microscopy of Lithium Atoms”. PhD Thesis. University of Hamburg, 2019 (cit. on pp. 15, 17–21, 24, 27, 30–32, 48, 50–52, 61, 80).

[58] M. H. Hagemann. “A Setup for High-Resolution Imaging of Ultracold Lithium Atoms”. PhD Thesis. University of Hamburg, 2020 (cit. on pp. 15, 18, 20, 21, 33, 50, 51).

[59] T. Petersen. “Tools for lithium quantum gas experiments: radiofrequency control, interlock system and image response function”. Master’s Thesis. University of Hamburg, 2020 (cit. on pp. 15, 25, 27).

[60] A. G. Truscott, K. E. Strecker, W. I. McAlexander, G. B. Partridge, and R. G. Hulet. “Observation of Fermi Pressure in a Gas of Trapped Atoms”. In: *Science* 291.5513 (2001), pp. 2570–2. DOI: `10.1126/science.1059318` (cit. on p. 16).

[61] K. E. Strecker, G. B. Partridge, A. G. Truscott, and R. G. Hulet. “Formation and propagation of matter-wave soliton trains”. In: *Nature* 417.6885 (2002), pp. 150–3. DOI: `10.1038/nature747` (cit. on p. 16).

[62] Y. P. Chen, J. Hitchcock, D. Dries, M. Junker, C. Welford, and R. G. Hulet. “Phase coherence and superfluid-insulator transition in a disordered Bose-Einstein condensate”. In: *Phys. Rev. A* 77.3 (2008). DOI: `10.1103/PhysRevA.77.033632` (cit. on p. 16).

[63] R. Wang, M. Liu, F. Minardi, and M. Kasevich. “Reaching ^{7}Li quantum degeneracy with a minitrap”. In: *Phys. Rev. A* 75.1 (2007). DOI: `10.1103/PhysRevA.75.013610` (cit. on p. 16).

[64] N. Navon, S. Piatecki, K. Gunter, B. Rem, T. C. Nguyen, F. Chevy, W. Krauth, and C. Salomon. “Dynamics and Thermodynamics of the Low-Temperature Strongly Interacting Bose Gas”. In: *Phys. Rev. Lett.* 107.13 (2011), p. 135301. DOI: `10.1103/PhysRevLett.107.135301` (cit. on p. 16).

[65] I. L. Dimitrova. “Realizing quantum spin models with ^{7}Li atoms in an optical lattice”. PhD Thesis. Massachusetts Institute of Technology, 2020 (cit. on p. 16).

[66] Z. Geiger. “An Apparatus for Dynamical Quantum Emulation Using Ultracold Lithium”. PhD Thesis. University of California Santa Barbara, 2018 (cit. on pp. 16, 21, 43).

[67] C. Fujiwara. “Dynamics of Ultracold Lithium in Modulated Optical Lattices”. PhD Thesis. University of California Santa Barbara, 2019 (cit. on p. 16).

[68] E. Q. Simmons, R. Sajjad, K. Keithley, H. Mas, J. L. Tanlimco, E. Nolasco-Martinez, Y. Bai, G. H. Fredrickson, and D. M. Weld. “Thermodynamic engine with a quantum degenerate working fluid”. In: (Apr. 2023), arXiv:2304.00659. DOI: `10.48550/arXiv.2304.00659` (cit. on p. 16).

[69] Z. Vendeiro, J. Ramette, A. Rudelis, M. Chong, J. Sinclair, L. Stewart, A. Urvoy, and V. Vuletić. “Machine-learning-accelerated Bose-Einstein condensation”. In: *Physical Review Research* 4.4 (2022). DOI: `10.1103/PhysRevResearch.4.043216` (cit. on p. 17).

[70] G. A. Phelps, A. Hébert, A. Krahn, S. Dickerson, F. Öztürk, S. Ebadi, L. Su, and M. Greiner. “Sub-second production of a quantum degenerate gas”. In: (2020). arXiv: `2007.10807 [cond-mat.quant-gas]` (cit. on p. 17).

[71] M. Bankau. “Saturated Absorption Spectroscopy and Design of an Ultra-High-Vacuum Chamber for a Lithium Quantum Gas Experiment”. Bachelor’s Thesis. University of Hamburg, 2014 (cit. on p. 18).

[72] A. Kerkmann. “Ein Lasersystem zum Fangen und Kühlen von bosonischem und fermionischem Lithium”. Thesis. University of Hamburg, 2015 (cit. on pp. 18, 19, 28, 30).

[73] K. Dieckmann, R. J. C. Spreeuw, M. Weidemüller, and J. T. M. Walraven. “Two-dimensional magneto-optical trap as a source of slow atoms”. In: *Phys. Rev. A* 58.5 (1998), pp. 3891–3895. DOI: `10.1103/PhysRevA.58.3891` (cit. on p. 18).

[74] J. Schoser, A. Batär, R. Löw, V. Schweikhard, A. Grabowski, Y. B. Ovchinnikov, and T. Pfau. “Intense source of cold Rb atoms from a pure two-dimensional magneto-optical trap”. In: *Phys. Rev. A* 66.2 (2002). DOI: `10.1103/PhysRevA.66.023410` (cit. on p. 18).

[75] J. Catani, P. Maioli, L. De Sarlo, F. Minardi, and M. Inguscio. “Intense slow beams of bosonic potassium isotopes”. In: *Phys. Rev. A* 73.3 (2006). DOI: `10.1103/PhysRevA.73.033415` (cit. on p. 18).

[76] T. G. Tiecke, S. D. Gensemer, A. Ludewig, and J. T. M. Walraven. “High-flux two-dimensional magneto-optical-trap source for cold lithium atoms”. In: *Phys. Rev. A* 80.1 (2009). DOI: `10.1103/PhysRevA.80.013409` (cit. on pp. 18, 32, 37).

[77] M. H. Hagemann. “Magnetic field coils and an interferometer for a quantum gas microscope with lithium atoms”. Master’s Thesis. University of Hamburg, 2016 (cit. on p. 21).

[78] R. von Wurmb. “About a symmetry problem of Helmholtz coils and their corresponding magnetic fields”. Bachelor’s Thesis. University of Hamburg, 2023 (cit. on p. 21).

[79] A. Keshet and W. Ketterle. “A distributed, graphical user interface based, computer control system for atomic physics experiments”. In: *Rev Sci Instrum* 84.1 (2013), p. 015105. DOI: `10.1063/1.4773536` (cit. on p. 26).

[80] N.-O. Rohweder. “Developing a modular camera program for quantum gas experiments”. Bachelor’s Thesis. University of Hamburg, 2014 (cit. on p. 26).

[81] F. Huber. “Site-Resolved Imaging with the Fermi Gas Microscope”. PhD Thesis. Harvard University, 2014 (cit. on pp. 31, 32, 52).

[82] K. Li, D. Zhang, T. Gao, S.-G. Peng, and K. Jiang. “Enhanced trapping of cold ^{6}Li using multiple-sideband cooling in a two-dimensional magneto-optical trap”. In: *Phys. Rev. A* 92.1 (2015). DOI: `10.1103/PhysRevA.92.013419` (cit. on p. 36).

[83] J. H. Lee and J. Mun. “Optimized atomic flux from a frequency-modulated two-dimensional magneto-optical trap for cold fermionic potassium atoms”. In: *Journal of the Optical Society of America B* 34.7 (2017). DOI: `10.1364/josab.34.001415` (cit. on p. 36).

[84] B. P. Anderson and M. A. Kasevich. “Enhanced loading of a magneto-optic trap from an atomic beam”. In: *Phys. Rev. A* 50.5 (1994), R3581–R3584. DOI: `10.1103/physreva.50.r3581` (cit. on p. 37).

[85] W. Ketterle, D. S. Durfee, and D. M. Stamper-Kurn. “Making, probing and understanding Bose-Einstein condensates”. In: (1999). arXiv: `cond-mat/9904034 [cond-mat]` (cit. on pp. 39, 44, 83).

[86] M.-O. Mewes. “Bose-Einstein Condensation of Sodium Atoms”. PhD Thesis. Massachusetts Institute of Technology, 1997 (cit. on p. 40).

[87] M. Stolpmann. “Intensity Stabilization and Deep Learning Based Laser Speckle Spectrometer”. Master’s Thesis. University of Hamburg, 2022 (cit. on pp. 45, 51).

[88] D. Vogel. “Measuring Geometry and Topology of Floquet-Bloch States in and out of Equilibrium with ultracold fermions”. PhD Thesis. University of Hamburg, 2018 (cit. on pp. 48, 61).

[89] N. Käming. “Upcoming PhD Thesis”. PhD Thesis. University of Hamburg, 2023 (cit. on p. 49).

[90] F. Schreck. “Mixtures of ultracold Gases: Fermi sea and Bose-Einstein Condensate of Lithium Isotopes”. PhD Thesis. 2002 (cit. on p. 50).

[91] C. J. Pethick and H. Smith. *Bose–Einstein Condensation in Dilute Gases*. 2nd ed. Cambridge University Press, 2008. DOI: `10.1017/CBO9780511802850` (cit. on p. 55).

[92] M. Lewenstein, A. Sanpera, V. Ahufinger, B. Damski, A. Sen, and U. Sen. “Ultracold atomic gases in optical lattices: mimicking condensed matter physics and beyond”. In: *Advances in Physics* 56.2 (2007), pp. 243–379. DOI: `10.1080/00018730701223200` (cit. on p. 57).

[93] P. Windpassinger and K. Sengstock. “Engineering novel optical lattices”. In: *Rep Prog Phys* 76.8 (2013), p. 086401. DOI: `10.1088/0034-4885/76/8/086401` (cit. on p. 57).

[94] K. I. Petsas, A. B. Coates, and G. Grynberg. “Crystallography of optical lattices”. In: *Phys. Rev. A* 50.6 (1994), pp. 5173–5189. DOI: `10.1103/physreva.50.5173` (cit. on p. 57).

[95] M. Anderlini, P. J. Lee, B. L. Brown, J. Sebby-Strabley, W. D. Phillips, and J. V. Porto. “Controlled exchange interaction between pairs of neutral atoms in an optical lattice”. In: *Nature* 448.7152 (2007), pp. 452–6. DOI: `10.1038/nature06011` (cit. on p. 57).

[96] S. Trotzky, P. Cheinet, S. Folling, M. Feld, U. Schnorrberger, A. M. Rey, A. Polkovnikov, E. A. Demler, M. D. Lukin, and I. Bloch. “Time-Resolved Observation and Control of Superexchange Interactions with Ultracold Atoms in Optical Lattices”. In: *Science* 319.5861 (2008), pp. 295–9. DOI: `10.1126/science.1150841` (cit. on p. 57).

[97] L. Tarruell, D. Greif, T. Uehlinger, G. Jotzu, and T. Esslinger. “Creating, moving and merging Dirac points with a Fermi gas in a tunable honeycomb lattice”. In: *Nature* 483.7389 (2012), pp. 302–5. DOI: `10.1038/nature10871` (cit. on p. 57).

[98] H.-N. Dai, B. Yang, A. Reingruber, X.-F. Xu, X. Jiang, Y.-A. Chen, Z.-S. Yuan, and J.-W. Pan. “Generation and detection of atomic spin entanglement in optical lattices”. In: *Nature Physics* 12.8 (2016), pp. 783–787. DOI: `10.1038/nphys3705` (cit. on p. 57).

[99] C. Robens, J. Zopes, W. Alt, S. Brakhane, D. Meschede, and A. Alberti. “Low-Entropy States of Neutral Atoms in Polarization-Synthesized Optical Lattices”. In: *Phys. Rev. Lett.* 118.6 (2017), p. 065302. DOI: `10.1103/PhysRevLett.118.065302` (cit. on p. 57).

[100] X. Q. Wang, G. Q. Luo, J. Y. Liu, W. V. Liu, A. Hemmerich, and Z. F. Xu. “Evidence for an atomic chiral superfluid with topological excitations”. In: *Nature* 596.7871 (2021), pp. 227–231. DOI: `10.1038/s41586-021-03702-0` (cit. on pp. 57, 66, 80).

[101] M. D. Li, W. Lin, A. Luo, W. Y. Zhang, H. Sun, B. Xiao, Y. G. Zheng, Z. S. Yuan, and J. W. Pan. "High-powered optical superlattice with robust phase stability for quantum gas microscopy". In: *Opt Express* 29.9 (2021), pp. 13876–13886. DOI: `10.1364/OE.423776` (cit. on p. 57).

[102] D. Wei, D. Adler, K. Srakaew, S. Agrawal, P. Weckesser, I. Bloch, and J. Zeiher. "Observation of brane parity order in programmable optical lattices". In: (2023). arXiv: `2301.11869 [cond-mat.quant-gas]` (cit. on p. 57).

[103] C. Becker, P. Soltan-Panahi, J. Kronjäger, S. Dörscher, K. Bongs, and K. Sengstock. "Ultracold quantum gases in triangular optical lattices". In: *New Journal of Physics* 12.6 (2010). DOI: `10.1088/1367-2630/12/6/065025` (cit. on p. 57).

[104] J. Struck, C. Olschlager, R. Le Targat, P. Soltan-Panahi, A. Eckardt, M. Lewenstein, P. Windpassinger, and K. Sengstock. "Quantum Simulation of Frustrated Classical Magnetism in Triangular Optical Lattices". In: *Science* 333.6045 (2011), pp. 996–9. DOI: `10.1126/science.1207239` (cit. on p. 57).

[105] N. Fläschner, B. S. Rem, M. Tarnowski, D. Vogel, D. S. Luhmann, K. Sengstock, and C. Weitenberg. "Experimental reconstruction of the Berry curvature in a Floquet Bloch band". In: *Science* 352.6289 (2016), pp. 1091–4. DOI: `10.1126/science.aad4568` (cit. on pp. 57, 66).

[106] M. N. Kosch. "Studying Quantum Gases in a Dynamically Tunable Lattice with Sub-Lattice-Site Resolution". PhD Thesis. University of Hamburg, 2023 (cit. on pp. 59, 66).

[107] B. Gadway. "Atom-optics approach to studying transport phenomena". In: *Phys. Rev. A* 92.4 (2015). DOI: `10.1103/PhysRevA.92.043606` (cit. on p. 62).

[108] E. J. Meier, F. A. An, and B. Gadway. "Atom-optics simulator of lattice transport phenomena". In: *Phys. Rev. A* 93.5 (2016). DOI: `10.1103/PhysRevA.93.051602` (cit. on p. 62).

[109] S. Ostermann, F. Piazza, and H. Ritsch. "Spontaneous Crystallization of Light and Ultracold Atoms". In: *Phys. Rev. X* 6.2 (2016). DOI: `10.1103/PhysRevX.6.021026` (cit. on pp. 65, 80).

[110] G. Jotzu, M. Messer, R. Desbuquois, M. Lebrat, T. Uehlinger, D. Greif, and T. Esslinger. "Experimental realization of the topological Haldane model with ultracold fermions". In: *Nature* 515.7526 (2014), pp. 237–40. DOI: `10.1038/nature13915` (cit. on p. 66).

[111] K. Wintersperger, C. Braun, F. N. Ünal, A. Eckardt, M. D. Liberto, N. Goldman, I. Bloch, and M. Aidelsburger. "Realization of an anomalous Floquet topological system with ultracold atoms". In: *Nature Physics* 16.10 (2020), pp. 1058–1063. DOI: `10.1038/s41567-020-0949-y` (cit. on p. 66).

[112] P. Hauke, M. Lewenstein, and A. Eckardt. "Tomography of Band Insulators from Quench Dynamics". In: *Phys. Rev. Lett.* 113.4 (2014), p. 045303. DOI: `10.1103/PhysRevLett.113.045303` (cit. on p. 66).

[113] M. Tarnowski, F. N. Unal, N. Fläschner, B. S. Rem, A. Eckardt, K. Sengstock, and C. Weitenberg. "Measuring topology from dynamics by obtaining the Chern number from a linking number". In: *Nature Communications* 10.1 (2019), p. 1728. DOI: `10.1038/s41467-019-09668-y` (cit. on p. 66).

[114] K. D. Nelson, X. Li, and D. S. Weiss. "Imaging single atoms in a three-dimensional array". In: *Nature Physics* 3.8 (2007), pp. 556–560. DOI: `10.1038/nphys645` (cit. on p. 67).

[115] O. Elíasson, J. S. Laustsen, R. Heck, R. Müller, J. J. Arlt, C. A. Weidner, and J. F. Sherson. "Spatial tomography of individual atoms in a quantum gas microscope". In: *Phys. Rev. A* 102.5 (2020). DOI: `10.1103/PhysRevA.102.053311` (cit. on p. 67).

[116] T. Gericke, P. Würtz, D. Reitz, T. Langen, and H. Ott. "High-resolution scanning electron microscopy of an ultracold quantum gas". In: *Nature Physics* 4.12 (2008), pp. 949–953. DOI: `10.1038/nphys1102` (cit. on p. 67).

[117] C. Veit, N. Zuber, O. A. Herrera-Sancho, V. S. V. Anasuri, T. Schmid, F. Meinert, R. Löw, and T. Pfau. "Pulsed Ion Microscope to Probe Quantum Gases". In: *Phys. Rev. X* 11.1 (2021). DOI: `10.1103/PhysRevX.11.011036` (cit. on p. 67).

[118] M. McDonald, J. Trisnadi, K.-X. Yao, and C. Chin. "Superresolution Microscopy of Cold Atoms in an Optical Lattice". In: *Phys. Rev. X* 9.2 (2019). DOI: `10.1103/PhysRevX.9.021001` (cit. on p. 67).

[119] S. Subhankar, Y. Wang, T. C. Tsui, S. L. Rolston, and J. V. Porto. "Nanoscale Atomic Density Microscopy". In: *Phys. Rev. X* 9.2 (2019). DOI: `10.1103/physrevx.9.021002` (cit. on p. 67).

[120] N. Read and N. R. Cooper. "Free expansion of lowest-Landau-level states of trapped atoms: A wave-function microscope". In: *Phys. Rev. A* 68.3 (2003). DOI: `10.1103/PhysRevA.68.035601` (cit. on p. 67).

[121] A. del Campo. "Frictionless quantum quenches in ultracold gases: A quantum-dynamical microscope". In: *Phys. Rev. A* 84.3 (2011). DOI: `10.1103/PhysRevA.84.031606` (cit. on p. 67).

[122] I. Shvarchuck, C. Buggle, D. S. Petrov, K. Dieckmann, M. Zielonkowski, M. Kemmann, T. G. Tiecke, W. von Klitzing, G. V. Shlyapnikov, and J. T. Walraven. "Bose-Einstein condensation into Nonequilibrium States Studied by Condensate Focusing". In: *Phys. Rev. Lett.* 89.27 (2002), p. 270404. DOI: `10.1103/PhysRevLett.89.270404` (cit. on p. 67).

[123] A. H. van Amerongen, J. J. van Es, P. Wicke, K. V. Kheruntsyan, and N. J. van Druten. "Yang-Yang thermodynamics on an atom chip". In: *Phys. Rev. Lett.* 100.9 (2008), p. 090402. DOI: `10.1103/PhysRevLett.100.090402` (cit. on p. 67).

[124] S. Tung, G. Lamporesi, D. Lobser, L. Xia, and E. A. Cornell. "Observation of the presuperfluid regime in a two-dimensional Bose gas". In: *Phys. Rev. Lett.* 105.23 (2010), p. 230408. DOI: `10.1103/PhysRevLett.105.230408` (cit. on p. 67).

[125] P. A. Murthy, D. Kedar, T. Lompe, M. Neidig, M. G. Ries, A. N. Wenz, G. Zürn, and S. Jochim. "Matter-wave Fourier optics with a strongly interacting two-dimensional Fermi gas". In: *Phys. Rev. A* 90.4 (2014). DOI: `10.1103/PhysRevA.90.043611` (cit. on p. 67).

[126] K. Hueck, N. Luick, L. Sobirey, J. Siegl, T. Lompe, and H. Moritz. "Two-Dimensional Homogeneous Fermi Gases". In: *Phys. Rev. Lett.* 120.6 (2018), p. 060402. DOI: `10.1103/PhysRevLett.120.060402` (cit. on p. 67).

[127] L. Asteria, H. P. Zahn, M. N. Kosch, K. Sengstock, and C. Weitenberg. “Quantum gas magnifier for sub-lattice-resolved imaging of 3D quantum systems, Supplementary information”. In: *Nature* 599 (2021), pp. 571–575. DOI: `10.1038/s41586-021-04011-2` (cit. on pp. 68, 70).

[128] L. Asteria. “Quantum Gas Magnifier for imaging of ultracold Atoms in highly tunable optical Lattices”. PhD Thesis. University of Hamburg, 2022 (cit. on pp. 70, 71, 76, 77).

[129] M. Horikoshi, A. Ito, T. Ikemachi, Y. Aratake, M. Kuwata-Gonokami, and M. Koashi. “Appropriate Probe Condition for Absorption Imaging of Ultracold ^{6}Li Atoms”. In: *Journal of the Physical Society of Japan* 86.10 (2017). DOI: `10.7566/jpsj.86.104301` (cit. on p. 71).

[130] Y. Zhai, C. H. Carson, V. A. Henderson, P. F. Griffin, E. Riis, and A. S. Arnold. “Talbot-enhanced, maximum-visibility imaging of condensate interference”. In: *Optica* 5.1 (2018). DOI: `10.1364/optica.5.000080` (cit. on p. 71).

[131] M. Holten, L. Bayha, K. Subramanian, S. Brandstetter, C. Heintze, P. Lunt, P. M. Preiss, and S. Jochim. “Observation of Cooper pairs in a mesoscopic two-dimensional Fermi gas”. In: *Nature* 606.7913 (2022), pp. 287–291. DOI: `10.1038/s41586-022-04678-1` (cit. on p. 74).

[132] J. F. Clauser and S. Li. “Talbot-vonLau atom interferometry with cold slow potassium”. In: *Phys. Rev. A* 49.4 (1994), R2213–R2216. DOI: `10.1103/physreva.49.r2213` (cit. on p. 75).

[133] M. S. Chapman, C. R. Ekstrom, T. D. Hammond, J. Schmiedmayer, B. E. Tannian, S. Wehinger, and D. E. Pritchard. “Near-field imaging of atom diffraction gratings: The atomic Talbot effect”. In: *Phys. Rev. A* 51.1 (1995), R14–R17. DOI: `10.1103/physreva.51.r14` (cit. on p. 75).

[134] S. Nowak, C. Kurtsiefer, T. Pfau, and C. David. “High-order Talbot fringes for atomic matter waves”. In: *Opt Lett* 22.18 (1997), pp. 1430–2. DOI: `10.1364/ol.22.001430` (cit. on p. 75).

[135] B. Santra, C. Baals, R. Labouvie, A. B. Bhattacherjee, A. Pelster, and H. Ott. “Measuring finite-range phase coherence in an optical lattice using Talbot interferometry”. In: *Nature Communications* 8 (2017), p. 15601. DOI: `10.1038/ncomms15601` (cit. on p. 75).

[136] P. Höllmer, J.-S. Bernier, C. Kollath, C. Baals, B. Santra, and H. Ott. “Talbot effect in the presence of interactions”. In: *Phys. Rev. A* 100.6 (2019). DOI: `10.1103/PhysRevA.100.063613` (cit. on p. 75).

[137] R. Ziv, A. Patsyk, Y. Lumer, Y. Sagi, Y. C. Eldar, and M. Segev. “Phase Retrieval of Vortices in Bose-Einstein Condensates”. In: (2022). arXiv: `2211.11668 [cond-mat.quant-gas]` (cit. on pp. 78, 80).

[138] R. Bücker, A. Perrin, S. Manz, T. Betz, C. Koller, T. Plisson, J. Rottmann, T. Schumm, and J. Schmiedmayer. “Single-particle-sensitive imaging of freely propagating ultracold atoms”. In: *New Journal of Physics* 11.10 (2009). DOI: `10.1088/1367-2630/11/10/103039` (cit. on pp. 78, 80).

[139] A. Fuhrmanek, A. M. Lance, C. Tuchendler, P. Grangier, Y. R. P. Sortais, and A. Browaeys. “Imaging a single atom in a time-of-flight experiment”. In: *New Journal of Physics* 12.5 (2010). DOI: `10.1088/1367-2630/12/5/053028` (cit. on p. 78).

[140] C. J. Picken, R. Legaie, and J. D. Pritchard. “Single atom imaging with an sCMOS camera”. In: *Applied Physics Letters* 111.16 (2017). DOI: `10.1063/1.5003304` (cit. on p. 78).

[141] A. Bergschneider, V. M. Klinkhamer, J. H. Becher, R. Klemt, G. Zürn, P. M. Preiss, and S. Jochim. “Spin-resolved single-atom imaging of $^{6}\mathrm{Li}$ in free space”. In: *Phys. Rev. A* 97 (2018), p. 063613. DOI: `10.1103/PhysRevA.97.063613` (cit. on pp. 78, 80).

[142] N. R. Cooper. “Rapidly rotating atomic gases”. In: *Advances in Physics* 57.6 (2008), pp. 539–616. DOI: `10.1080/00018730802564122` (cit. on p. 80).

[143] B. Andrade, V. Kasper, M. Lewenstein, C. Weitenberg, and T. Graß. “Preparation of the 1/2 Laughlin state with atoms in a rotating trap”. In: *Phys. Rev. A* 103.6 (2021). DOI: `10.1103/PhysRevA.103.063325` (cit. on p. 80).

[144] R. J. Fletcher, A. Shaffer, C. C. Wilson, P. B. Patel, Z. Yan, V. Crepel, B. Mukherjee, and M. W. Zwierlein. “Geometric squeezing into the lowest Landau level”. In: *Science* 372.6548 (2021), pp. 1318–1322. DOI: `10.1126/science.aba7202` (cit. on p. 80).

[145] B. Mukherjee, A. Shaffer, P. B. Patel, Z. Yan, C. C. Wilson, V. Crepel, R. J. Fletcher, and M. Zwierlein. “Crystallization of bosonic quantum Hall states in a rotating quantum gas”. In: *Nature* 601.7891 (2022), pp. 58–62. DOI: `10.1038/s41586-021-04170-2` (cit. on p. 80).

[146] J. Leonard, S. Kim, J. Kwan, P. Segura, F. Grusdt, C. Repellin, N. Goldman, and M. Greiner. “Realization of a fractional quantum Hall state with ultracold atoms”. In: *Nature* 619.7970 (2023), pp. 495–499. DOI: `10.1038/s41586-023-06122-4` (cit. on p. 80).

[147] S. P. Ram, S. R. Mishra, S. K. Tiwari, and H. S. Rawat. “Temperature and phase-space density of a cold atom cloud in a quadrupole magnetic trap”. In: *Journal of the Korean Physical Society* 65.4 (2014), pp. 462–470. DOI: `10.3938/jkps.65.462` (cit. on p. 82).

[148] J. Stuhler, P. O. Schmidt, S. Hensler, J. Werner, J. Mlynek, and T. Pfau. “Continuous loading of a magnetic trap”. In: *Phys. Rev. A* 64.3 (2001). DOI: `10.1103/PhysRevA.64.031405` (cit. on p. 82).

[149] T. Badr, D. B. Ali, J. Seaward, Y. Guo, F. Wiotte, R. Dubessy, H. Perrin, and A. Perrin. “Comparison of time profiles for the magnetic transport of cold atoms”. In: *Applied Physics B* 125.6 (2019). DOI: `10.1007/s00340-019-7213-0` (cit. on p. 82).

[150] D. Yum, J. Park, W. Lee, and W. Jhe. “Systematic study of the rf-induced evaporation of ^{87}Rb atoms in a spherical magnetic quadrupole trap”. In: *Journal of the Korean Physical Society* 60.1 (2012), pp. 1–5. DOI: `10.3938/jkps.60.1` (cit. on p. 84).

[151] H. J. Lewandowski, D. M. Harber, D. L. Whitaker, and E. A. Cornell. “Simplified System for Creating a Bose–Einstein Condensate”. In: *Journal of Low Temperature Physics* 132.5/6 (2003), pp. 309–367. DOI: `10.1023/a:1024800600621` (cit. on pp. 84, 85).

Glossary

1D 1-dimensional 1, 57–62, 64, 65, 68, 75

2D 2-dimensional v, 1, 18, 57, 58, 65, 67, 68, 71, 75, 76, 78

3D 3-dimensional 18, 67, 68

AH anti-Helmholtz 21, 22, 28

AOM acousto-optic modulator 28, 30, 31, 42, 45, 52, 53, 59–62, 65, 73, 76

AR anti-reflection 19

AWG arbitrary waveform generator 36

BEC Bose-Einstein condensate 1, 2, 15, 16, 37, 51, 55, 63, 72, 73, 80, 107

cMOT compressed MOT 27, 28, 38, 39, 43

dPLL digital phase-locked loop 32

DSP dark state pumping 34, 42, 43

ECDL external cavity diode laser 28, 31

EOM electro-optic modulator 28, 31, 33, 36, 39, 52, 53, 59, 61, 62, 64–66, 79

FMS frequency modulation spectroscopy 28, 30

FPI Fabry-Perot interferometer 31, 52

GLP Glan-laser polarizer 52

GM Gray Molasses 16, 38, 39

GUI graphical user interface 26

HH Helmholtz 21, 22

IGBT insulated-gate bipolar transistor 22, 23, 43, 48

MFL multi-frequency lattice 51

MOT magneto-optical trap 12, 14, 16, 20, 21, 27, 30, 31

MT magnetic trap 16, 21

MTS modulation transfer spectroscopy 28, 30

OD optical density 26, 47, 76, 77

ODT optical dipole trap 15, 16

PBS polarising beam splitter 28, 46, 51–53, 60

PCB printed circuit board 32

PD photodiode 52

PM polarization-maintaining 28, 30, 34

PSD Phase-Space Density 16, 27, 43, 44, 49, 53

RF radio frequency 2, 16, 17, 22, 24–26, 36, 41, 46–50, 54, 60–62, 73, 74, 76, 78, 79, 84, 103

RIN Relative intensity noise 87

RS-232 Recommended Standard 232 26

TA tapered amplifier 31

TCP/IP Transmission Control Protocol/Internet Protocol 26

VISA virtual instrument software architecture 26

VVA voltage variable attenuator 61

XHV extreme-high vacuum 17

List of Figures

2.1 Vapor pressure of different alkali elements 4
2.2 Energy level scheme of ^{7}Li 7
2.3 Ground-state energy shift at varying magnetic field 9
2.4 Energy shift of the $2^2P_{1/2}$-state at varying magnetic field 9
2.5 Energy shift of the $2^2P_{3/2}$-state at varying magnetic field 10
2.6 D2 transitions at high fields from $m_J = -1/2$ 10
2.7 D2 transitions at high fields from $m_J = +1/2$ 11
2.8 Feshbach resonances for intra-spin collisions in the lowest hypferfine state . . 13
2.9 Feshbach resonances for spin mixtures in the lowest hypferfine state 14

3.1 CAD drawing of the vacuum chamber 17
3.2 Sideview of the vacuum chamber 18
3.3 3D explosion plot of the science cell 19
3.4 Side-cut through the magnetic field coils surrounding the glass cell 20
3.5 Circuit for switching the current through the MOT and the Feshbach coils . 22
3.6 Noise spectra of the IGBT drivers 23
3.7 Photographs of the offset coils used in the experiment 24
3.8 Input return loss of the broadband antenna 25
3.9 Narrow-resonance RF antenna used for fast state transfers 25
3.10 Input return loss of the narrow-resonance antennas 26
3.11 Illustration of the experiment control 27
3.12 Energy levels of ^{7}Li and the relative detunings of the applied laser beams . . 29
3.13 Sketch of the spectroscopy setup 30
3.14 Near-resonant laser system 31
3.15 The offset lock 32
3.16 View on the 2D-MOT through the rear window 33
3.17 Illustration of the 3D-MOT setup 34
3.18 Alignment of the 2D-MOT in front of the differential pumping tube 35

3.19 Alignment of the 2D-MOT with respect to the push beam 36
3.20 Illustration of the multi-frequency 2D-MOT approach 37
3.21 Comparison of the multi-frequency 2D-MOT with the simple 2D-MOT scheme 38
3.22 Concept of the evaporation in the magnetic trap 41
3.23 Illustration of the optical dark state pumping 42
3.24 Atom number in the dark state as a function of the pumping time 43
3.25 Laser system for the optical plug 45
3.26 Plug adjustment procedure 47
3.27 Saturation of the optical power of the plug beam 47
3.28 Influence of the plug beam on the optical density 48
3.29 Optimizing the stray field compensation along the z-axis 49
3.30 Magnetic field gradient and radio frequency during the evaporation 50
3.31 Sketch of the dipole trap telescopes and their arrangement around the glass cell 51
3.32 Laser system for the optical dipole trap and the optical lattice 52
3.33 Adiabatic state transfer in the optical dipole trap 54
3.34 Evaporation in the optical dipole trap 55

4.1 Concept of the multi-frequency lattice 58
4.2 Tuning the lattice potential via the geometry phase 59
4.3 Implementation of the multi-frequency lattice 60
4.4 Visualization of the staggered flux in the momentum lattice 62
4.5 Calibration of the geometry phase 63
4.6 Images of the density distribution of the atoms in the lattice 64
4.7 1D lattice structure from off-resonant beams 65

5.1 Working principle of the matter-wave microscope 68
5.2 Graphical illustration of the focusing condition 70
5.3 Measuring the single beam trap frequencies 73
5.4 Influence of interactions during the matter-wave protocol 74
5.5 Visualization of the Talbot effect in 1D and 2D 75
5.6 Mapping free evolution to the evolution in a harmonic trap 77
5.7 Analysis of the Talbot revivals 77

A.1 Peak PSD in the magnetic trap as a function of the capture gradient 83
A.2 Distorted in-situ images of the OD in the magnetic trap 85

B.1 Relative intensity noise of the lattice laser 87

List of Tables

2.1 Atomic properties of ^{7}Li 4

2.2 Physical and thermochemical properties of bulk ^{7}Li 4

2.3 Optical properties of the ^{7}Li D1-line 5

2.4 Optical properties of the ^{7}Li D2-line 6

2.5 Hyperfine constants for the $2S$ and $2P$ levels of ^{7}Li 7

2.6 ^{7}Li magnetic and electric field interaction parameters 8

2.7 Singlet and triplet s-wave scattering lengths for ^{7}Li 12

2.8 Position, width and zero-crossing of the Feshbach resonances of ^{7}Li 14

3.1 List of experimental groups that realized BECs of ^{7}Li 16

3.2 Experimental stages and corresponding particle number, temperature and PSD 16

3.3 Characteristic parameters of the main coils 21

3.4 Experimental key parameters for laser cooling 28

3.5 Overview of the evaporative cooling in the magnetic trap 49

Danksagung

An dieser Stelle möchte ich mich bei allen Menschen bedanken, die mich während dieser Arbeit unterstützt und begleitet haben. Mein erster Dank gilt Christof Weitenberg, dem PI unseres Experiments und Betreuer dieser Arbeit. Vielen Dank für die immer neuen Lösungsvorschläge in scheinbaren Sackgassen, die leidenschaftlichen Diskussionen, Deine motivierende Art sowie Deinen Rat und Deine vielseitige Unterstützung. Die Zusammenarbeit mit Dir in den letzten Jahren war extrem lehrreich. Zudem danke ich Henning Moritz nicht nur für die freundliche Übernahme des Gutachtens dieser Arbeit, sondern auch dafür, dass er bereits in den Bachelorvorlesungen des Physikstudiums mein Interesse an der Physik ultrakalter Quantengase entfacht hat. Desweiteren möchte ich mich bei Klaus Sengstock bedanken, der mir eine Masterarbeit in seiner Arbeitsgruppe ermöglicht hat und stets mit seinem umfangreichen Wissen und der langjährigen Erfahrung in allen technischen und physikalischen Fragen zum Gelingen dieser Arbeit beigetragen hat.

Meinem Mitdoktoranden der letzten Jahre Justus Brüggenjürgen gilt ein besonderer Dank. Wir haben in dieser Zeit vermutlich mehr Zeit zusammen im Labor als mit unseren Freunden und Familien verbracht. Danke für das gegenseitige Vertrauen, das gemeinsame Leiden und die gemeinsamen Freuden und für Deine Freundschaft. Nach vielen Rückschlägen haben wir in den letzten Jahren viel erreicht und ich freue mich auf die Zukunft. Darüber hinaus bedanke ich mich bei allen aktuellen und ehemaligen Mitarbeiterinnenn und Mitarbeitern an unserem Projekt. Besonders hervorheben möchte ich hierbei Benno Rem, Andreas Kerkmann und Michael Hagemann. In meiner Zeit als Masterstudent und während des ersten Jahres meiner Promotion konnte ich viel von Euch lernen und Euch als Freunde gewinnen. Auch den Master- und Bachelor-Studierenden, sowie HiWis der letzten Jahre sei an dieser Stelle gedankt.

Darüber hinaus möchte ich mich bei der gesamten Forschungsgruppe für das freundliche Miteinander sowie die tatkräftige gegenseitige Unterstützung bedanken - insbesondere beim BFM-Team, das uns stets mit Rat zur Seite gestanden hat sowie bei Ortwin Hellmig für die Betreuung und einfallsreiche Lösung diverser experimenteller Probleme. Außerdem gilt mein Dank allen Mitarbeiterinnen und Mitarbeitern des technischen und Verwaltungs-Personals, die mit ihrer Arbeit den erfolgreichen Betrieb des gesamten Instituts gewährleisten. Besonders zu erwähnen sind hier Reinhard Mielck sowie Finn-Marten Gloyer, die mit ihrer Beherrschung der teils in die Jahre gekommenen Haustechnik stabile experimentelle Umgebungen geschaffen haben. Außerhalb unserer Arbeitsgruppe haben viele Diskussionen mit Yann Kiefer und Max Hachmann uns immer wieder Ideen für neue experimentelle Ansätze beschert. Vielen Dank dafür.

Zu guter letzt bedanke ich mich bei meinen Freunden und meiner Familie, die mein gesamtes Studium sowie die Promotion mit viel Interesse, Unterstützung und Rücksicht begleitet haben.